Reactor Analysis and Safety Division

Reactor Analysis and Safety Division
Reactor Analysis and Safety Division
Reactor Analysis and Safety Division
Reactor Analysis and Safety Division
Reactor Analysis and Safety Division
Reactor Analysis and Safety Division
Reactor Analysis and Safety Division
Reactor Analysis and Safety Division
Reactor Analysis and Safety Division
Reactor Analysis and Safety Division
Reactor Analysis and Safety Division
Reactor Analysis and Safety Division
Reactor Analysis and Safety Division
Reactor Analysis and Safety Division
Reactor Analysis and Safety Division
Reactor Analysis and Safety Division

ANL/RAS-GPU-1

Assessment of the Integrity of TMI-2 Lower Head Instrument Penetration Weldments

by S. K. Wang, J. J. Sienicki, and B. W. Spencer

Argonne National Laboratory, Argonne, Illinois 60439
operated by The University of Chicago
for the United States Department of Energy under Contract W-31-109-Eng-38

Argonne National Laboratory, with facilities in the states of Illinois and Idaho, is owned by the United States government, and operated by The University of Chicago under the provisions of a contract with the Department of Energy.

ANL/RAS-GPU-1

ASSESSMENT OF THE INTEGRITY OF TMI-2 LOWER HEAD INSTRUMENT PENETRATION WELDMENTS

by

S. K. Wang
J. J. Sienicki
B. W. Spencer

August 1988

Disclaimer

Reactor Analysis and Safety Division
Argonne National Laboratory
9700 South Cass Avenue
Argonne, Illinois 60439

TABLE OF CONTENTS

Section	Page
NOMENCLATURE	vii
ABSTRACT	xi
I. INTRODUCTION	1
A. Background	1
B. Approach	4
II. TMI-2 MOLTEN CORE RELOCATION PHENEMONA AND CONDITIONS	6
A. Summary of Relocation Event	6
B. Initial Conditions of Corium Jet/Water Interaction	7
1. Initial Temperature of Corium Jet	7
2. Duration of Corium Relocation	8
C. Initial Water Temperature and Water Inventory in Vessel Lower Head	8
III. CORIUM JET BREAKUP AND TRANSIENT HEATUP OF VESSEL LOWER HEAD	17
A. Assumed Pathway of Corium Relocation	18
B. Corium-Jet Breakup and Quenching	27
C. Heatup of the Lower Head	42
1. Case i (Scoping Calculation)	42
2. Case ii (Bounding Severe Calculation)	43
IV. SUMMARY AND CONCLUSIONS	50
REFERENCES	55
ACKNOWLEDGMENTS	58
APPENDIX A - Corium Properties	59
APPENDIX B - Reactor Vessel Lower Head Properties	64
APPENDIX C - Modeling of Thermal and Hydrodynamic Aspects of Corium/Water Interactions	69
APPENDIX D - Corium Spreading and Drainage Inside the Core Former Region	84
APPENDIX E - Relocation of Control Rod Material	101
APPENDIX F - Heatup and Ablation of Lower Head by an Impinging Corium Jet	110

List of Figures

		Page
2.1	TMI-2 Recorded Data	9
2.2	Correlation of Events 3:30 to 5:30	10
2.3	Schematics of HPI Water Heatup	13
2.4	HPI Water Heatup	15
3.1	Schematics of Corium Relocation Ignoring Presence of Core Support Assembly (Case i)	19
3.2	Details of Core Support Assembly Structure (Case ii)	20
3.3	Side View of Corium Relocation from East Side Assumed in Case ii	21
3.4	Side View of Corium Relocation from South Side Assumed in Case ii	22
3.5	Top View of Lower Grid Rib and Flow Distribution Plate Associated with Corium Relocation (Case ii)	23
3.6	Top View of Flow Distribution Plate and Grid Forging Associated with Corium Relocation (Case ii)	25
3.7	Top View of Instrument Support Plate and Elliptical Flow Distribution Plate Associated with Corium Relocation (Case ii)	26
3.8	Primary System Pressure for a 6-inch Diameter Jet Without Pre-Fragmentation of CSA (Case i) for Different Injection Times	28
3.9	Primary System Pressure for a 6-inch Diameter Jet Without Pre-Fragmentation of CSA (Case i) for Different Injection Times	29
3.10	Primary System Pressure for a 6-inch Diameter Jet and 60 1 5/16-inch Jets Without Pre-Fragmentation of CSA (Cases i and iiia) for 205 K Water Subcooling	31
3.11	Primary System Pressure (Cases i, ii, iiia, and iiib) for 90 K Water Subcooling	32
3.12	Corium Jet Breakup and Particle/Droplet Formation for Case i	34
3.13	Corium Jet Breakup and Particle/Droplet Formation for Case iii	35
3.14	Corium Jet Breakup and Particle/Droplet Formation for Case iiia	36

List of Figures (cont.)

Page

3.15 Corium Jet Breakup and Particle/Droplet Formation for Case iiib 37

3.16 Corium Temperature Variation for Case i 38

3.17 Corium Temperature Variation for Case ii 39

3.18 Corium Temperature Variation for Case iiia 40

3.19 Corium Temperature Variation for Case iiib 41

3.20 Temperature at Interface Between Corium Crust and Vessel Lower Head Steel Following Onset of Corium Jet Impingement and Thickness of Corium Crust Formed Upon Lower Head Resulting from the Impingement of a Single Unimpeded Jet 44

3.21 Temperature Profile Within Vessel Lower Head at Inception of Steel Melting Resulting from the Impingement of a Single Unimpeded Jet 45

3.22 Thickness of Lower Head Wall Ablated Following Onset of Corium Jet Impingement of a Single Jet 46

3.23 Temperature at Interface Between Corium Crust and Vessel Lower Head Steel Following Onset of Corium Jet Impingement and Thickness of Corium Crust Formed Upon Lower Head Resulting from the Impingement of Four Corium Jets Draining from the Core Support Assembly 48

3.24 Temperature Profile through the Thickness of Lower Head at the End of the Jet Impingement Phase 49

NOMENCLATURE

A = area, m^2

A = atomic weight, g

a = flow hole drainage area per unit channel length, m

C = discharge coefficient

C_D = drag coefficient

C_p = specific heat, J/kg•K

C_m = constant in Eq. (C.11), $m^{1/2}$

$C_{f,jet}$ = specific heat of molten corium, J/kg•K

$C_{s,film}$ = specific heat of melted film, J/kg•K

D = diameter, m

e_c = corium crust specific enthalpy at temperature T_c, MJ/kg

e_s = steel specific enthalpy, MJ/kg

$\Delta e_{s,liq}$ = change in steel specific enthalpy in going from initial temperature to liquidus, J/kg

g = gravitational constant, m/s^2

h = heat transfer coefficient, $W/m^2 \cdot K$

h_{fg} = latent heat of evaporation, J/kg

h'_{fg} = latent heat of evaporation including sensible heat, J/kg

h_{liquid} = specific enthalpy of corium liquid phase, MJ/kg

h_{solid} = specific enthalpy of corium solid phase, MJ/kg

h_{fusion} = corium heat of fusion, MJ/kg

k = Boltzmann's constant

k = heat conductivity, W/m•K

k_p = the most probable wave number of surface disturbances, 1/m

L = length, m

L_f = corium heat of fusion, MJ/kg

m = mass, kg

$\dot{m}_i$ = mass flux of steam condensation, $kg/m^2 \cdot s$

P = pressure, MPa

Pr = Prandtl number

Q = activation energy, J/mole

q''_R = radiation heat flux, W/m^2

q''_S = heat flux from structure, W/m^2

R_J = jet radius, m

R_o = jet initial radius, m

Re = Reynold number

R_v = universal gas constant, $R_v = 8.2 \times 10^{-6}$ $MPa \cdot m^3/gmole \cdot K$

t = time, s

T = temperature, K

U = velocity, m/s

V = velocity, m/s

V = volume, m^3

w = mass flow rate, kg/s

w = channel width, m

x = distance, m

X = mole fraction

y = distance, m

z = distance, m

<u>Subscripts</u>

ℓ = liquid (water)

m = melt (corium)

v = vapor (steam)

1 = melt

2 = vapor

L = leading edge

J = jet

SAT = saturation

W = water

f = corium

c = crust

s = steel

<u>Greek</u>

α = thermal conductivity, m^2/s

β = coefficient of thermal expansion, K^{-1}

σ = surface tension, N/m

δ = thickness, m

μ = kinematic viscosity, kg/m•s

ν = dynamic viscosity, m^2/s

ρ = density, kg/m^3

θ = angle, radian

ω = growth rate of disturbance, 1/s

<u>Conversion Table</u>

1 meter	= 39.37 inch
1 Joule/kg•K	= 2.39×10^{-4} BTU/lbm °F
1 Joule/kg	= 4.30×10^{-4} BTU/lbm
1 W/m^2•K	= 0.1762 BTU/ft^2•hour•°F
1 W/m^2	= 0.3172 BTU/ft^2•hour
1 W/m•K	= 6.938 BTU•inch/ft^2•hour•°F
1 MPa	= 145.04 psi
1 m/s	= 3.2808 ft/s

1 kg/m^3	= 6.2428 lbm/ft^3
1 kg/s	= 2.2046 lbm/s
1 Pa•s	= 2.089×10^{-2} $lbf \cdot s/ft^2$
1 N/m	= 6.852×10^{-2} lbf/ft

ASSESSMENT OF THE INTEGRITY OF TMI-2 LOWER HEAD INSTRUMENT PENETRATION WELDMENTS

by

S. K. Wang, J. J. Sienicki, and B. W. Spencer

ABSTRACT

An analysis has been carried out to assess the potential of a melting attack upon the reactor vessel lower head and incore instrument nozzle penetration weldments during the TMI core relocation event at 224 minutes. Calculations were performed to determine the potential for molten corium to undergo breakup into droplets which freeze and form a debris bed versus impinging upon the lower head as one or more coherent streams. The effects of thermal-hydraulic interactions between corium streams and water inside the lower plenum, the effects of the core support assembly structure upon the corium, and the consequences of corium relocation by way of the core former region were examined.

It was found that for the best estimate case in which the corium entered the lower plenum by draining over a major portion of the circumference of the core former region, the corium is calculated to undergo extensive breakup to form a debris bed. The formation of such a debris bed avoids the prediction of any significant thermal attack on the penetration welds. However, even if the bounding severe assumption is made that all of the corium entered the lower plenum in the form of a single coherent stream (i.e., jet), the presence of the core support assembly structure would have caused the single corium jet to be ultimately broken up into an assumed minimum of four smaller streams. (A mechanistic treatment would likely yield a greater number of streams.) For the resulting impingement of the four jets draining from the elliptical flow distributor plate, no melting attack is predicted for the vessel lower head. For this case, the temperature at the vessel wall inner surface is calculated to attain a maximum value of 1200 Kelvins (1700 degrees Farenheit) remaining well below the material melting temperature [~1800 Kelvins (2800 degrees Farenheit)].

I. INTRODUCTION

A. Background

Planning for the removal of the core support assembly (CSA) from the TMI-2 reactor vessel includes the consideration of the accidental dropping of a portion of the CSA structure into the lower head. Of principal interest is the condition of the weldments securing the incore instrument nozzles to the lower head vessel wall. If a weldment were to fail during a load drop event, the consequence could be a drainage of water from the reactor vessel. Concern for the integrity of the penetration welds arises from the presence of corium debris inside the lower head. Heat transfer from molten corium is a potential means of heating up and melting the weld material such that the weldment no longer serves to adequately secure the incore instrument nozzle to the lower head. Thus, the circumstances under which the corium relocated into the lower head and the physical state of the corium when it potentially came into contact with the lower head wall or the individual weldments is of major significance.

According to current perception of the TMI accident, corium largely relocated into the lower head at approximately 224 minutes into the accident.[1] An analysis has been carried out to examine the direct threat to the weldments resulting from the corium relocation event. Calculations were performed of the thermal-hydraulic interactions of corium with water and structure inside the lower head. Predictions of the state of the debris inside the lower head were made in light of the results of the Core Coolant Mixing (CCM) reactor material experiments[2] recently carried out at Argonne National Laboratory. In the CCM tests, predominantly UO_2-ZrO_2 corium mixtures were injected into steel test sections containing water and simulating features of the lower head region to provide data on corium breakup behavior and debris formation.

To threaten the weldment integrity, it is necessary that a significant thickness of the weld be melted and ablated away, or heated to a temperature approaching the melting point. Previous studies of the interaction of corium with the lower head have identified two idealized mechanisms by which failure may occur. The first mechanism is the postulated direct impingement of a stream of molten corium upon a weld as a localized and coherent jet.[3] High heat transfer rates may be calculated inside the impingement zone in which the jet splashes off of the lower head or is redirected to flow horizontally over the underlying substrate. The high impingement region heat fluxes can be predicted to erode the weld thickness over a timescale of a few tens of seconds, unless the mitigative effects of water or structure are taken into account. The second mechanism is the postulated accumulation of a large mass of molten corium atop the lower head and penetration welds.[4] If the removal of energy from such a layer due to quenching by overlying water is ignored, then significant heatup and melting of weldments and the lower head may be calculated. (In fact, the debris at TMI was coolable.) This is a relatively much slower process requiring tens of minutes or more.

There are at least three features of the relocation of corium into the lower head during the TMI-2 accident which act to preclude the realization of both these weldment failure mechanisms. First, corium draining through the lower head as a jet or series of jets will undergo breakup due to its interaction with water. In particular, the corium is broken up into a dispersion of molten droplets which lose energy by heat transfer as they settle through the water. A corium stream will undergo complete breakup after passing through a suitable depth of water which is dependent upon a number of conditions including the jet diameter, velocity, and corium temperature as well as the water temperature. For shorter distances, the extent of breakup may not be complete. However, in this case, the breakup processes still tend to reduce the corium mass remaining in the form of a coherent jet. Freezing of the droplets formed as they settle through the water will result in the formation of a debris bed inside the lower head. For complete breakup and freezing into particles of sufficiently large diameters, water will readily ingress the bed to remain present at the surface of the weldments and lower head steel, quench the corium particles, and remove the subsequent decay heat generation.

Second, the core support assembly (CSA) beneath the TMI core incorporates three massive plate members referred to as the flat distributor plate, the lower grid forging, and the elliptical distributor plate. The flat distributor plate which is the uppermost member has holes of diameter 8.23 centimeters (3.24 inches) which are smaller than those of the underlying forging

[16.5 centimeter (6.50 inch) diameter holes] and elliptical distributor plate [15.2 centimeter (6.0 inch) diameter holes]. The holes penetrating the lower forging and the elliptical plate are not coincident and do not provide a straight-shot pathway from the core to the vessel bottom. As a molten corium stream impacts upon a particular plate, it will tend to splash and spread over the plate and drain through the nearby holes. These processes and the CSA configuration tend to break up a single stream into several streams and enhance the breakup of streams into droplets. Because of the presence of the CSA which has been observed to be essentially intact in defueling examinations,[5] it is impossible for corium to drain as a single coherent stream from the elevation of the bottom of the core to the lower head vessel wall.

Third, the TMI defueling examinations have revealed that the corium relocated from the molten core region to the lower head predominantly by way of the core former region (CFR) located between the vertical baffle plates immediately surrounding the fuel assemblies and the core barrel. Corium was observed to have spread horizontally within the CFR with solidified debris found over approximately three-fourths of the CFR circumference.[6] The principal pathways for downward flow through the horizontal former plates are the eighty relatively small diameter [3.33 centimeters (1.31 inch)] flow holes through each former plate. Consequently, corium drainage from the CFR was likely distributed over a large number of flow holes. In particular, the corium did not exit from the CFR in the form of a single coherent jet. The smaller diameter streams draining from the flow holes will break up more readily giving rise to droplet generation, droplet freezing, and debris bed formation.

The breakup of corium streams into droplets which freeze and form a debris particle bed precludes a significant direct thermal attack upon the incore instrument nozzle weldments. For large-size particle diameters exceeding roughly 1 millimeter (0.039 inch) as predicted by the current analysis and consistent with the results of the CCM experiments, detailed experimental studies of the entry of water into and quenching of debris beds have demonstrated an efficient two-dimensional quench process. Specifically, it has been established that when water is delivered to the upper surface of a heated particle bed, a significant portion of the water penetrates directly to the bottom of the debris through the formation of localized water channels.[7,8]

Water thus immediately begins to accumulate as a layer at the bottom of the bed. This water layer grows in depth as a quench front rises upward through the debris in a more or less one-dimensional fashion. Concurrently, water in the regions interstitial to the channels propagates downward through the bed behind a downward moving quench front. The major point here is that when debris accumulates as a bed atop the lower head vessel wall or the penetration welds, water will remain present adjacent to the underlying substrate lower head steel or weld material. The water is expected to prevent the welds from undergoing any significant heatup. Water also provides a means of quenching the debris particulate and subsequently removing its decay heat.

The present analysis investigates the conditions of the corium as it accumulated inside the lower head during the TMI relocation event which occurred at about 224 minutes into the accident. Current state-of-the-art calculations of the interaction of corium with water in the lower head were carried out consistent with configurational features of the TMI system and data recorded during the accident. The heatup of the lower head wall was calculated.

B. <u>Approach</u>

It was found useful to perform calculations for three cases which correspond to investigation of the three features of the TMI corium relocation discussed above.

i) A scoping calculation was carried out to ascertain the effects of water alone. This calculation bears no relation to reality because it does not account for the effects of the core support assembly structure or the spreading flow of corium inside the core former region. Instead, all of the corium is assumed to drain downward as a single jet. Only the effects of the interaction of the corium jet with surrounding water are modeled as a breakup mechanism. The purpose of this calculation is to characterize the potential for breakup due to corium jet-water interactions alone.

ii) A bounding severe case in which corium is assumed to drain from the CFR at a single nonvarying location in the form of a localized jet. However, the effects of the CSA in breaking up the corium into several streams as it successively drains through the various plates are modeled. The interactions of each corium stream with water are included.

iii) A best estimate case accounting for the lateral spreading of corium within the CFR. The corium is assumed to drain simultaneously through the flow holes in the bottom most horizontal core former plate to enter the underlying water interior to the CSA. Specifically, corium is assumed to drain over a maximum of three-fourths of the circumference of the CFR as observed in defueling examinations. The effects of the CSA as modeled in Case ii were unnecessary owing to the extensive breakup and quench in this case. Jet breakup is due solely to the simultaneous interaction with water of all of the corium streams draining from the flow holes.

It shall be demonstrated that for Case iii, the jet breakup calculations predict that virtually all of the corium is broken up into droplets which cool and solidify while falling through the water pool to settle out upon the lower head as a particle debris bed. Although a fourth case could have been defined in which the effects of both the CSA and CFR spreading are simultaneously considered, such a calculation was not necessary.

The heatup and ablation of the lower head are predicted only for the impingement of a downward directed corium jet. Following impingement, corium might flow laterally over the lower head inner surface to impinge upon the sides of the instrument penetration nozzles. This process involves several uncertainties including the degree to which the impinging corium splashes up off of the lower head as opposed to flowing along it. Calculation of the thermal heatup of the nozzles and weldments from this mode of contact lies beyond the scope of the present analysis and was not attempted.

In carrying out the analysis, input to the calculations has been selected to be consistent with what is currently known about the TMI-2 accident. In some instances, it has been necessary to estimate conditions inside the reactor vessel. Of specific importance here is the temperature of water residing in the lower head at the time of the relocation event. An examination of previous estimates of subcooling was carried out. Because the earlier studies provide widely divergent values for the amount of subcooling, as estimate of the subcooling and its range of uncertainty was performed as part of the current analysis. The dependency of the subcooling upon uncertainties in thermal-hydraulic processes prior to the relocation event was scoped. In determining the subcooling, use was made of the recorded primary system pressure as well as the recommended flowrate and temperature of water delivered by the high-pressure injection capability of the makeup pumps.

The role played by control material which underwent melting and may have relocated into the lower head is currently an uncertainty. Calculations were carried out to determine the breakup and quenching behavior of molten absorber alloy, in order to ascertain how the presence of control material might influence interactions of corium with the lower head wall.

A discussion of the accident data, estimates of in-vessel conditions, and assumptions incorporated in the analysis is presented in Section II. The results of the corium jet breakup calculations for the three cases are discussed in Section III. Also included here is a comparison of the predicted pressurization of the primary system reflecting net steam formation from the calculated corium-water interactions during the relocation event versus the measured pressures. The calculations of the heatup and potential ablation of the lower head in the presence of an impinging corium jet are presented in Section III. Overall conclusions and observations are discussed in Section IV. Appendix A discusses in detail the thermophysical properties for corium used in the analysis and documents the data sources upon which the properties are based. The thermophysical properties for the vessel lower head are similarly documented in Appendix B. The corium jet breakup model employed in the analysis is discussed in detail in Appendix C. Appendix D presents calculations of the lateral relocation of corium as it drained through the core former region. Calculations of the behavior of melted control material which may have entered the lower plenum are discussed in Appendix E. Finally, Appendix F documents the analytical model employed to calculate the heatup and ablation of the lower head resulting from the impingement of a corium jet.

II. TMI-2 MOLTEN CORE RELOCATION PHENOMENA AND CONDITIONS

A. Summary of Relocation Event

According to current perception of the TMI-2 accident, at 224 minutes after the turbine tripped, approximately 25 tonnes[1] (55,000 pounds) molten fuel material (referred to as corium) relocated from a pool contained by a surrounding crust into the vessel core former region (CFR) and the lower plenum. The probable flow path for the molten corium was to impinge upon the vertical baffle plate structure surrounding the core. Following the breaching of the baffle plate, corium which flowed through a hole in the baffle plate to enter the CFR would accumulate upon the horizontal core former plate immediately below the breach. A recent inspection[4] inside the CSA revealed that as much as ~4.2 tonnes (9200 pounds) of debris may be in the region between the core barrel and core former baffle plates. Presumably, the remaining ~20 tonnes (44000 pounds) of molten corium drained through the core lower structure and impacted on the vessel lower head.

It is believed that failure of the crust in the southeast quadrant of the core permitted molten corium to flow out of the pool and impinge upon the vertical baffle plates surrounding the core. Observations from the defueling operations revealed that the R6, P5, and P4 baffle plates (see Figure 3.5 for core coordinates) are missing, presumed melted, in the region below former plate #5 to midway between former plates #6 and #7. As the depth of the molten corium layer increased, the corium then proceeded to spread laterally over the former plate under the influence of gravity. However, the extent of corium spreading would be restricted by drainage through the flow holes in the core former plate. In particular, each former plate contains eighty circular holes each having a diameter of 1 5/16 inch (0.0333 meter). Evidence shows that approximately three-fourths of the CFR circumference were covered by solidified debris. Ultimately, corium drained through the peripheral part of the lower ribbed grid plate to enter the lower head region interior to the CSA. Examination of the CSA structure has shown the presence of corium over a similar extent of the vessel circumference.

In order to assess the vessel heatup and possible ablation due to the impingement of the relocated core material, various postulated relocation paths are assumed and analyzed. The breakup and quench of corium jets draining through different relocation paths and the following thermal attack on the vessel lower head are discussed in Section III. An attempt was made to assess the relocation behavior by comparison of the calculation of the pressurization data during the relocation event with the TMI reported data.

B. Initial Conditions of Corium Jet/Water Interaction

1. Initial Temperature of Corium Jet

Based on the overall energy balance between the heat production rate of a molten fuel pool and the heat loss rate of the pool to its hemispheric crust, the nominal corium superheat[9] immediately prior to the relocation event was estimated to be ~200 Kelvins (360 Farenheit degrees). Thus, an initial temperature of 3050 Kelvins (5030 degrees Farenheit) was assumed for the corium jet relative to the corium liquidus temperature of 2850 Kelvins (4670 degrees Farenheit).

2. Duration of Corium Relocation

As shown in Figure 2.1,[10] the source range monitor (SRM) response, reactor coolant system (RCS) pressure response, and measured cold leg temperatures all indicated that a global change in the core and reactor vessel condition over a time span estimated to be 30 to 120 seconds. For an assumed jet diameter, the velocity of the impinging corium stream depends on the relocation time. Based on a hydrodynamic/thermal model of jet breakup as described in Appendix C, the jet velocity strongly characterizes the jet breakup behavior such as the steam generation during corium-water interaction and a concomitant increase in the primary system pressure. It is believed that the SRM response is a direct indicator of change in the core configuration since the SRM directly measures neutron leakage from the core region. According to Figure 2.1, a significant increase of the SRM count rate occurs at 224.25 minutes and reaches its maximum at 225.75 minutes, and then indicates a normal decay profile. Therefore, the corium relocation time was estimated to be 90 seconds. This value was assumed exclusively in the current analysis.

C. Initial Water Temperature and Water Inventory in Vessel Lower Head

During the time interval between when the turbine tripped and the B-loop pump started at 174 minutes of the TMI-2 accident, about half of the primary system coolant was lost to the containment through the stuck open PORV on the pressurizer.[11] The core water level at 174 minutes was estimated to be 0.5 to 1.0 meter (1.6 to 3.3 feet) above the bottom of the active core,[12] and the water temperature was very likely to be saturated [560 Kelvins (550 degrees Farenheit)] based on the hot leg and cold leg water temperature data.[13] At 200 minutes, the high-pressure injection (HPI) system was actuated for approximately 17 minutes. The onset of HPI provided a strong condensation and cooling source within the cold legs and caused the primary system pressure to decrease rapidly as shown in Figure 2.2. As a result, the pressurizer drained water into the A-loop hot leg and into the core.[11] Since the temperature of HPI water was much lower [~294 Kelvins (70 degrees Farenheit)], the core water would be subcooled which significantly influences the steaming rate and vessel pressurization during the corium relocation. In order to estimate the water temperature in the vessel lower head, the HPI water temperature transient was

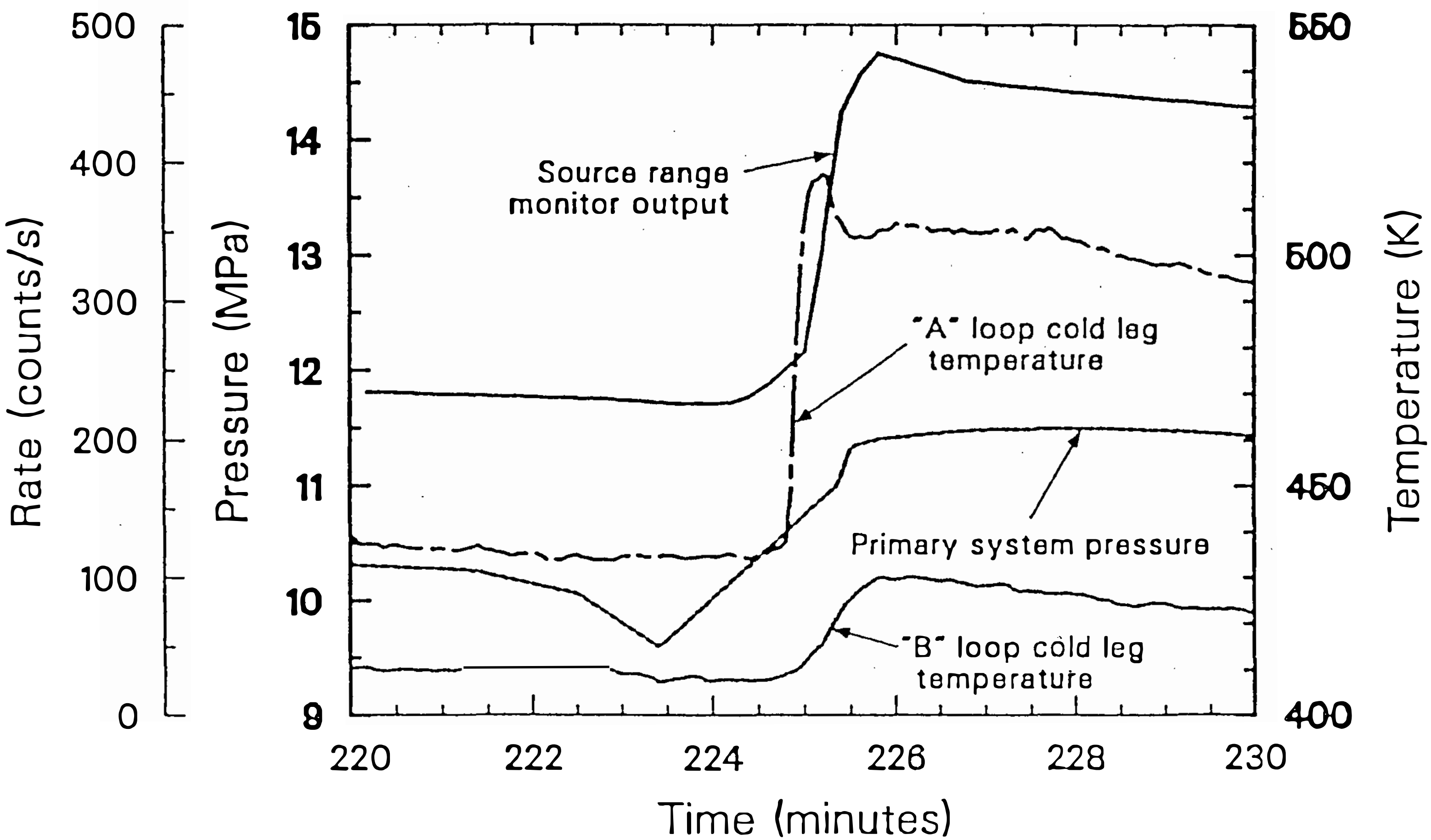

Figure 2.1 TMI-2 Recorded Data

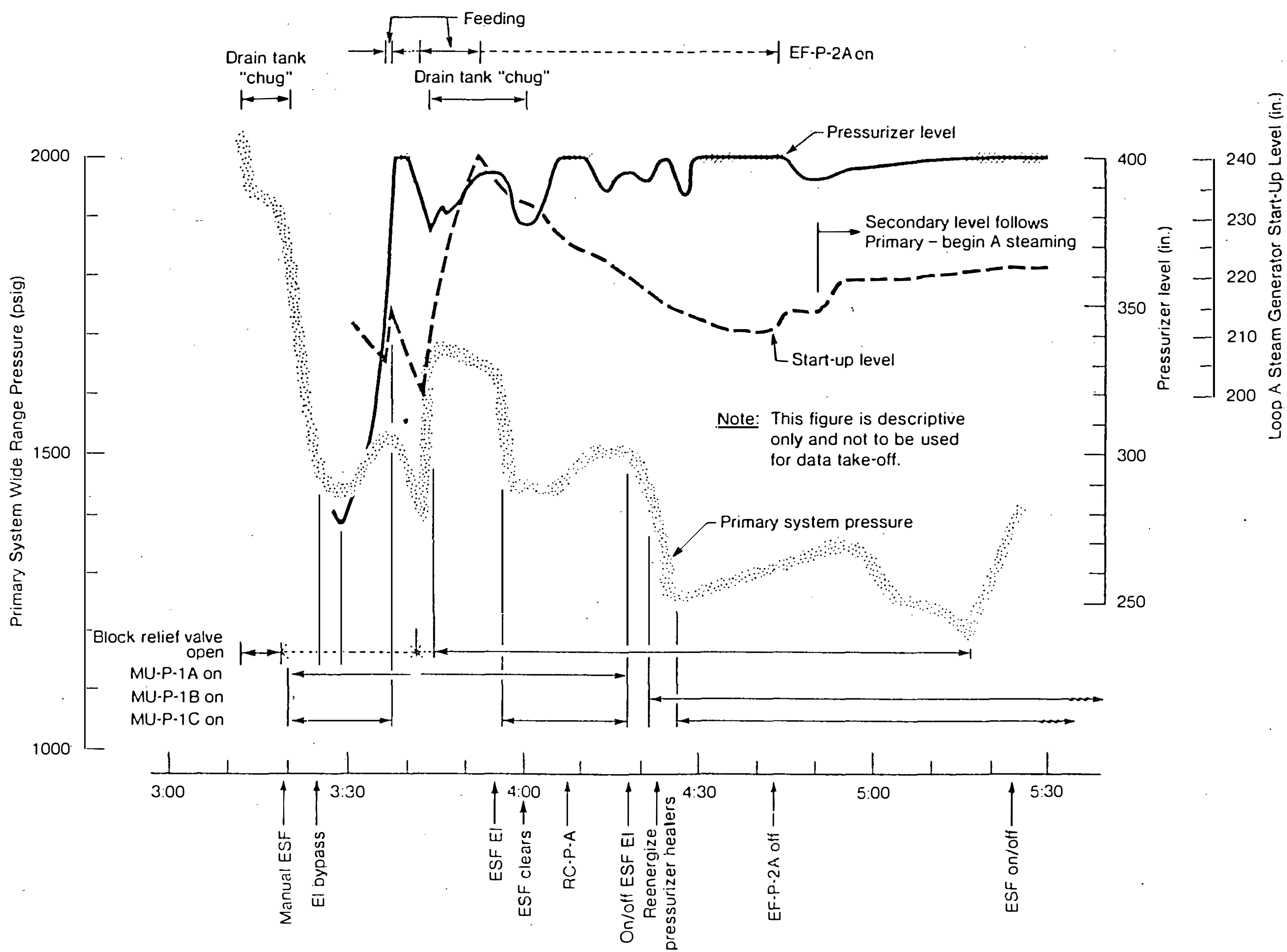

Figure 2.2 Correlation of Events 3:30 to 5:30

analyzed based on the recorded pressure data and the recommended HPI injection rates. Assuming that the steam/hydrogen mixture behaves as a perfect gas during the injection of HPI water, then the pressure transient can be related to the condensation rate and volume change rate as expressed below:

$$\frac{\partial P}{\partial t} \simeq \left(\frac{\partial m}{\partial t}\right) \frac{R_v}{\bar{V}} T - \frac{P}{\bar{V}} \frac{\partial \bar{V}}{\partial t} \tag{2.1}$$

where

P = pressure, MPa,

m = mass of steam, kg,

R_v = universal gas constant, $R_v = 8.2 \times 10^{-6}$ MPa•m^3/(gmole-K),

$\bar{V}$ = volume of steam/hydrogen mixture, m^3

T = temperature of steam/hydrogen mixture, K.

The change of the volume of steam/hydrogen mixture in the primary system can be calculated based on the flow rate of HPI and the water level in the pressurizer, i.e.,

$$\frac{\partial \bar{V}}{\partial t} = \left.\frac{\partial \bar{V}}{\partial t}\right|_{HPI} + \left.\frac{\partial \bar{V}}{\partial t}\right|_{pressurizer} \tag{2.2}$$

The estimated HPI injection rate of 60.5 kilograms per second (480000 pounds per hour) as recommended in Reference 14 was assumed. The pressurizer water level is also shown in Figure 2.2.

During the first seven minutes of HPI injection, the strip chart record of the primary system pressure indicates that the pressure dropped about 400 pounds per inch square (2.7 megapascals), i.e., an average depressurization rate of about -7.56 kilopascals per second (-11 pounds per inch square per second). Therefore, the steam is condensed at a net rate of -7.79 kilograms per second (-61700 pounds per hour) during this period according to Equation 2.1. However, the steam condensation due to the HPI injection and the steam generation due to flashing and core steaming all contribute to the net steam condensation rate, i.e.,

$$\frac{\partial m}{\partial t} = \left.\frac{\partial m}{\partial t}\right|_{condensation}^{HPI} + \left.\frac{\partial m}{\partial t}\right|_{flashing} + \left.\frac{\partial m}{\partial t}\right|_{core\ steaming} \tag{2.3}$$

Assuming thermodynamic equilibrium and saturation conditions, the average flashing rate due to the depressurization during this period is estimated to be 11.06 kilograms per second (92000 pounds per hour). The steaming rate due to the boiling off the surface of the degraded core debris is estimated using the Zuber flat plate critical heat flux expression:[15]

$$\left.\frac{\partial m}{\partial t}\right|_{core\ steaming} \simeq 0.14\ \rho_g \left[\frac{\sigma g(\rho_\ell - \rho_v)}{\rho_v^2}\right]^{1/4} A \tag{2.4}$$

$$\simeq 15\ kg/s$$

Therefore, an average condensation rate due to the HPI injection is estimated to be -33.85 kilograms per second (-268100 pounds per hour). The HPI water temperature immediately prior to entering the vessel lower head can be evaluated based on the calculated HPI condensation rate. Applying mass and energy balance on the control volume as shown in Figure 2.3, it yields:

mass equations:

$$w_{out} = w_{in} + \int_o^z \dot{m}_i\ L\ dz \tag{2.5}$$

energy equation:

$$\frac{\partial T}{\partial z} = \frac{1}{wC_p}\left\{\dot{m}_i L[h_{fg} + C_p(T_{SAT} - T)] + q_s'' L\right\} \tag{2.6}$$

where

T = HPI water temperature, K,

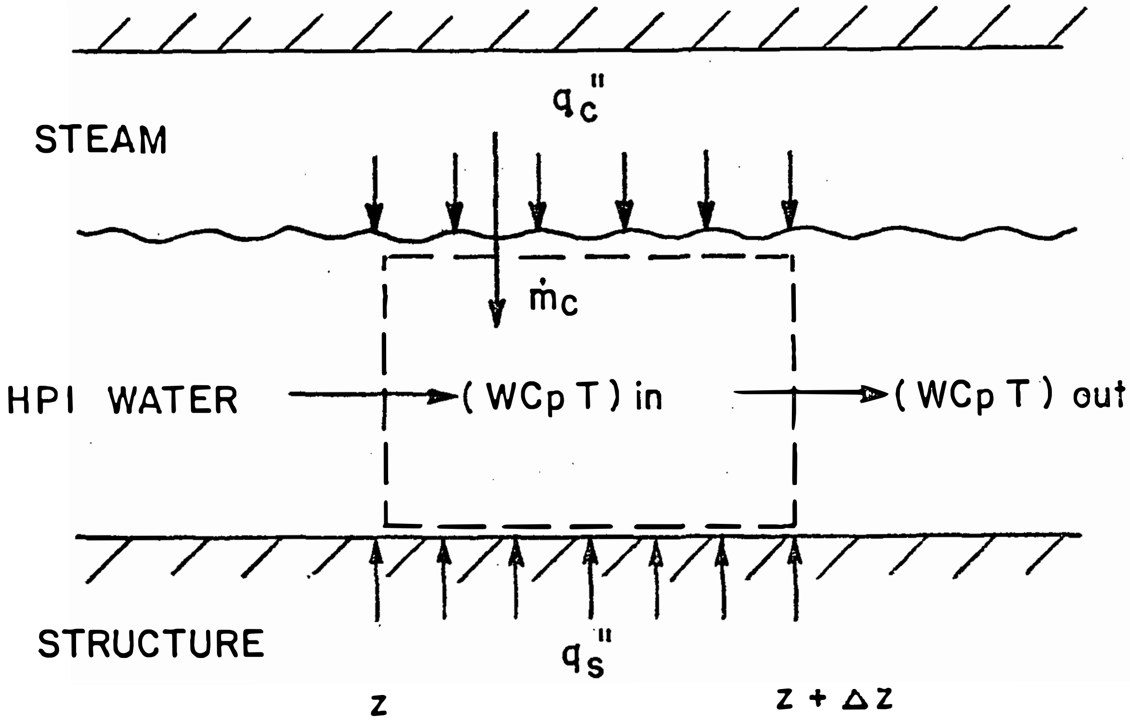

Figure 2.3 Schematics of HPI Water Heatup

w = HPI water flow rate, kg/s,

L = width of steam/water interface, m,

$\dot{m}_i$ = mass flux of steam condensation, $kg/m^2 \cdot s$,

q''_s = heat flux from structure, W/m^2,

T_{SAT} = temperature of steam, K.

The heat flux between the HPI water and structure can be evaluated by assuming transient heat conduction to a semi-infinite region. Thus,

$$q''_s = \frac{k(T_{SAT} - T)}{(\pi \alpha t)^{1/2}} \tag{2.7}$$

where

k = thermal conductivity of water, W/m•K,

α = thermal diffusivity of water, m^2/s,

t = z/U, sec,

U = velocity of HPI water, m/s.

The HPI flow rate is ~15 kilograms per second (118800 pounds per hour) (per leg). The water stream is estimated to attain a depth of 8 centimeters, a width L ~20 centimeters, and a velocity U ~1 meter per second in the cold legs. When the HPI water stream enters the downcomer, the stream would impinge upon the core barrel and fall along it as an attached film flow. However, there are twenty clips (obstacles) attached to the core barrel to support the upper end of the thermal shield.[16] The HPI water draining down the barrel would be spread laterally by those clips. Based on the orientation of these clips, a width L ~1 meter is estimated for the film flow on the core barrel. Equations 2.5 and 2.6 were solved to yield the HPI temperature transient on the cold leg and along the downcomer. Figure 2.4 shows that the HPI water temperature increases by ~150 Kelvins (270 degrees Farenheit) when it enters the vessel lower head and mixes with the vessel water.

At 207 minutes when the pressurizer stopped draining, the primary system pressure began to rise. This is a direct result of the reduced HPI-induced

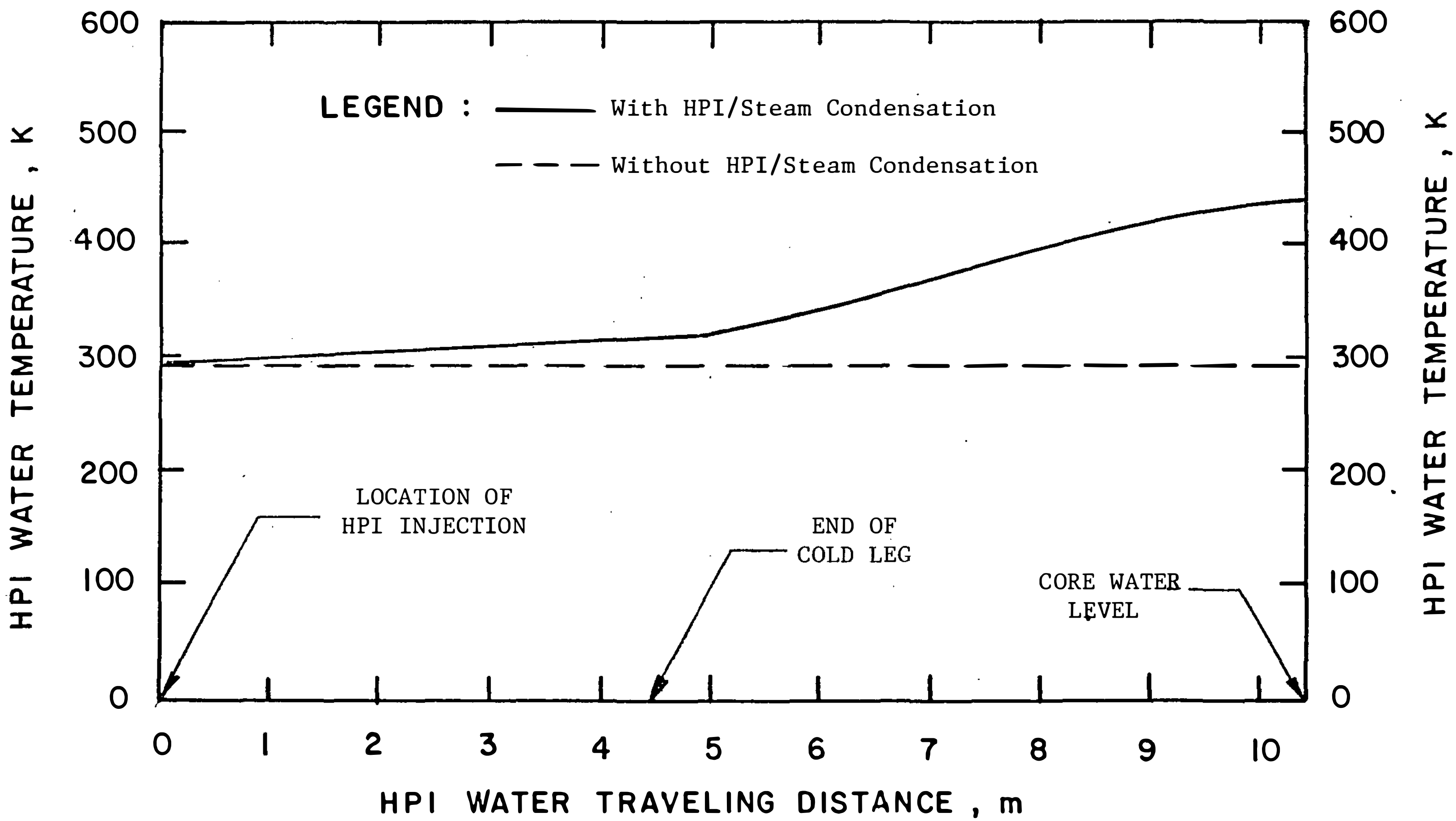

Figure 2.4 HPI Water Heatup

steam condensation due to the water level rising above that of the primary piping nozzles and preventing steam from entering the cold legs from the vessel upper plenum.[11] As a result, the cold legs accumulated hydrogen to essentially offset the condensation of steam. The HPI water temperature under this condition, i.e., no HPI/steam condensation, is estimated to increase only slightly as shown in Figure 2.4. The true HPI water is believed to fall within these two bounding cases.

When the HPI water enters the vessel lower head, it may mix with the water in the lower head or stay on the bottom portion of the lower head to form two stratified layers of water having different temperature due to the density difference. In order to determine the most likely water temperature in the lower head when the corium started to relocate, four different water temperatures, T_w, are estimated based on various assumptions.

<u>Case 1</u>:

$$\left.\frac{dm}{dt}\right)_{condensation}^{HPI} = -33.85\ \mathrm{kg/s};\ 200\ \mathrm{min} \le t \le 217\ \mathrm{min}$$

Water is homogeneously mixed in the lower head.

$T_w = 500$ K, $\Delta T_{sub} = 60$ K

<u>Case 2</u>:

$$\left.\frac{dm}{dt}\right)_{condensation}^{HPI} = \begin{cases} -33.85\ \mathrm{kg/s}; & 200\ \mathrm{min} \le t \le 207\ \mathrm{min} \\ 0; & 207\ \mathrm{min} \le t \le 217\ \mathrm{min} \end{cases}$$

Water is homogeneously mixed in the lower head.

$T_w = 470$ K, $\Delta T_{sub} = 90$ K

<u>Case 3</u>:

$$\left.\frac{dm}{dt}\right]_{condensation}^{HPI} = -33.85 \text{ kg/s}; \; 200 \text{ min} \le t \le 217 \text{ min}$$

Water is stratified in the lower head.

T_w = 443 K, ΔT_{sub} = 117 K

Case 4:

$$\left.\frac{dm}{dt}\right]_{condensation}^{HPI} = \begin{cases} -33.85 \text{ kg/s}; & 200 \text{ min} \le t \le 207 \text{ min} \\ 0 & ; \; 207 \text{ min} \le t \le 217 \text{ min} \end{cases}$$

Water is stratified in the lower head.

T_w = 355 K, ΔT_{sub} = 205 K

These four water temperatures will be used as the initial water temperature when the corium jet interacts with the water.

III. CORIUM JET BREAKUP AND TRANSIENT HEATUP OF VESSEL LOWER HEAD

The overall objective of this work is to estimate the maximum temperature and possible ablation the vessel wall may have experienced during the core material relocation. The transient heatup of the vessel wall depends strongly on the physical conditions of the core material relocation pathway through the vessel water. If the corium has been dispersed and quenched during the relocation, a coolable debris bed may be formed on the vessel lower head and a benign thermal transient may be expected. On the other hand, if the corium still retains the form of a coherent jet when it impinges on the lower head, the heat flux between the impinging corium and the vessel wall may be high enough to ablate the steel. In this section, the breakup of a corium jet (or jets) and temperature transient of the vessel wall will be analyzed and discussed based on the possible relocation paths and jet initial conditions as described in Section II. The vessel heatup is then calculated based on the physical conditions of the impinging jet (i.e., jet temperature, jet velocity, jet diameter, etc.). In order to assess the thermal transient of the vessel wall during the core material relocation, two existing models developed at ANL have been employed for these analyses. The models which are based upon data obtained from previous experiments carried out at ANL involve: i) the breakup and quench of jets of molten core materials flowing through subcooled (and saturated) water in a film boiling regime, and ii) the convective heat transfer for a jet of corium impinging on a steel surface.

A. Assumed Pathways of Corium Relocation

The breakup and quench of jets of molten core materials are analyzed based on the following assumed relocation paths:

Case i

This is a scoping case to ascertain the effects of water alone. A 6-inch (0.1524-meter) diameter corium is assumed to drain from the lower ribbed grid plate at the location below the lowest former plate as shown in Figure 3.1. The initial jet velocity is estimated based on the duration of injection as described in Section II. The vessel lower head will suffer a highest thermal attack resulting from relocation of corium through this path due to its physical configuration and the ignorance of the interaction with the CSA. As described in Section II, the water level was located above the core at the time of the relocation event. Specifically, water will be present when corium first enters the CFR. Subsequently, water may be expelled from the former region in the vicinity of the baffle breach and regions of greater corium accumulation (e.g., on a lower grid rib) due to vigorous steam generation in these regions. As a result, a further breakup and quench of the molten corium in these regions is not likely to occur. Thus, the corium jet is assumed to commence its interaction with water immediately beneath the lower ribbed grid plate as shown in Figure 3.1.

Case ii

Case ii is similar to Case i except the effects of the core lower structure on the corium jet breakup are considered. As shown in Figure 3.2, significant interaction with the water is expected to occur in regions I, II, III, and IV. Molten corium is assumed to reagglomerate and form multiple jets after it went through regions I, II, and III. A "straight-through" jet cannot exist in this geometry as shown in Figures 3.3 and 3.4. Similar to Case i, a 6-inch (0.1524-meter) diameter jet is drained from a 6-inch (0.1524-meter) hole on the lower ribbed grid plate at location R5 as shown in Figure 3.5. Molten corium accumulated on the flow distributor plate reagglomerates and

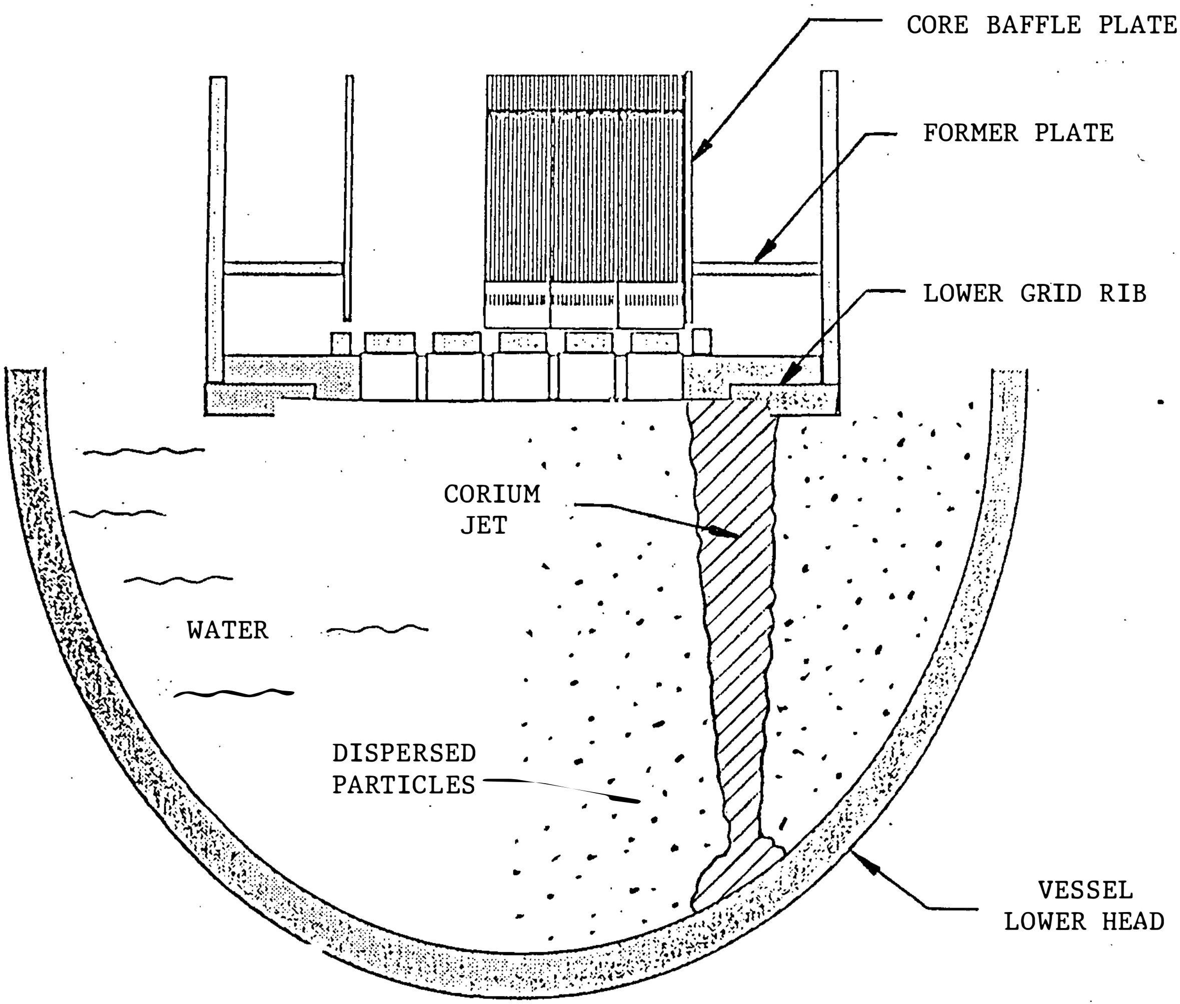

Figure 3.1 Schematics of Corium Relocation Ignoring Presence of Core Support Assembly (Case i)

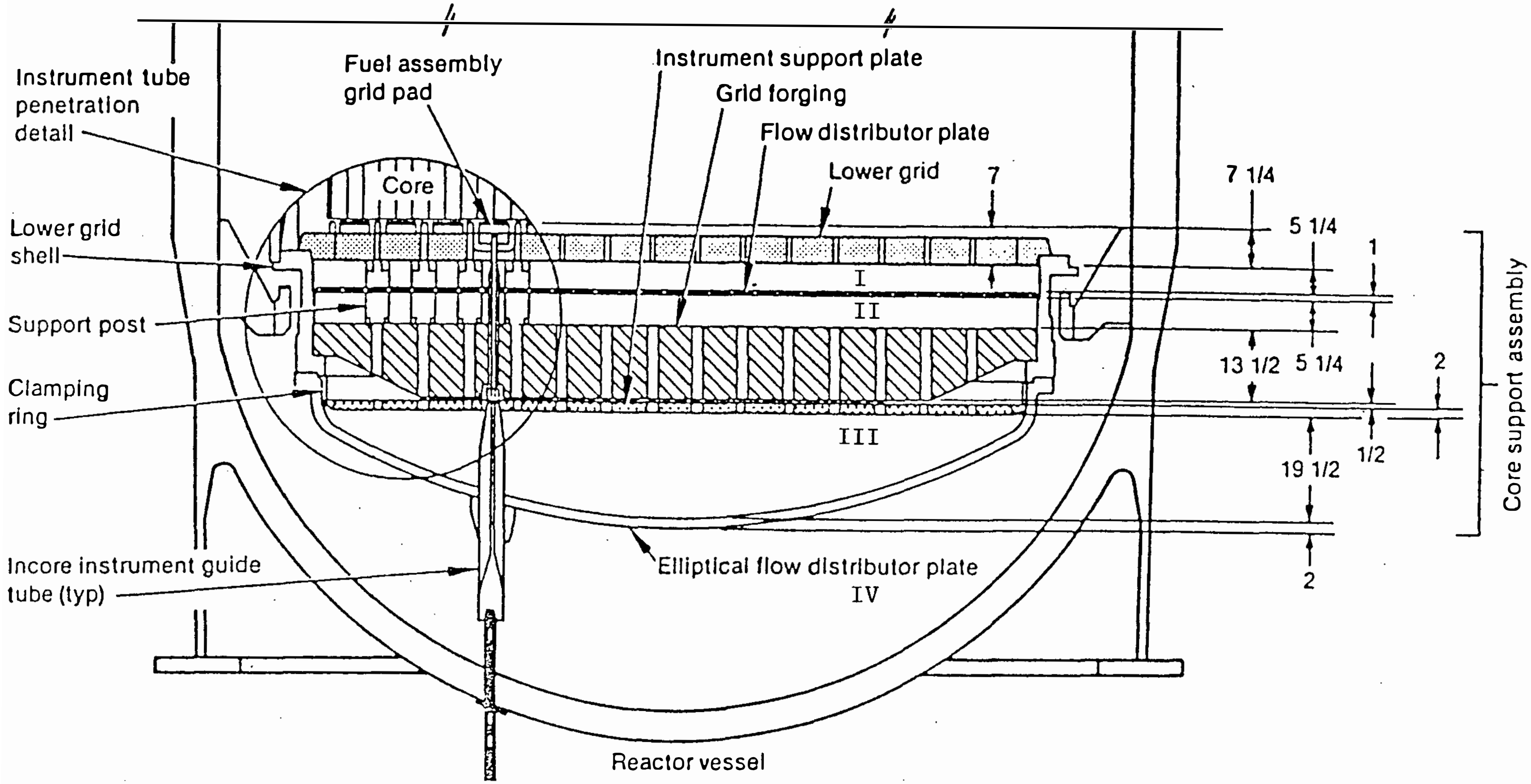

Figure 3.2 Details of Core Support Assembly Structure (Case ii)

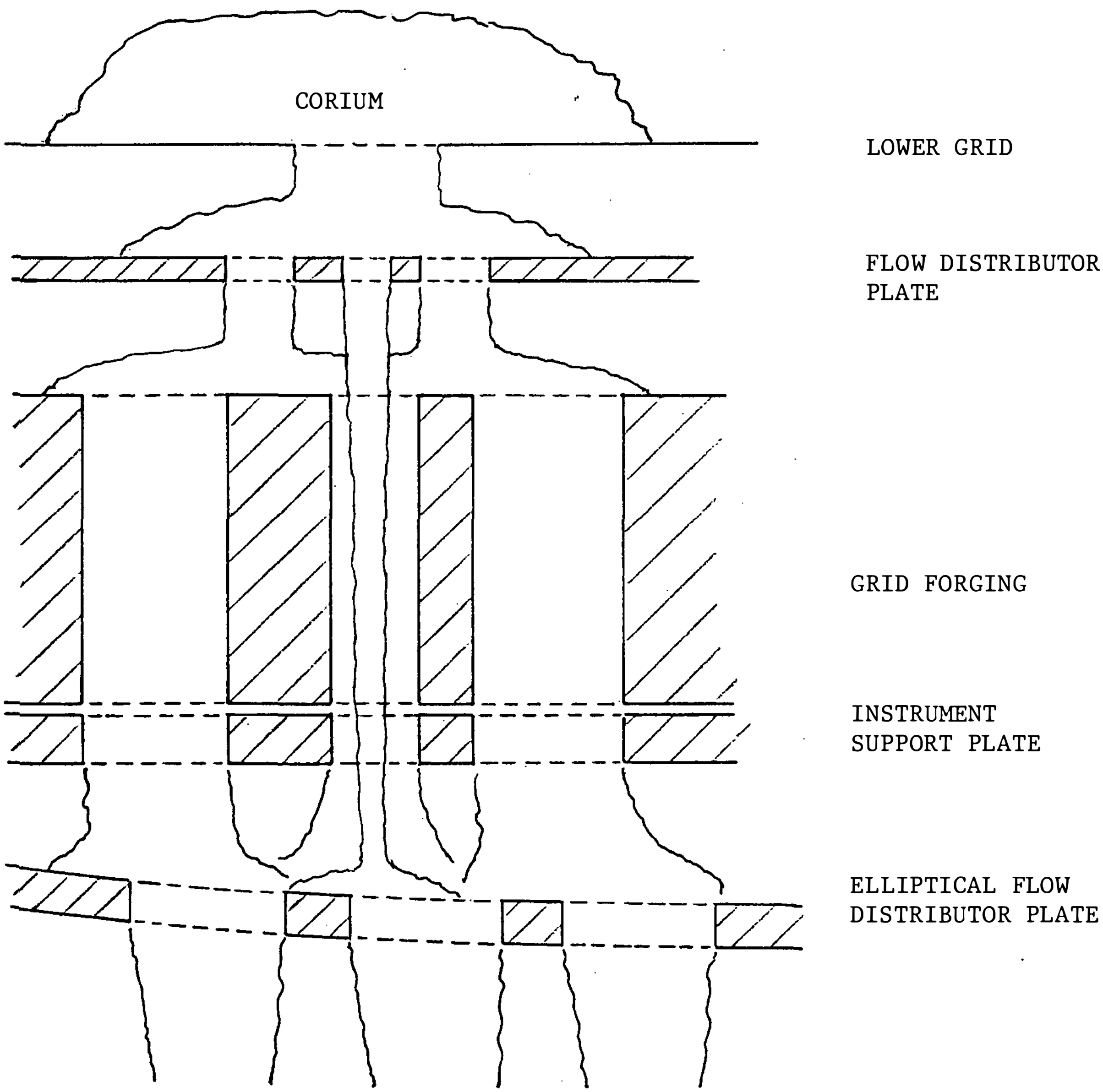

Figure 3.3 Side View of Corium Relocation from East Side Assumed in Case ii

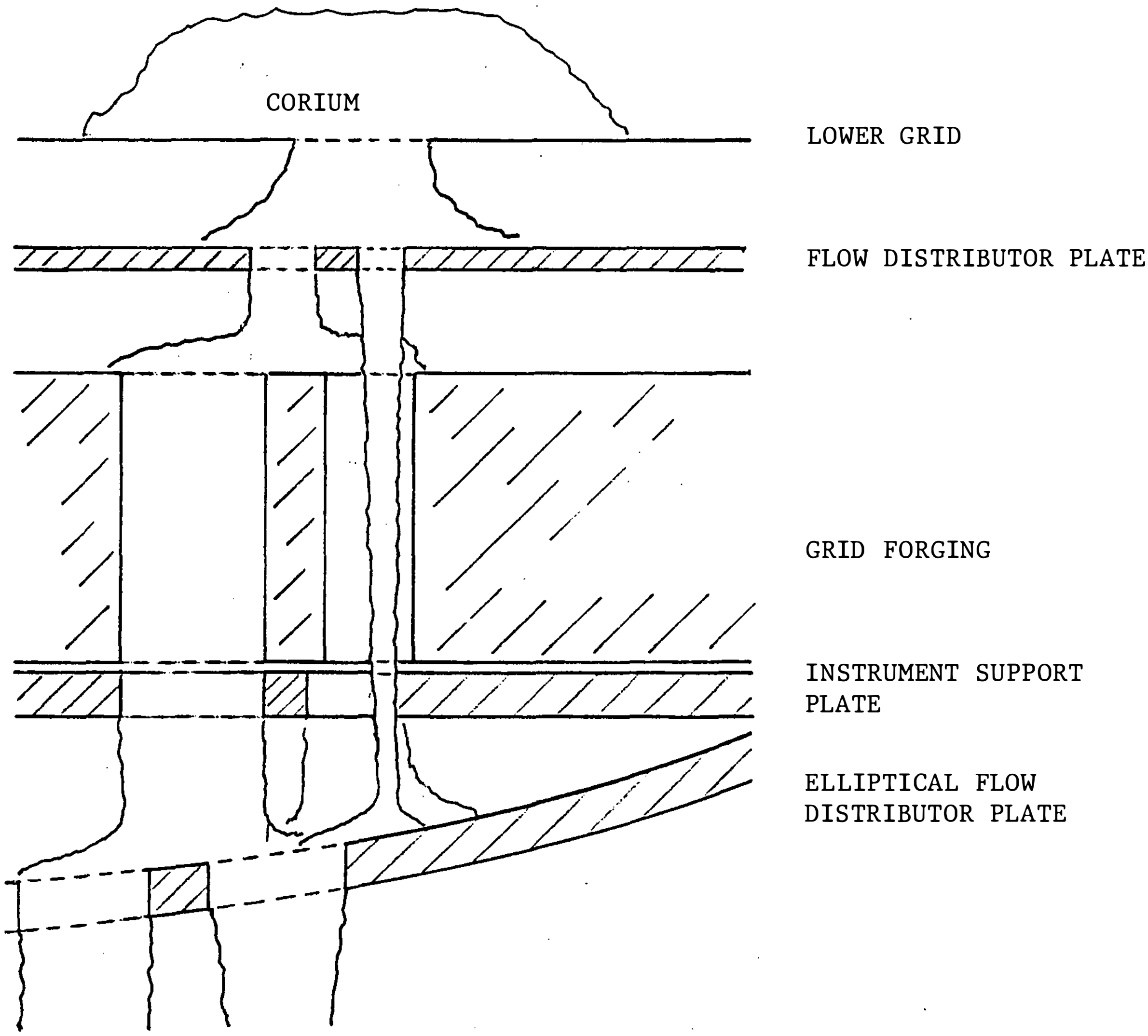

Figure 3.4 Side View of Corium Relocation from South Side Assumed in Case ii

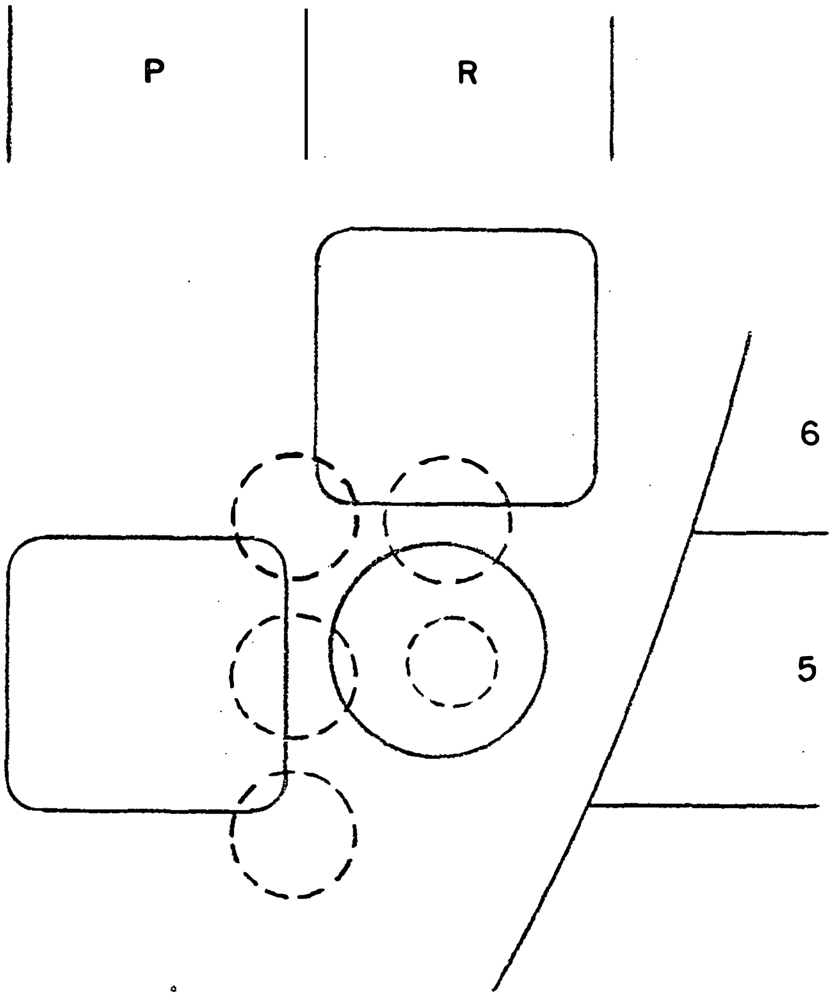

Solid symobls indicate lower grid sib

Dash symbols indicate flow distribution plate

Figure 3.5 Top View of Lower Grid Rib and Flow Distribution Plate Associated with Corium Relocation (Case ii) forms four 3 1/2-inch (0.089-meter) diameter jets and one 2 1/2-inch (0.0636-meter) diameter jet. Similar processes of reagglomeration occur on the upper surface of grid forging and the elliptical flow distributor plate as shown in Figures 3.6 and 3.7. The thermal attack upon the vessel lower head will be calculated based on four jets draining from the elliptical flow distributor plate. Due to the pre-fragmentation and multiple jets configuration, the corium streams will suffer more hydrodynamic dispersion and lose more energy when they impinge upon the vessel lower head. Therefore, relocation of the corium through this path will produce a less conservative yet more realistic thermal load on the lower head.

Case iiia

This is the best estimate case of the relocation based on the evidence of the in-vessel investigation. Examination of the core former region has revealed debris solidified between the lower core former plates over about three-fourths of the circumference of the core barrel. Additionally, examination of the core support assembly structure has shown the presence of corium over a similar extent of the vessel circumference. Therefore, it is plausible to assume that the corium drains through sixty out of the eighty holes on the lowest former plate into the vessel water as multiple jets. Since the jet size is small (1 5/16 inch [0.033 meter] diameter), a complete jet breakup is expected, and the additional dispersion by the CSA structure is thus ignored.

Case iiib

Similar to Case iiia, corium is assumed to drain through multiple 1 5/16-inch (0.033-meter) diameter holes on the lowest former plate into the vessel water. However, instead of simply assuming spreading over three-fourths of the circumference of the core barrel, the number of holes engaged in the corium drainage is estimated based on the corium spreading rate on the former plate and drainage rate through the holes underneath the corium layer. Furthermore, ablation-induced enlargement of the holes, which increases the local drainage and simultaneously decreases the spreading-induced lateral penetration, is also considered in this relocation path. An analysis of the spreading and drainage processes inside the core former region is presented in Appendix D. Corium relocated through this path is expected to yield a more conservative, yet more realistic thermal attack upon the vessel lower head than relocated through the path of Case iiia.

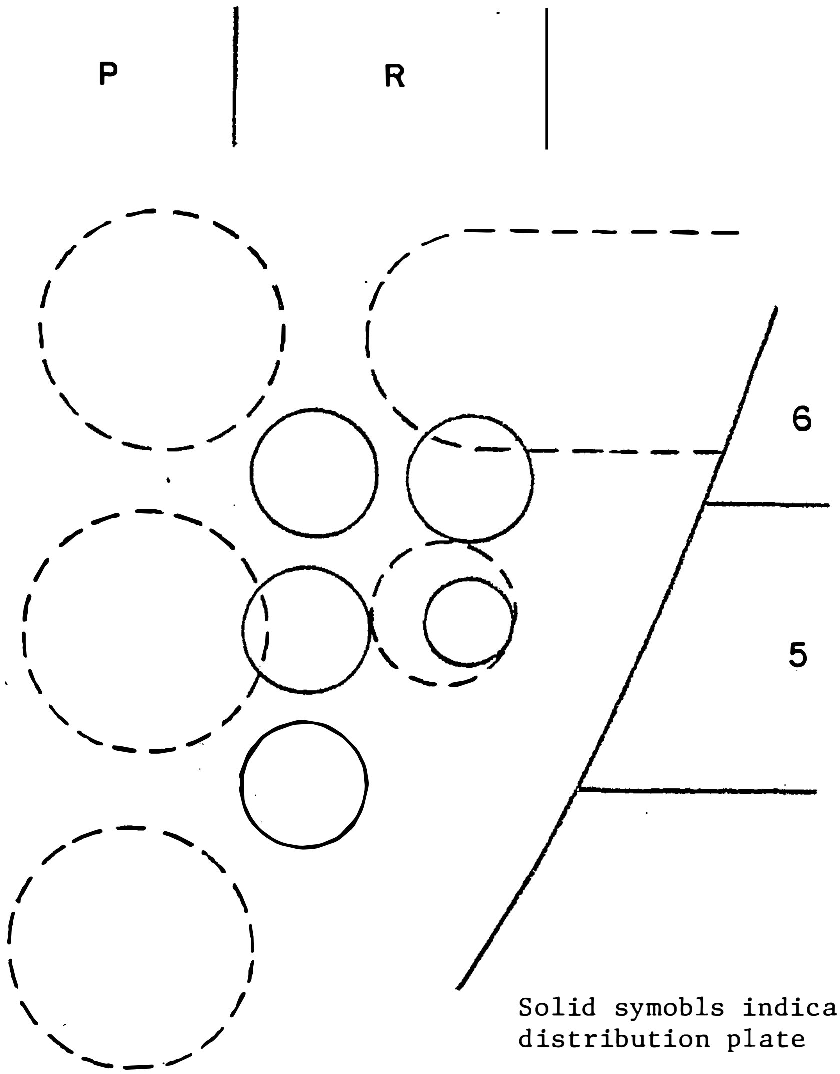

Solid symobls indicate flow distribution plate

Dash symbols indicate grid forging

Figure 3.6 Top View of Flow Distribution Plate and Grid Forging Associated with Corium Relocation (Case ii)

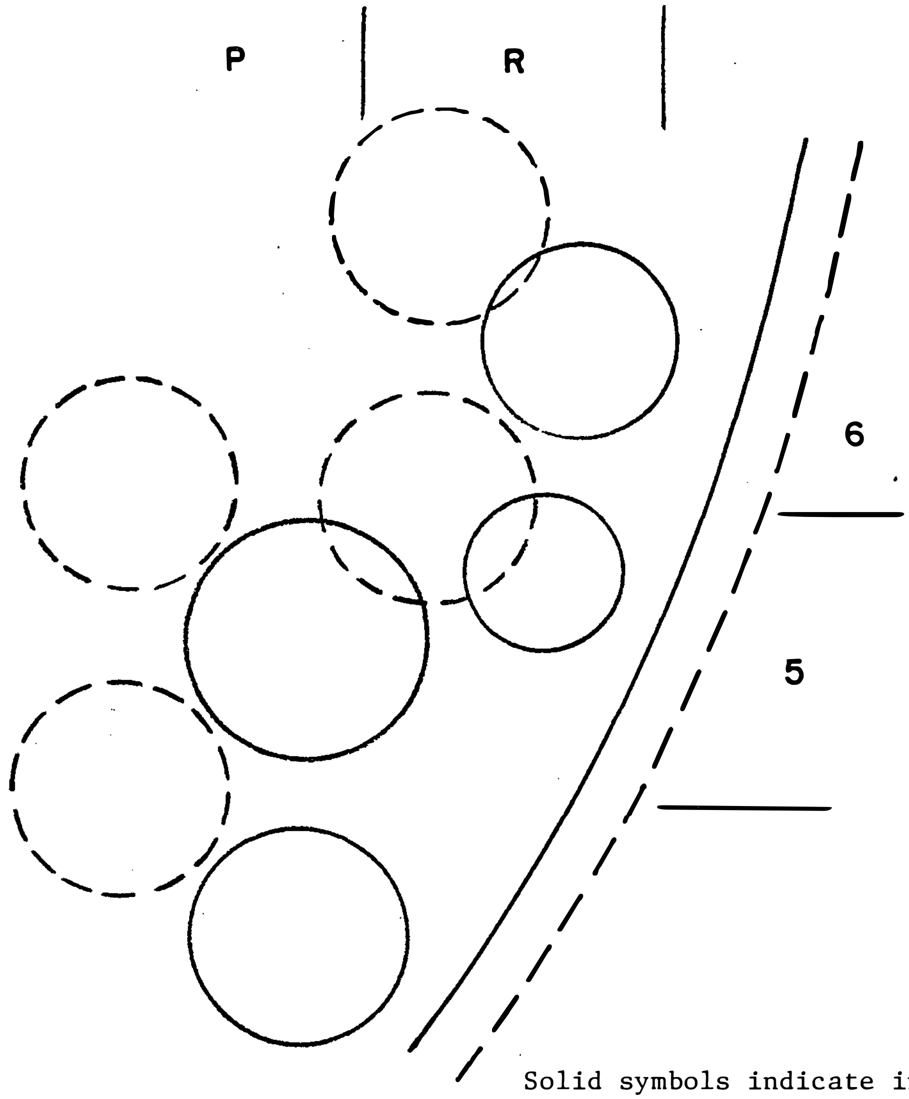

Solid symbols indicate instrument support plate

Dash symbols indicate elliptical flow distribution plate

Figure 3.7 Top View of Instrument Support Plate and Elliptical Flow Distributor Plate Associated with Corium Relocation (Case ii)

B. Corium-Jet Breakup and Quenching

Based on the experimental results of the corium/water tests carried out at ANL,[17] a phenomenological model has been developed to describe the thermal and hydrodynamic behavior of a high-temperature corium jet when it interacts with water in a film boiling regime. A brief description of this model is presented in Appendix C. The jet-breakup behavior, such as the mass of corium eroded, the dispersed particle size, etc., is evaluated based on the steam generated from the vaporization of water at the vapor/water interface. The heat transfer aspects of the corium/water interaction, such as the heat transfer coefficient, vapor film thickness, vapor velocity in the vapor film, etc., are solved analytically from the mass, momentum, and energy equations governing the corium/vapor/water interactions. The jet-breakup and quenching behavior predicted by the model has been justified by comparing the measured and calculated system pressurization data due to steam generation, and good agreement has been confirmed for the tests carried out at ANL.

The predicted behavior of the corium jet breakup and quenching of the TMI-2 core relocation is presented below for various assumed relocation paths and initial conditions, such as the jet injection time, water subcooling, etc. The comparison is made between the measured and predicted primary system pressurization data at the time from ~224 minutes to ~226 minutes into the accident. The effect of the jet injection time (and jet initial velocity) is shown in Figures 3.8 and 3.9. Figure 3.8 shows the primary system pressure for a 6-inch (0.1524-meter) diameter jet interacting with the vessel water of 60 Kelvins (108 Farenheit degrees) subcooling without the additional breakup due to the CSA (i.e., Case i). The predicted pressure shows roughly a linear increase during the time of jet injection. Similar calculations were repeated for the water of 90 Kelvins (162 Farenheit degrees) subcooling as shown in Figure 3.9. Both Figures 3.8 and 3.9 show that the case with injection time of 90 seconds may well predict the trend of the measured pressurizations data. This also implies that the core relocation can be reflected by the sharp change of the SRM data. Therefore, the injection time of 90 seconds will be used exclusively in the following analysis.

Figures 3.8 and 3.9 also show that the system pressure decreases when the water subcooling increases. The water subcooling has two major effects on the

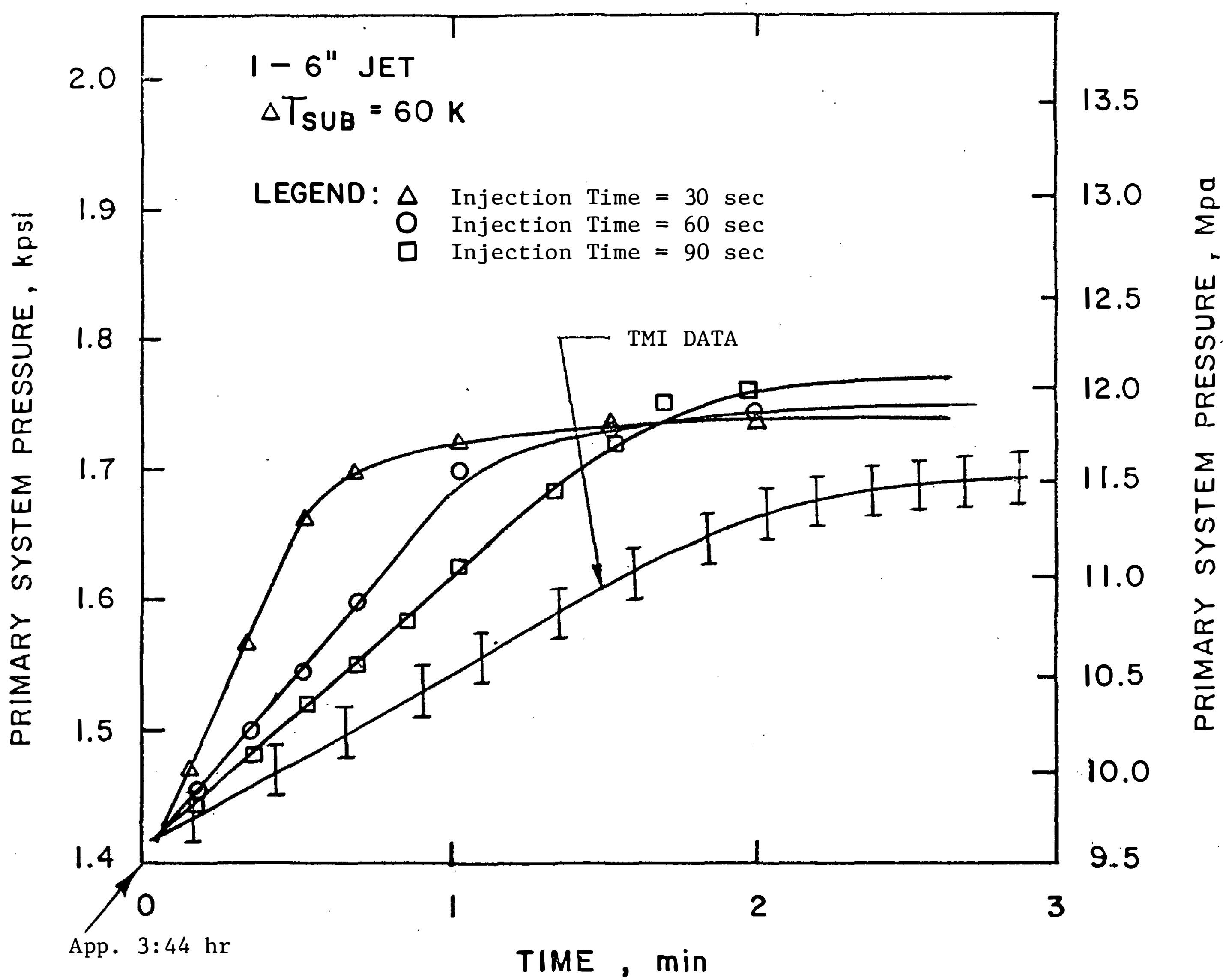

Figure 3.8 Primary System Pressure for a 6-inch Diameter Jet Without Pre-Fragmentation of CSA (Case i) for Different Injection Times

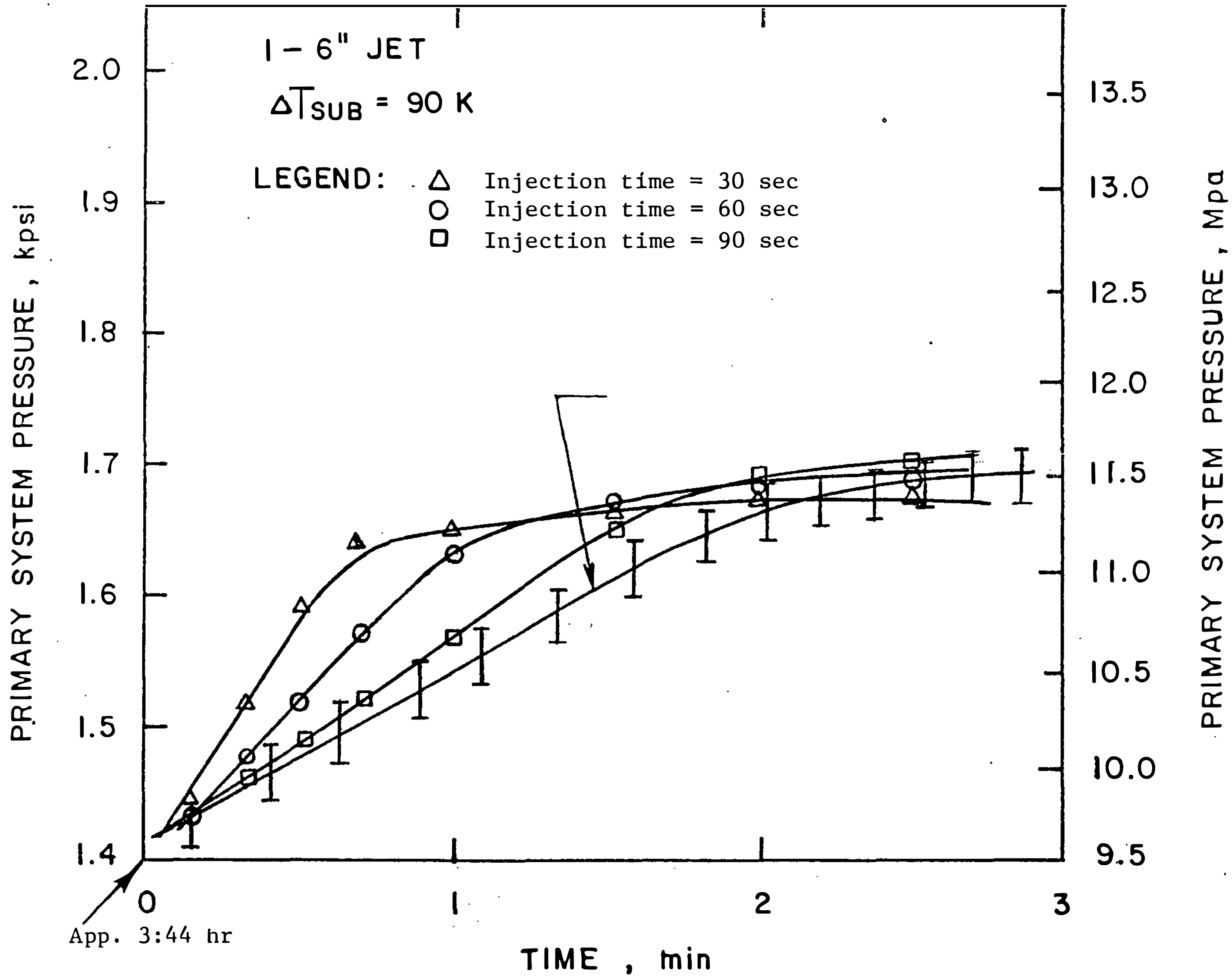

Figure 3.9 Primary System Pressure for a 6-inch Diameter Jet Without Pre-Fragmentation of CSA (Case i) for Different Injection Times

system pressure: i) it reduces the steam generation due to condensation, and ii) it reduces the jet erosion (i.e., increases the jet-breakup length) due to the reduced steam velocity. Both the reduction of the steam generation and the jet erosion will decrease the system pressure. A higher water subcooling will also increase the corium mass as a coherent jet when it is impinging upon the vessel wall due to the reduction of erosion. Thus, an assumption of a higher water subcooling may yield a more conservative convection heat transfer coefficient of the impinging corium jet on the vessel wall. However, the corium jet may lose more energy during its travel through the water due to a higher heat transfer into the subcooled water. Consequently, the jet may have a lower temperature when it impinging upon the vessel wall and results in a milder vessel heatup in spite of its larger physical geometry.

As described in Section II, the possible water subcooling ranges from ~60 Kelvins (108 Farenheit degrees) to ~205 Kelvins (369 Farenheit degrees) depending on the HPI condensation rate and the mode of mixing of the HPI/vessel water in the lower head. Based on the TMI primary system pressure and pressurizer water level data between 200 minutes to 217 minutes, the authors believe that the HPI condensation was mostly offset after 207 minutes. Therefore, the water subcooling may be bounded by ~90 Kelvins (162 Farenheit degrees) and ~205 Kelvins (369 Farenheit degrees) (see Section II). A microscopic investigation of the condensations between water and steam/hydrogen mixture shows that a water subcooling ranging from 160 Kelvins (288 Farenheit degrees) to 200 Kelvins (360 Farenheit degrees) was possible in the TMI lower head after the HPI water injection.[16]

The comparison of measured and predicted system pressure for the corium relocated through various relocations paths is shown in Figures 3.10 and 3.11. Apparently, a 205 Kelvins (369 Farenheit degrees) water subcooling results in an underestimated system pressure while a 90 Kelvins (162 Farenheit degrees) water subcooling predicts an overestimated system pressure. As explained before, lower water subcooling may yield a more conservative vessel heatup due to the impingement of a jet with higher temperature. Thus, water subcooling of 90 Kelvins (162 Farenheit degrees) is favored over 205 Kelvins (369 Farenheit degrees). In fact, the "A" loop cold leg temperature, as shown in Figure 2.1, shows a ~120 Kelvins (216 Farenheit degrees) water subcooling immediately prior to the core relocation. It is conceivable that some of the

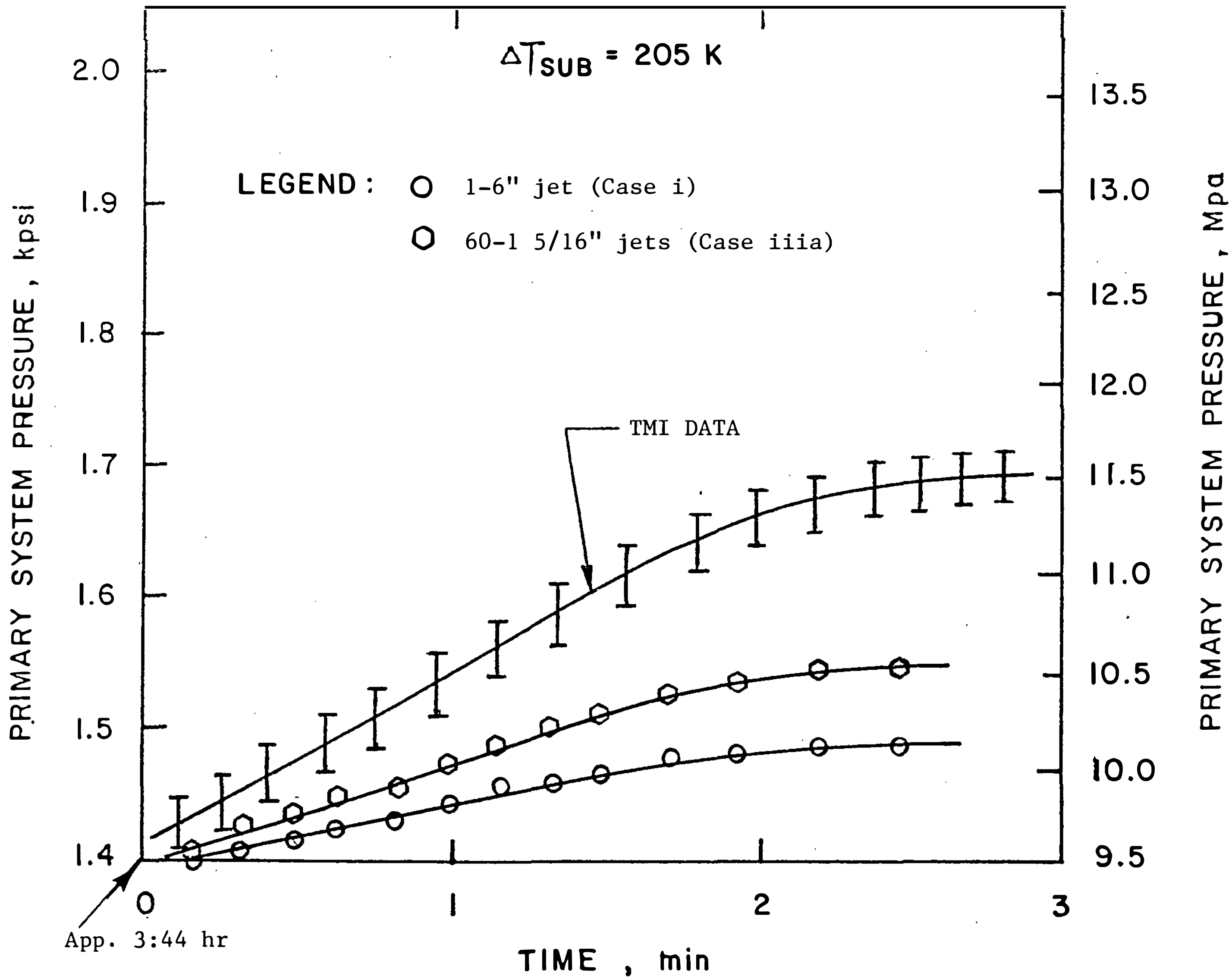

Figure 3.10 Primary System Pressure for a 6-inch Diameter Jet and 60 1 5/16-inch Jets Without Pre-Fragmentation of CSA (Case i and iiia) for 205K Water Subcooling

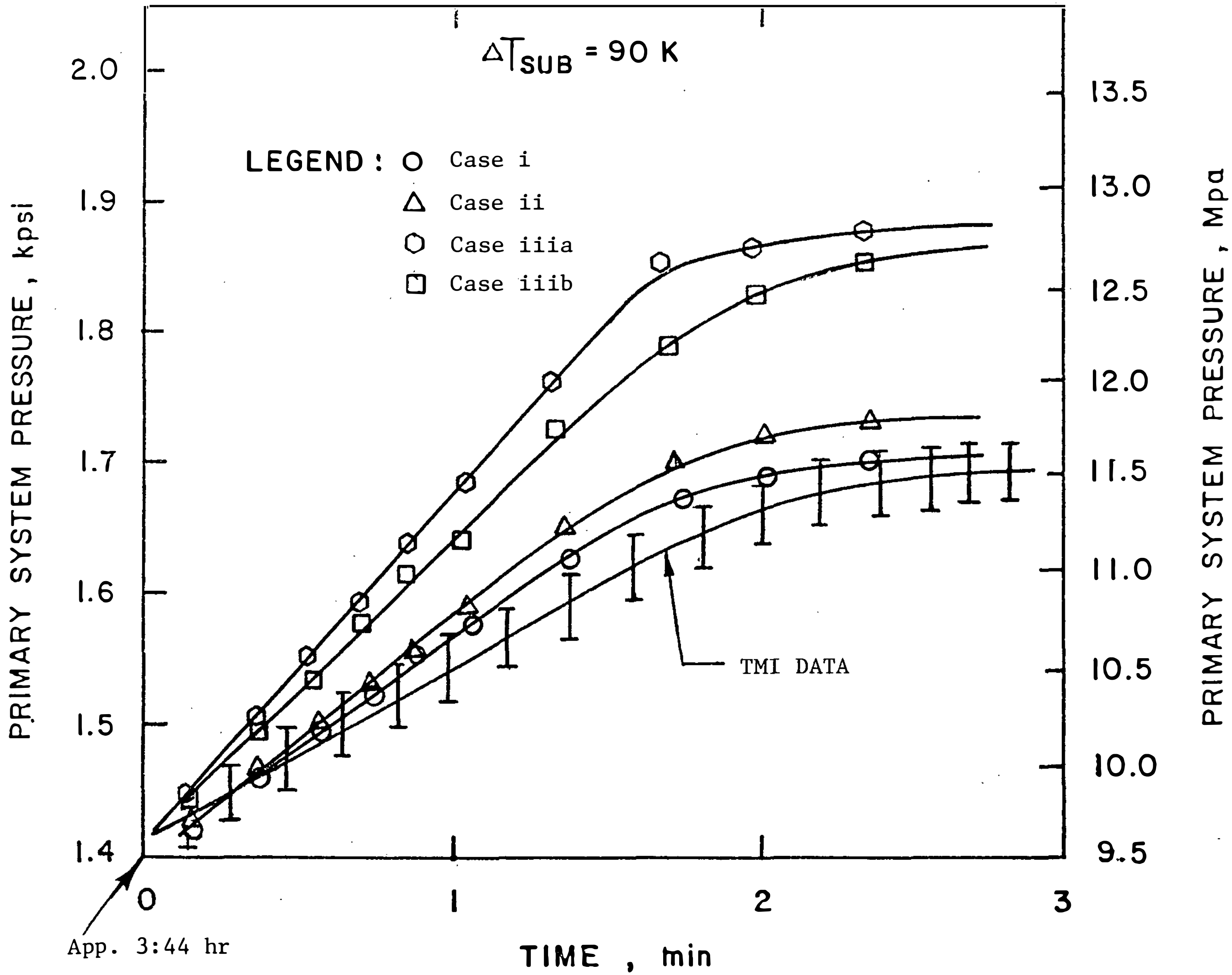

Figure 3.11 Primary System Pressure (Case i, ii, iiia, and iiib) for 90 K Water Subcooling

vessel water entered the "A" loop cold leg during and possibly before the core relocation due to the "carry-over" of the steam generated in the lower head. Therefore, a water subcooling between ~90 Kelvins (162 Farenheit degrees) to ~120 Kelvins (216 Farenheit degrees) is very possible before the core relocation. In fact, if we neglect the steaming from the core as expressed in Equation 2.3, a water subcooling of ~110 Kelvins (198 Farenheit degrees) will be obtained instead of 90 Kelvins (162 Farenheit degrees). Therefore, a water subcooling of 90 Kelvins (162 Farenheit degrees) can be considered as a lower bound, yet it yields a conservative vessel heatup.

Figures 3.10 and 3.11 also show that the predicted system pressure is bounded by case i and case iiia (i.e., one 6-inch (0.1524-meter) diameter jet and sixty 1 5/16-inch (0.033-meter) diameter jets, respectively). Case i predicts the lowest system pressure and an unrealistic, overly-conservative thermal attack on the lower head while Case iiia predicts the highest system pressure and a negligible thermal impact on the lower head. This can be clarified by comparing the thermal and hydrodynamic behavior of the corium jet (or jets) as shown in Figures 3.12 to 3.19. Figures 3.12 to 3.15 show the mass of a coherent jet (or jets), the formation of solidified particles and molten droplets as a function of the jet traveling distance. As predicted by the jet breakup model, the multiple 1 5/16-inch (0.033-meter) diameter jets will breakup completely into quenched particles before they reach the vessel wall. Both Case i and Case ii predict roughly one-third of the total corium mass impacts on the vessel wall as a coherent jet (or jets). Therefore, the vessel wall heatup are further evaluated for Case i and Case ii and the results are presented in the next subsection. Figures 3.16 to 3.19 show that the corium temperatures at the location of various core lower structures are still high. Thus, the ablation of the CSA due to the corium relocation may be possible.

The size of dispersed particles predicted by the jet breakup model ranges from ~1 millimeter (0.0394 inch) to ~10 millimeters (0.394 inch) with more than 50% of the total dispersed particles less than ~2 millimeters (0.0787 inch).

The breakup and quench of the control rod material relocated to the lower head is presented in Appendix E. The result shows that the control rod material forms a quenched debris bed on the center part of the lower head and the bed is located outside of the corium jet impingement zone.

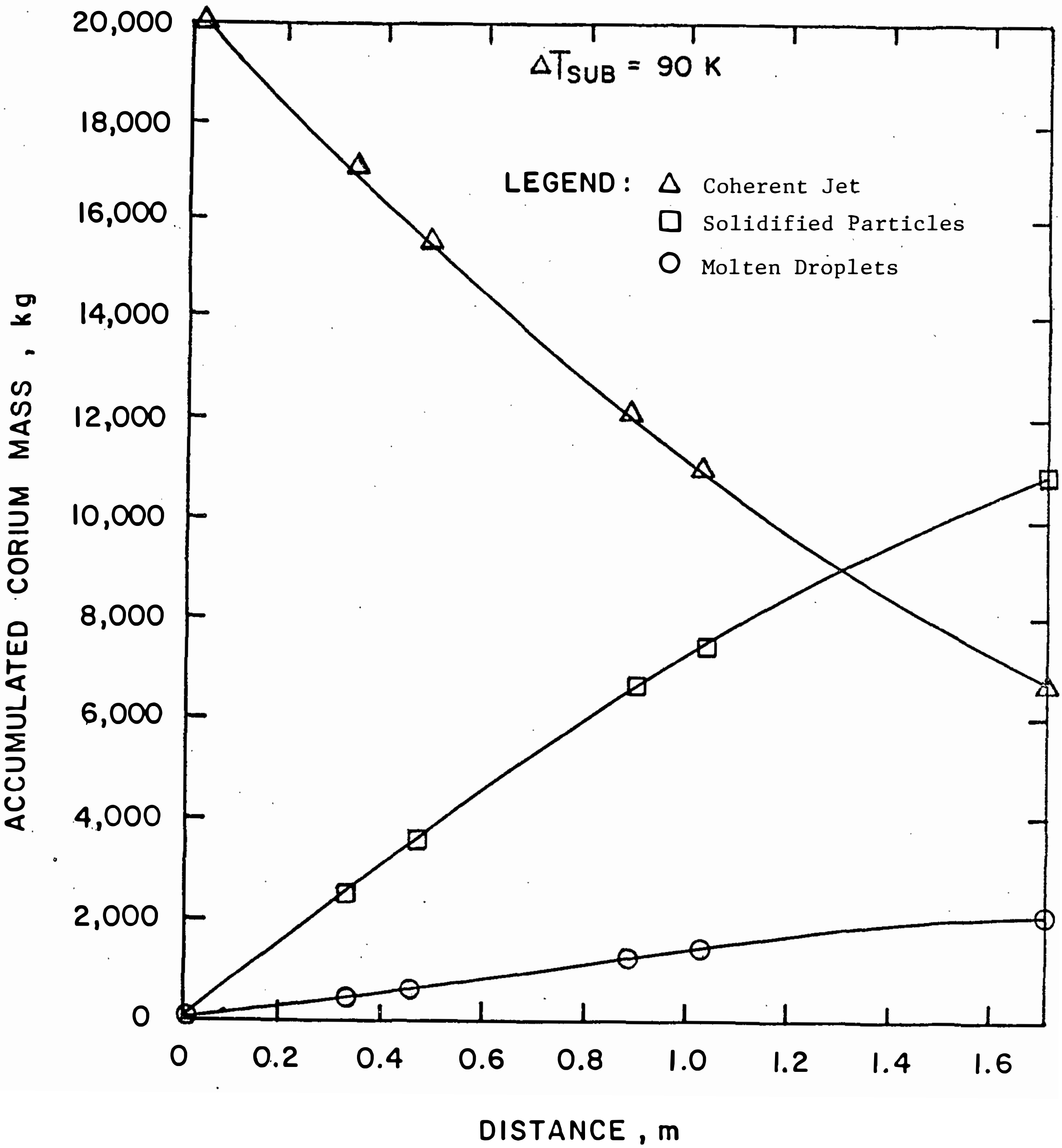

Figure 3.12 Corium Jet Breakup and Particle/Droplet Formation for Case i

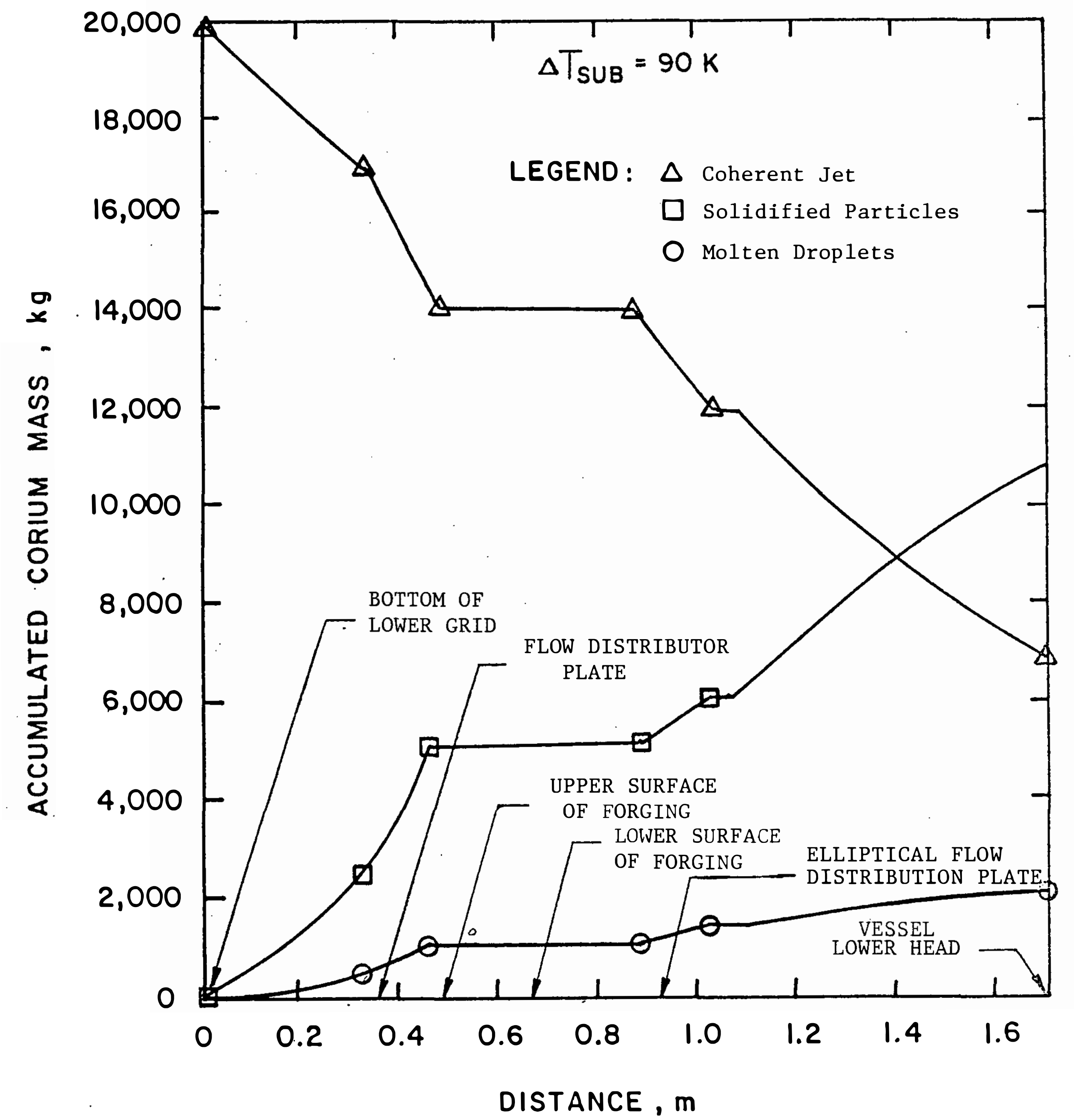

Figure 3.13 Corium Jet Breakup and Particle/Droplet Formation for Case ii

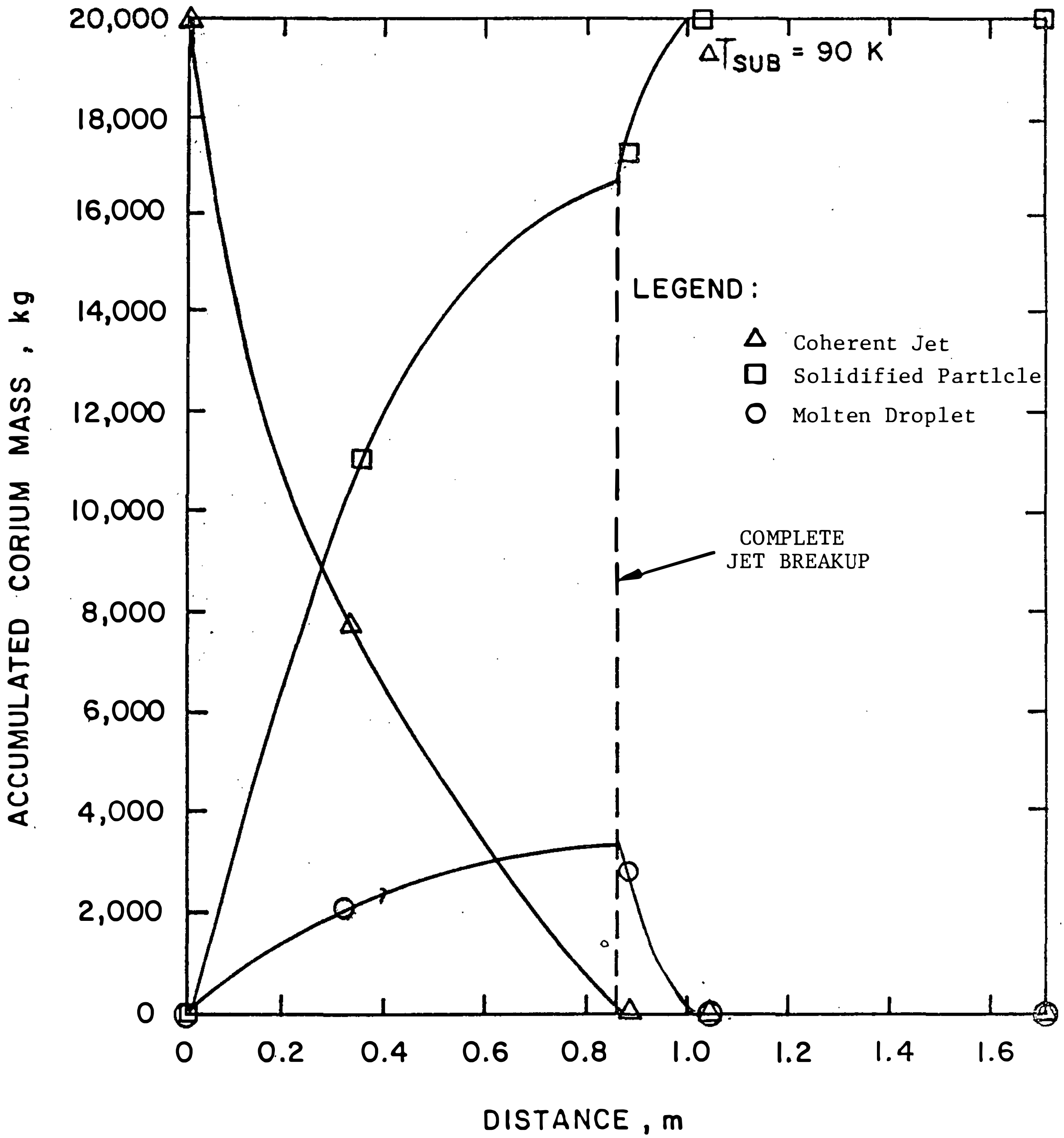

Figure 3.14 Corium Jet Breakup and Particle/Droplet Formation for Case iiia

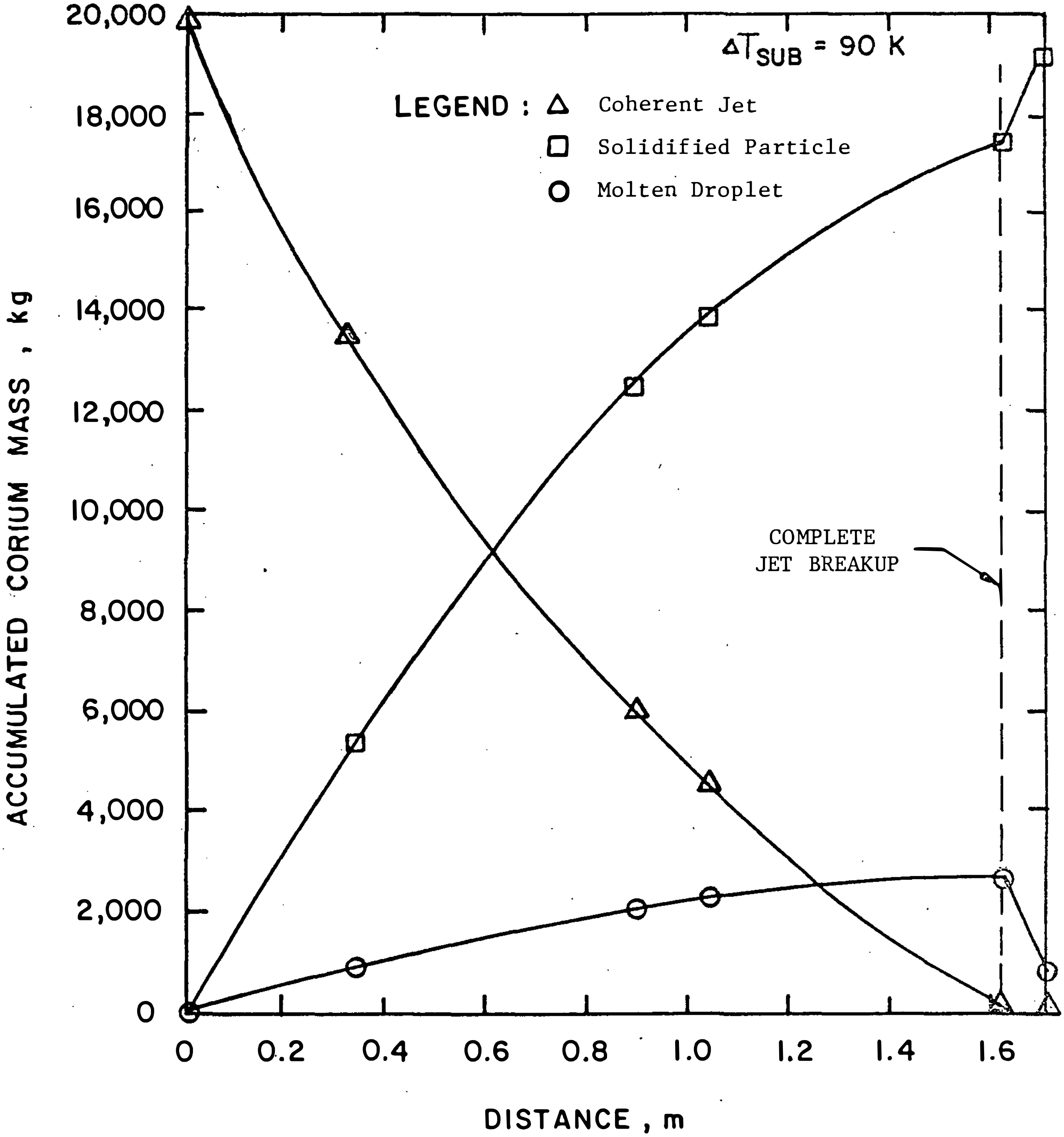

Figure 3.15 Corium Jet Breakup and Particle/Droplet Formation for Case iv

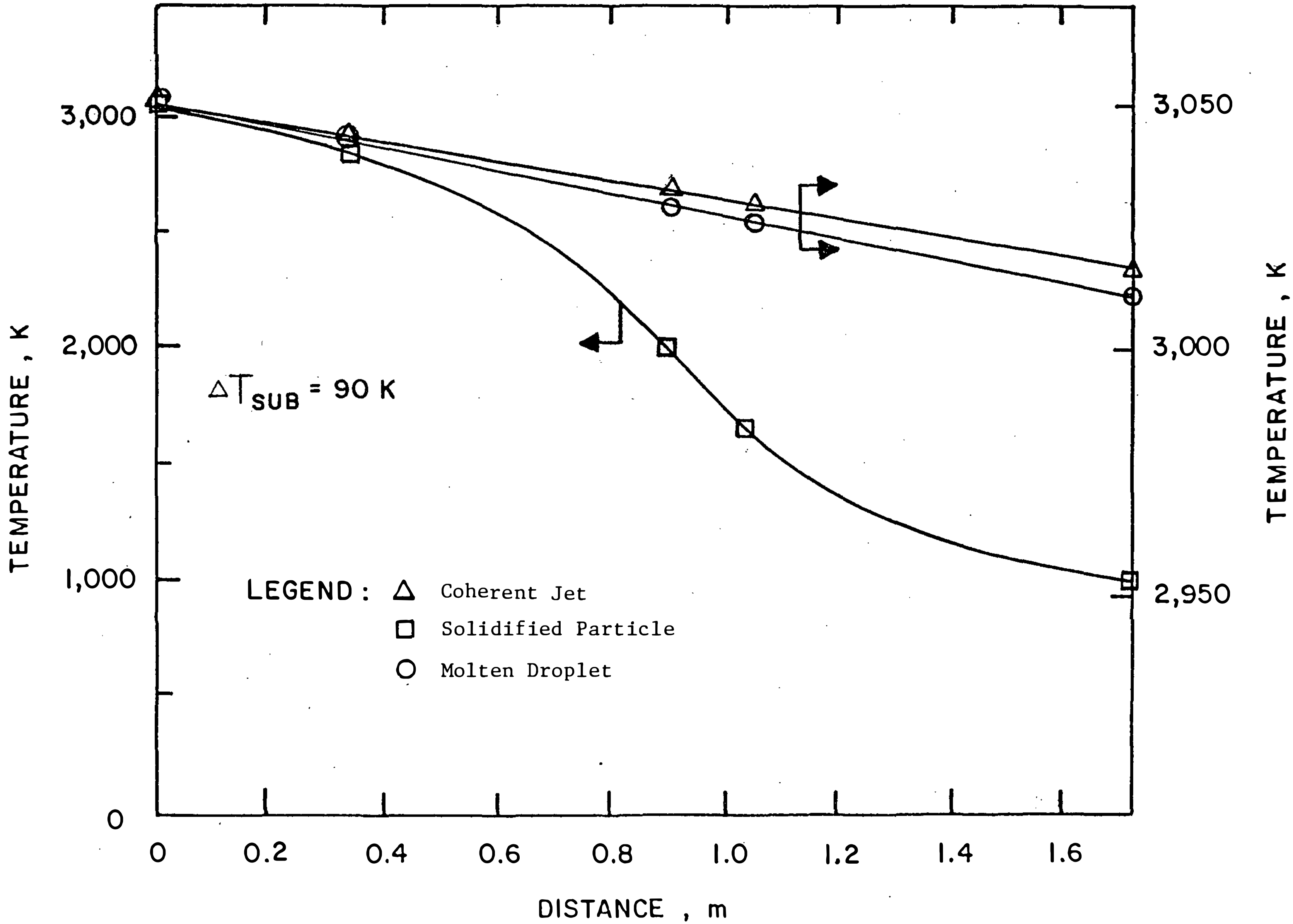

Figure 3.16 Corium Temperature Variation for Case i

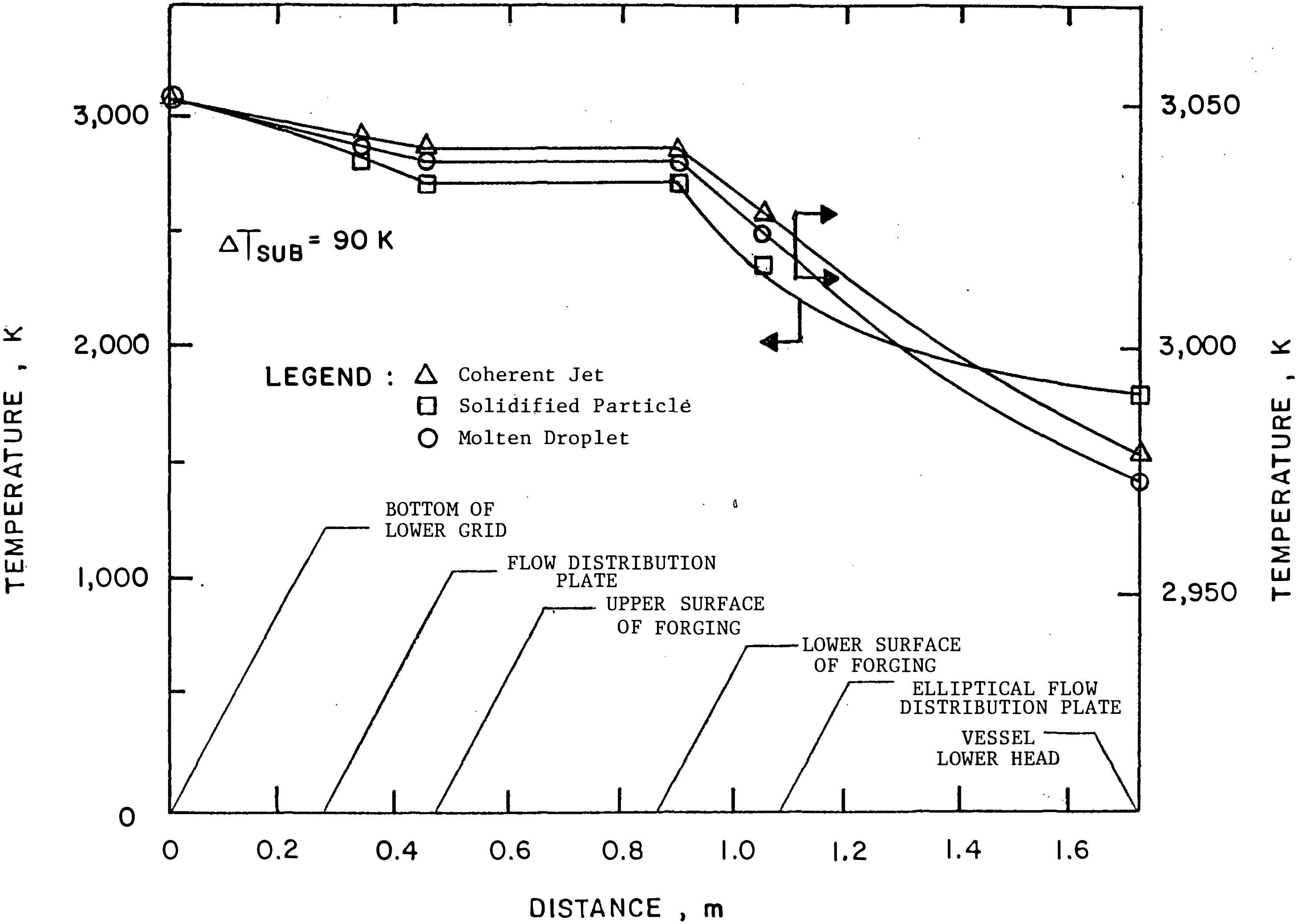

Figure 3.17 Corium Temperature Variation for Case ii

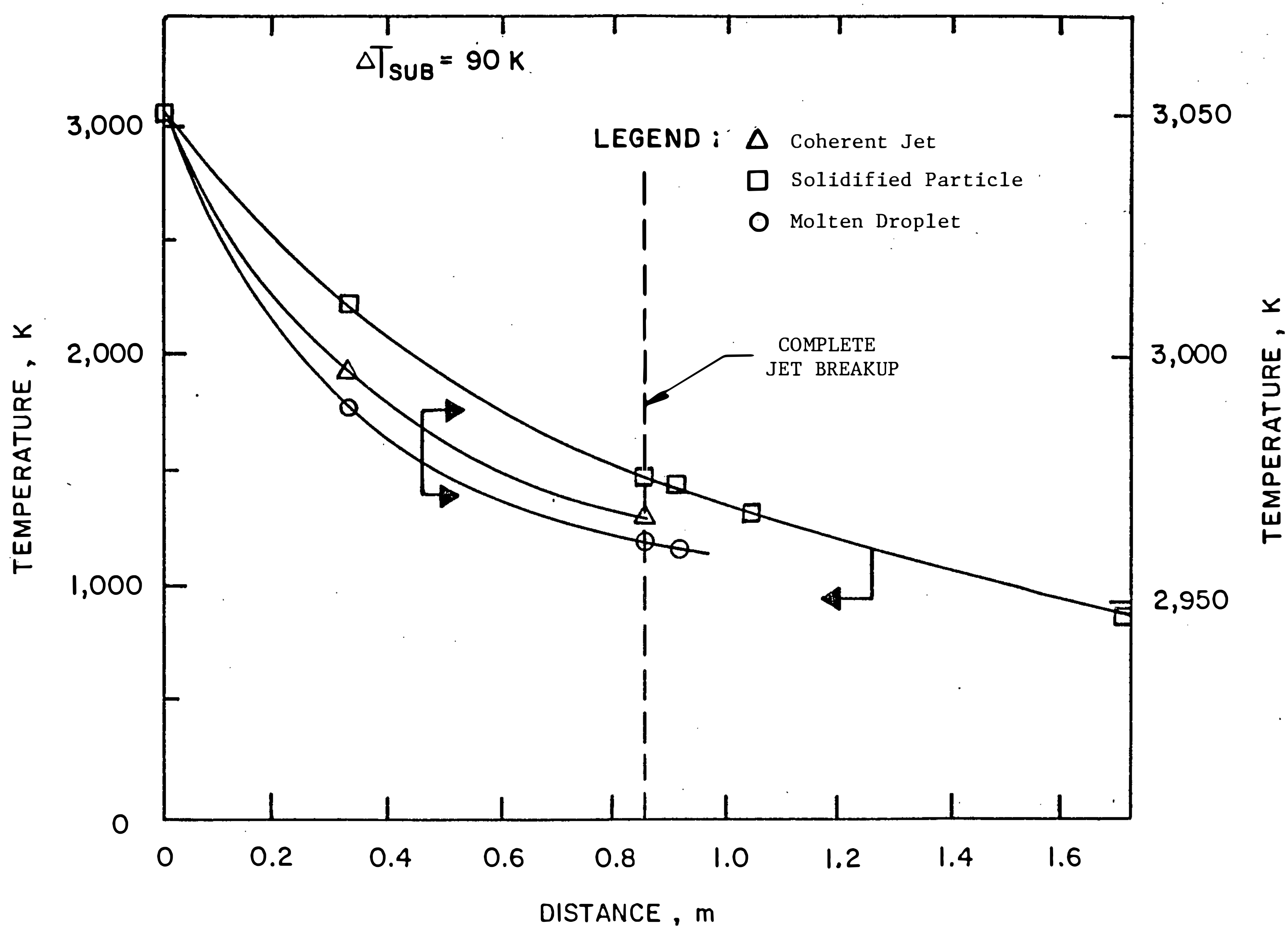

Figure 3.18 Corium Temperature Variation for Case iiia

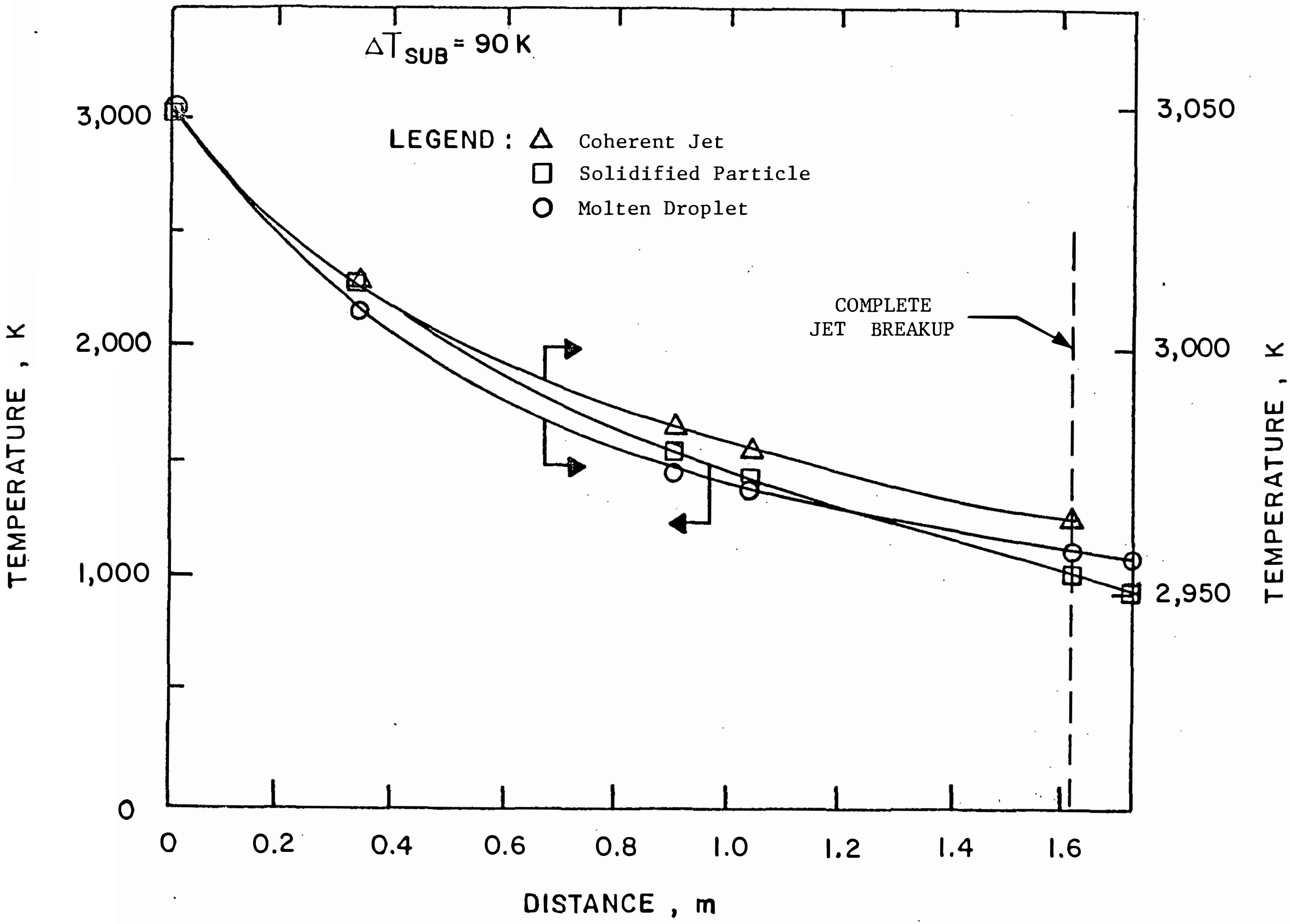

Figure 3.19 Corium Temperature Variation for Case iiib

C. Heatup of the Lower Head

The impingement of a corium jet upon the lower head may be calculated to result in high heat transfer rates into the steel inside the impingement zone in which the corium impacts upon the steel surface and either splashes off of the surface or is redirected to flow horizontally over the surface. The current analysis thus considers the heat transfer phenomena in the impingement region which is expected to represent the greatest potential for thermal attack upon the lower head and failure of the weldment securing one of the instrument penetrations to the vessel wall inner surface. In particular, the temperatures inside the lower head thickness beneath the impingement zone are expected to exceed those in the surrounding regions. Accordingly, the current calculations predict the temperatures across the thickness of the lower head directly beneath the impinging corium and, in the event that melting occurs, the maximum thickness of material which is ablated away. The transient temperatures within the lower head and the ablation rate are calculated using the one-dimensional MISTI computer code previously developed at Argonne National Laboratory. MISTI was originally used for analysis of the Corium Structure Thermal Interaction (CSTI) and Corium Water Thermal Interaction (CWTI) experiments[33] in which predominantly oxide corium mixtures were impinged upon stainless steel plates to provide data on the fundamental mechanisms involved in corium-structure, impingement mode heat transfer. The modeling assumptions and equations currently incorporated in the code are documented in Appendix F. Thermophysical properties employed in the calculations for corium and the lower head are discussed in Appendices A and B, respectively.

1. Case i (Scoping Calculation)

For the scoping calculation in which a single unimpeded jet is assumed to drain through the lower plenum and the effects of the CSA are unrealistically ignored, the corium jet impinging upon the lower head has a diameter of 8.72 centimeters (3.43 inches), velocity of 1.43 meters per second (4.69 feet per second), and temperature of 3017 Kelvins (4971 degrees Farenheit). The corium temperature represents a molten "superheat" of 167 Kelvins (301 Farenheit degrees) above the corium freezing temperature of 2850 Kelvins (4670 degrees Farenheit). This is the driving temperature difference for heat transfer from the impinging corium stream. For the impinging jet conditions, the forced convection heat transfer coefficient has a value of 16.0 kilowatts per square meter per Kelvin (2820 Btu per square foot per hour per Farenheit degree). This provides a heat flux, Q, of 2670 kilowatts per square meter (847000 Btu per square foot per hour).

In response to the impingement heat flux, the temperature of the steel at the corium crust-lower head wall interface is calculated to rise to the steel melting temperature of 1810 Kelvins (2800 degrees Farenheit) over an interval of 37 seconds. This is about one-third of the 90 second duration over which the corium jet is assumed to impinge upon the lower head. The temperature at the corium-steel interface during the pre-melting heatup phase is shown in Figure 3.20. The temperature profile within the lower head wall at the onset of melting is presented in Figure 3.21. At this time, the thermal wave has penetrated approximately 7 centimeters (2.8 inches) into the steel. Figure 3.20 also shows the thickness of the interstitial corium crust. The crust thickness rapidly grows to a maximum value of 1.43 millimeters (0.0563 inch) and then gradually decreases to 0.94 millimeters (0.037 inch) as the interface temperature progressively rises to the melting temperature. Thereafter, the crust has a constant thickness as steel ablation is assumed to proceed in a quasi-steady manner. Accordingly, the vessel wall is eroded at a constant rate of 0.331 millimeter per second (0.0130 inch per second) following melting inception. The lower head thickness eroded as a function of time is shown in Figure 3.22. Over the remainder of the jet impingement interval following the onset of melting, a total erosion of 1.77 centimeters (0.697 inch) is calculated. This would be a sufficient thickness to threaten the integrity of a penetration weldment.

2. Case ii (Bounding Severe Calculation)

For the bounding severe case in which a single jet is assumed to drain from the CFR but the effects of the underlying CSA in breaking up the jet are modeled, the corium is envisioned to impinge upon the lower head as four jets draining from the elliptical flow distributor plate. Because the impinging molten corium is distributed among several jets, the lower head undergoes a heatup which is significantly less severe than that corresponding to the impingement of the corium as a single unimpeded stream. Specifically, the heat transfer effects resulting from the impact of four jets are distributed over a larger portion of the lower head surface and the maximum heat flux into

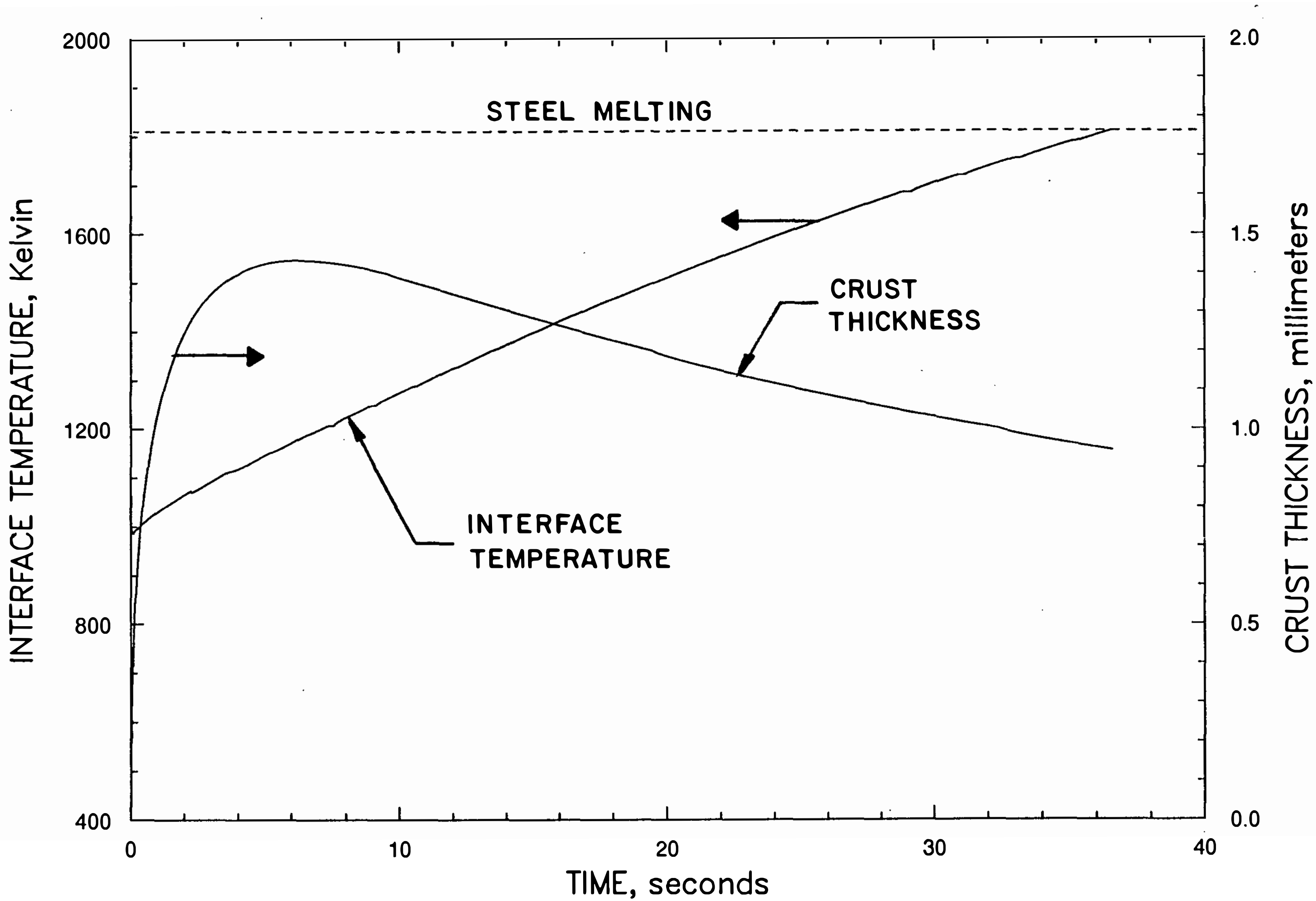

Fig. 3.20 Temperature at Interface Between Corium Crust and Vessel Lower Head Steel Following Onset of Corium Jet Impingement and Thickness of Corium Crust Formed Upon Lower Head Resulting from the Impingement of a Single Unimpeded Jet.

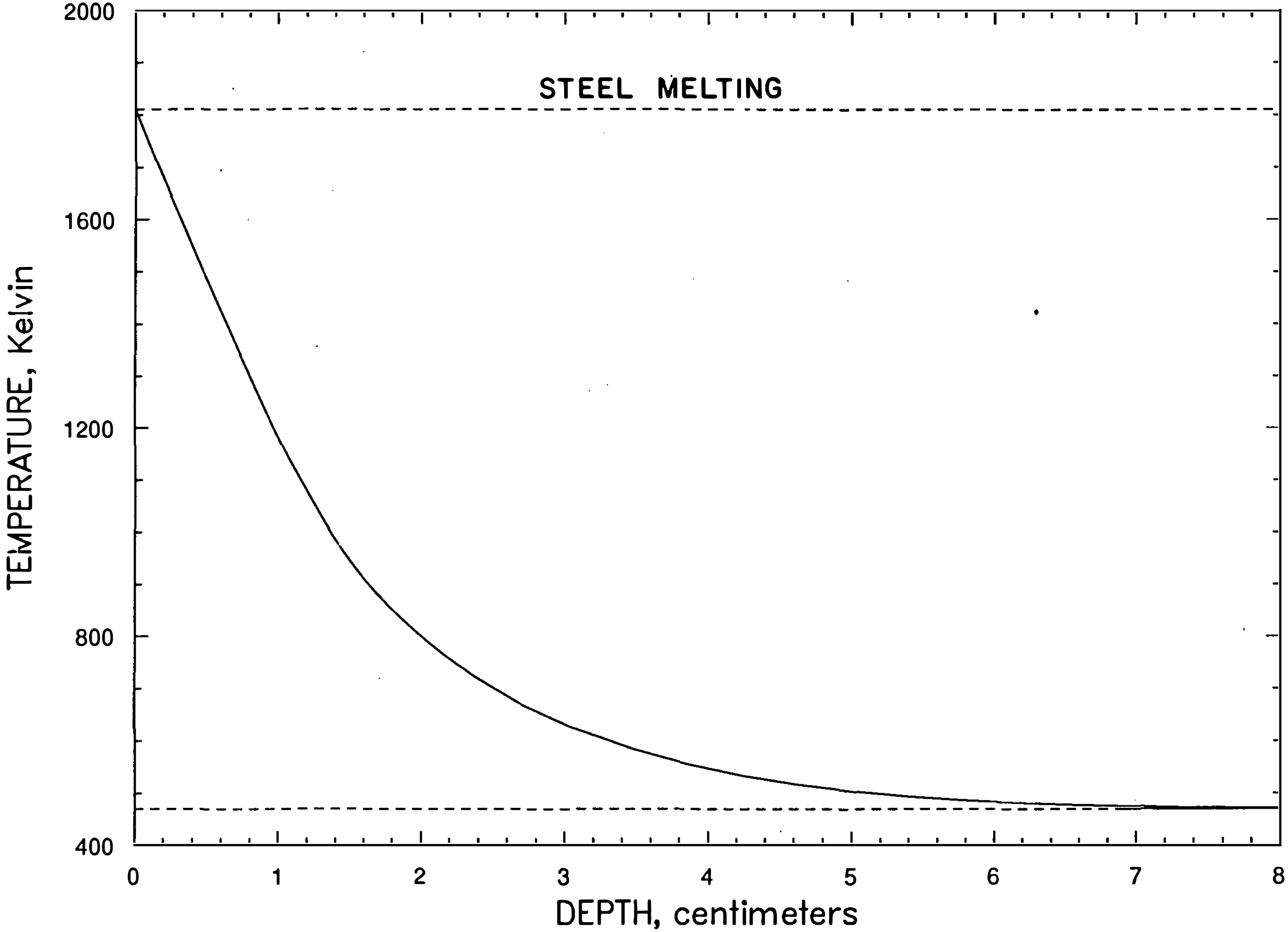

Fig. 3.21 Temperature Profile Within Vessel Lower Head at the Inception of Steel Melting Resulting from the Impingement of a Single Unimpeded Jet.

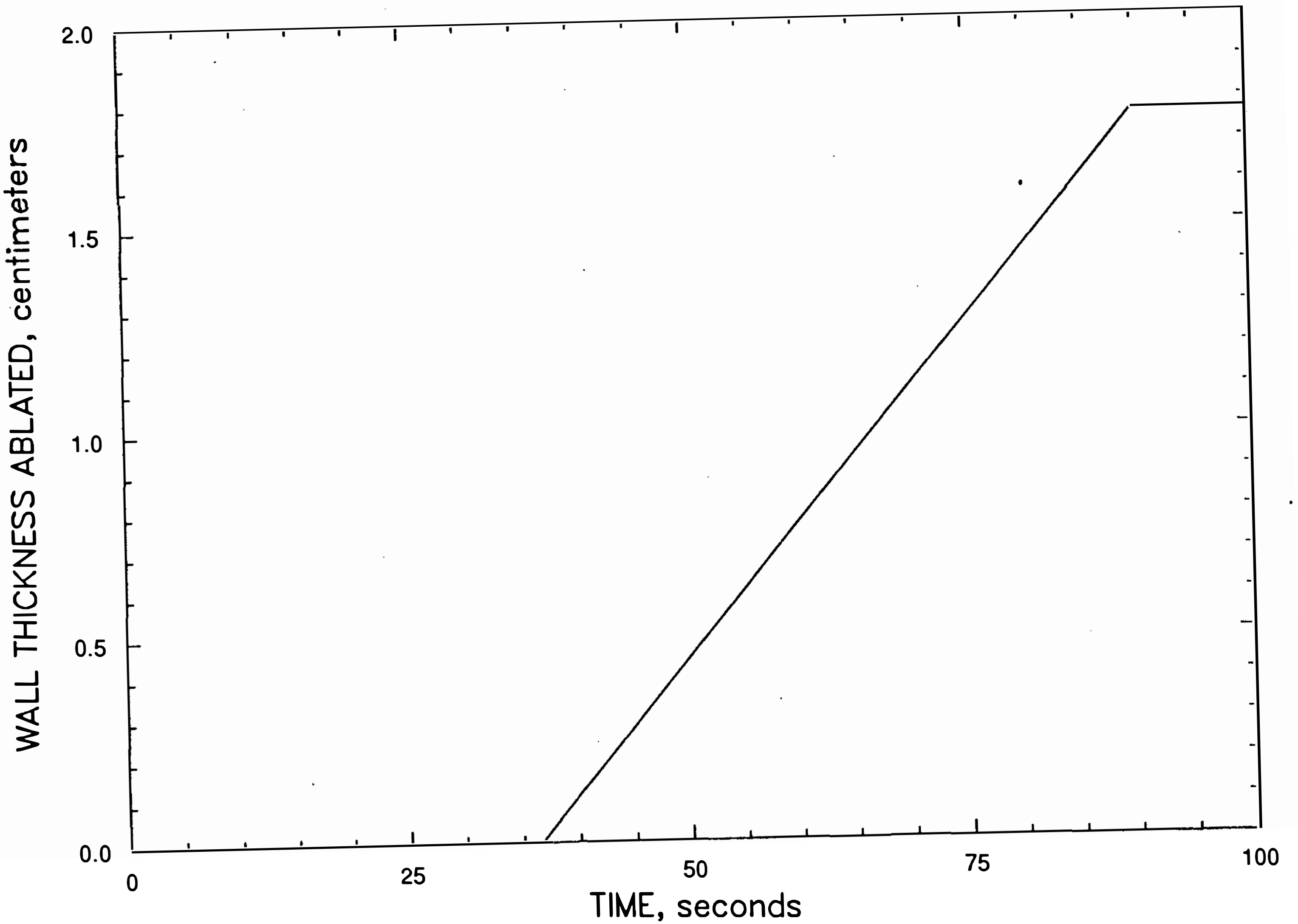

Fig. 3.22 Thickness of Lower Head Wall Ablated Following Onset of Corium Jet Impingement of a Single Unimpeded Jet.

the vessel wall is significantly less than that thus attained with a single unimpeded and localized stream. Similar to the unrealistic scoping calculation, roughly one-third of the corium mass reaches the lower head in the form of the four jets with the remainder having undergone breakup into particles and droplets. It follows that the impingement velocity of each of the four jets is expected to be less than one-fourth that obtained in the single jet case. In fact, each of the four jets is calculated to impinge with a velocity of 0.251 meter per second (0.823 foot per second) versus 1.43 meters per second (4.69 feet per second) for the single jet considered previously. The diameter of each impacting stream is 10.7 centimeters (4.21 inches) relative to 8.12 centimeters (3.20 inches) for the unimpeded stream case. In addition, the corium impinges with a somewhat lower temperature of 2983 Kelvins (4910 degrees Farenheit) corresponding to a molten superheat of 133 Kelvins (239 Farenheit degrees) compared with 167 Kelvins (301 Farenheit degrees) of superheat obtained previously. All of these conditions reduce the heat flux inside the impingement zone of each jet. Specifically, the forced convection heat transfer coefficient has a value of 5.60 kilowatts per square meter per Kelvin (987 Btu per square foot per hour per Farenheit degree) and the impingement zone heat flux is equal to 744 kilowatts per square meter (236000 Btu per square foot per hour) versus 16.0 kilowatts per square meter per Kelvin (2820 Btu per square foot per hour per Farenheit degree) and 2670 kilowatts per square meter (847000 Btu per square foot per hour) for the unrealistic single jet case.

The temperature at the corium crust-lower head wall interface is shown in Figure 3.23. The temperature is predicted to rise to a maximum value of 1210 Kelvins (1718 degrees Farenheit) at the end of the 90 second long interval over which jet impingement is assumed to take place. The peak temperature remains 600 Kelvins (1080 Farenheit degrees) below the lower head melting temperature of 1811 Kelvins (2800 degrees Farenheit). Thus, ablation of the lower head is calculated not to occur. The temperature profile through the thickness of the lower head at the end of the jet impingement phase is shown in Figure 3.24. For the indicated conditions, failure of the weldments securing the instrument penetration guide tubes to the lower head would not be expected.

The current analysis predicts the heatup of the lower head and penetra-

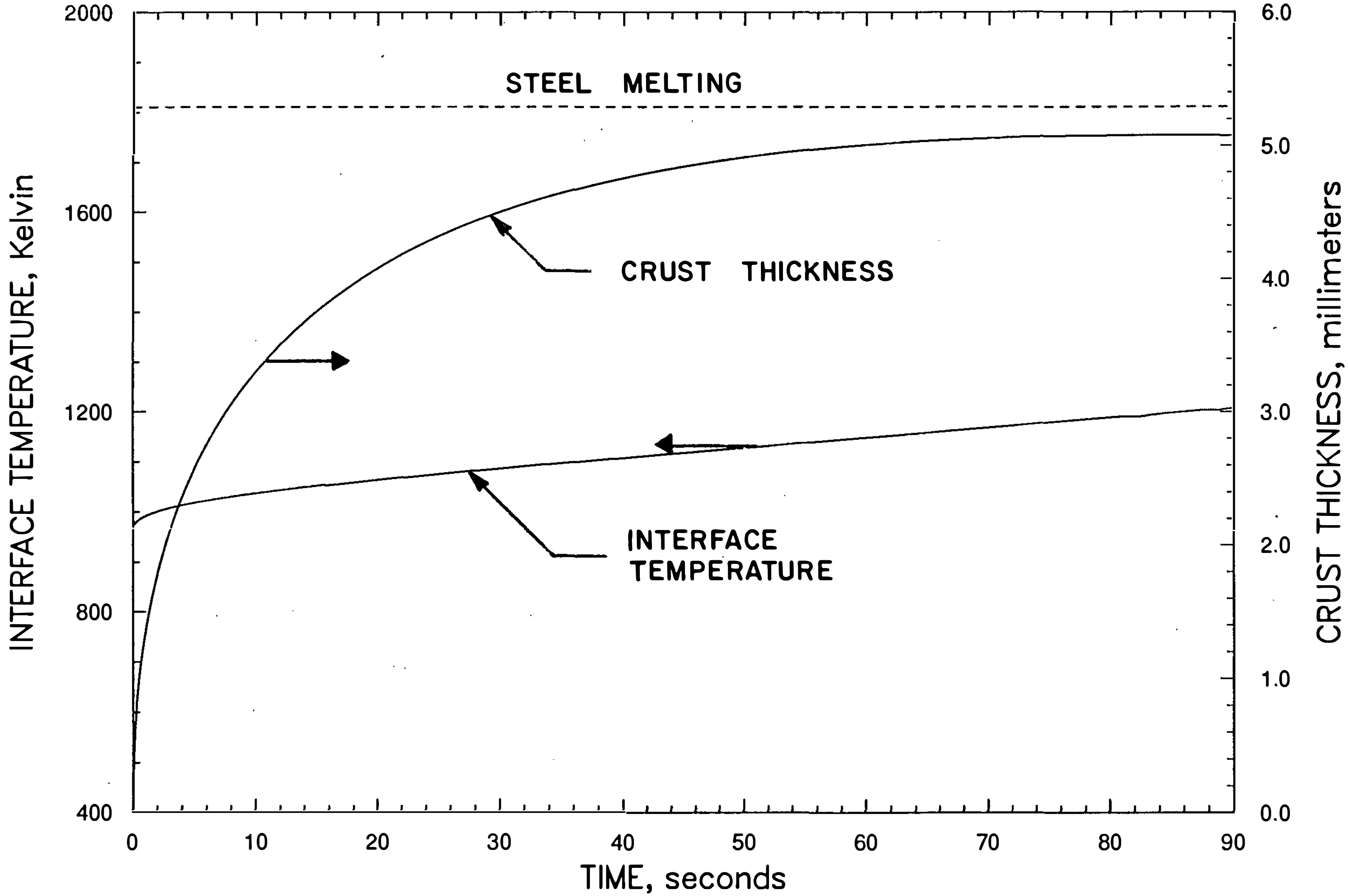

Fig. 3.23. Temperature at Interface Between Corium Crust and Vessel Lower Head Steel Following Onset of Corium Jet Impingement and Thickness of Corium Crust Formed Upon Lower Head Resulting from the Impingement of Four Corium Jets Draining from the Core Support Assembly.

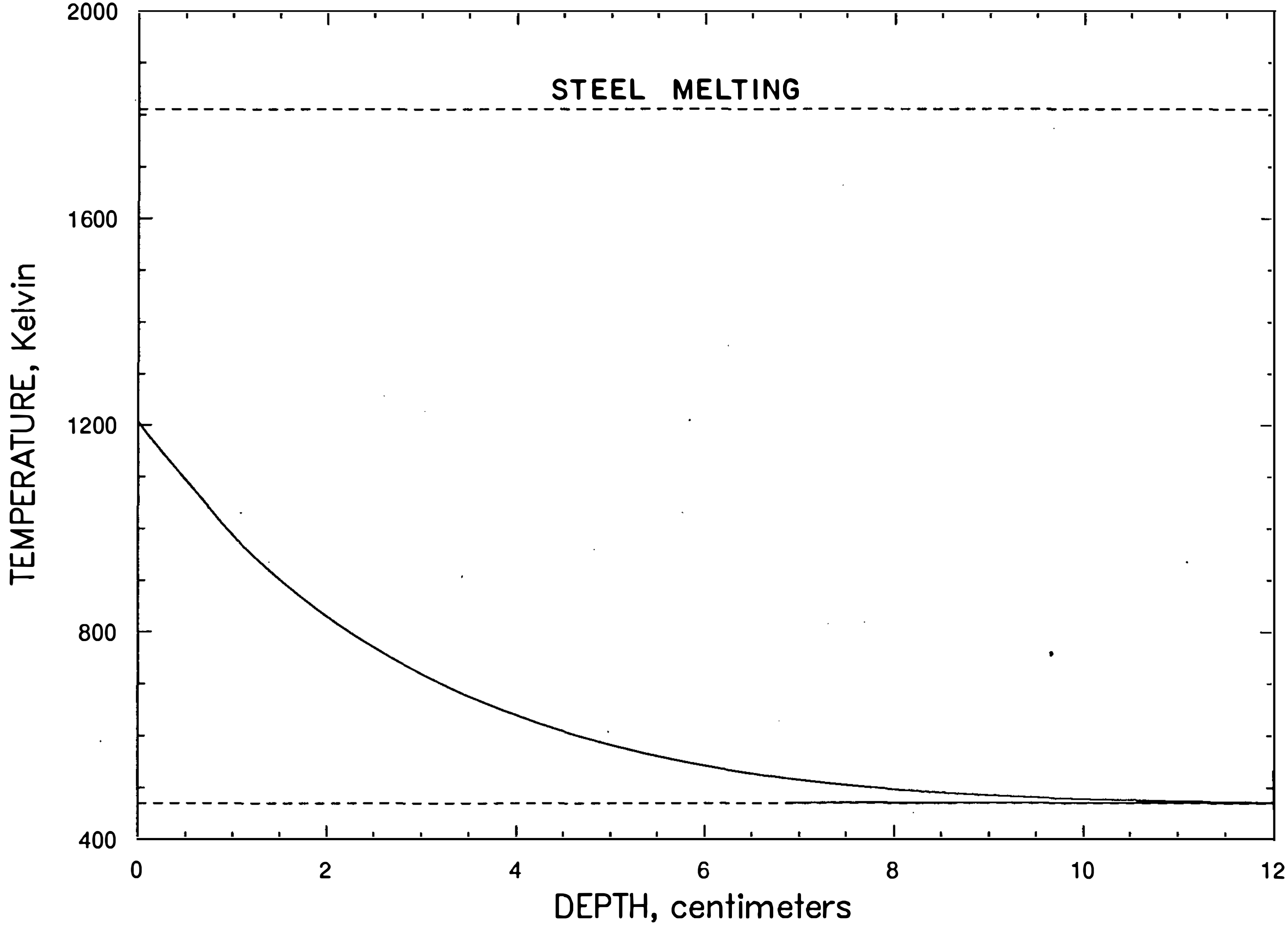

Fig. 3.24 Temperature Profile through the Thickness of Lower Head at the End of the Jet Impingement Phase.

tion weldments only for the impingement of a downward directed corium jet. Following impingement, the corium might spread over the inner surface of the lower head to impinge upon the sides of the neighboring instrument penetration nozzles. An uncertainty here is whether the corium would in fact spread over the lower head instead of splashing up off of the surface to resume its interaction with water. Predictions of the transient heatup and potential ablation of the instrument nozzles or the underlying weldments resulting from this spreading mode of contact were not carried out as part of the current analysis. Such calculations would require additional analysis beyond the scope of the present investigations.

IV. SUMMARY AND CONCLUSIONS

In summary, the following conclusions and observations may be drawn from the current analysis:

1) The best estimate case assumes that the corium relocated through the core former region such that corium drained as a large number of jets from the lowermost core former plate. Specifically, the corium is assumed to drain through as many as sixty 3.33 centimeters (1.31 inch) diameter flow holes. This corresponds to three-fourths of the circumference of the core former region, consistent with the material dispositions observed in the defueling examinations. Due to interactions with water, the corium jets are calculated to undergo complete breakup into molten droplets which freeze as they settle through the water in the reactor vessel lower plenum. The predicted particle diameters range from 1 to 10 millimeters (0.039 to 0.39 inch) in size. Based upon the results and analysis of the Argonne Core Coolant Mixing (CCM) experiments, the debris inside the lower head is predicted to consist of a loose or weakly sintered assemblage of particulate.

2) The bounding severe case assumes that the corium enters the lower plenum as a single, coherent, 15 centimeter (6 inch) diameter jet which drains from the core former region and interacts with the underlying core support assembly structure. The core support assembly causes the original single jet to be broken into multiple jets. For an assumed minimum of four smaller jets impinging upon the lower head, the absence of a melting attack upon the lower head is predicted. In particular, the temperature at the vessel wall inner surface is calculated to attain a maximum value of 1200 Kelvins (1700 degrees Farenheit) remaining 600 Kelvins (1100 Farenheit degrees) below the material melting temperature. Approximately two-thirds of the corium is broken up into droplets ranging in diameter from 1 to 10 millimeters (0.039 to 0.39 inch) with the remaining third predicted to impinge upon the lower head as the assumed four jets. Based upon the results and analysis of the Core Coolant Mix-

ing tests, the debris inside the lower head would be predicted to consist of an aggregate mixture of particles and solidified melt.

3) Corium entering the core former region through a localized breach in the baffle plate structure is calculated to spread around most of the circumference of the core former region while draining through the flow holes in the former plates. The maximum extent of spreading corresponds to about 80 percent of the core former region circumference in good agreement with the defueling examinations.

4) Relocation through the core former region has a significant effect in promoting the breakup of corium in water by causing the corium to simultaneously drain from a large number of flow holes as relatively small diameter jets.

5) The core support assembly structure has an important effect in protecting the lower head by causing the corium to splash off of the various plates and by breaking up single corium jets into multiple jets. It is impossible for corium to drain through the core support assembly as a single coherent jet.

6) Long-term coolability of the debris bed formed in the best estimate case was not examined through the application of models predicting the conditions under which bed dryout occurs. It is expected that for the particle sizes calculated to result from the breakup of the corium streams, the bed will be coolable such that no significant heatup of the lower head would subsequently occur.

7) As corium drains through the core former region, it is calculated to heat up and ablate the steel surrounding individual flow holes thereby enlarging the size of the holes. Prior to the onset of ablation, the corium is calculated to still spread over about 80% of the core former region circumference. Subsequently, as the flow holes grow in size, the corium is calculated to spread over a decreasing portion of the former region circumference. However, complete breakup of the corium draining as streams from the flow holes into particles is still calculated. For this case, a loose and weakly sintered particle bed is predicted to exist inside the lower head.

8) A scoping calculation was carried out to ascertain the effects of jet breakup in water alone without the additional breakup effects induced by the core support assembly structure or relocation through the core former region. The corium was assumed to enter the lower plenum as a single, coherent, 15 centimeter (6 inch) diameter jet. About two-thirds of the corium is calculated to be broken up into droplets. The remaining third is predicted to impinge upon the lower head as a single jet and give rise to ablation of 1.8 centimeter (0.71 inch) of the lower head wall thickness. This calculation bears no relation to reality due to the absence of the effects of the core support assembly and spreading flow inside the core former region.

9) The depth of water present between the core and the lower head is

not by itself sufficient to protect the lower head without consideration of the additional effects of the core support assembly structure.

10) The subcooling of the water in the lower head has a large effect upon the predicted rise in the primary system pressure resulting from interactions of corium with the water. The major effect here is condensation of steam within the bulk water mass. If the water were saturated, the predicted pressure rise would be significantly higher. Unfortunately, the uncertainties in the subcooling preclude the direct use of the pressure measured during the relocation event to select among the various mechanisms.

11) The subcooling of water inside the lower head immediately before the relocation event was calculated using the measured primary system pressure to determine the net steam condensation rate together with modeling of the relevant heat transfer processes. The subcooling was found to be strongly sensitive to uncertainties in the degree to which cooler water delivered by the high pressure injection remains stratified in the lower head versus mixing homogeneously with water present inside the reactor vessel.

12) Temperature measurements in the A-loop suggest a subcooling of 120 Kelvins (220 Farenheit degrees) prior to the relocation event. This value corresponds most closely to the results of calculations of the subcooling which assume thermal mixing of injected water with that already present in the reactor vessel, negligible quenching of the core region prior to relocation, and negligible condensation inside the cold leg piping after 207 minutes. For these assumptions, a subcooling of 110 Kelvins (200 Farenheit degrees) is predicted.

13) For the best estimate case, subcooling has a minor effect upon the prediction of complete corium breakup. In the severe bounding case, a lower subcooling would have resulted in the calculation of more extensive corium breakup and slightly higher melt temperatures for corium impinging upon the lower head.

14) The corium relocation rate was assumed to be uniform over an interval of 90 seconds. This timescale was obtained from the rise time in the count rate of the source range monitor, ex-core, neutron detector. The resulting timescale for the rise in the primary system pressure calculated due to corium-water interactions is in good agreement with the measured pressure data, barring uncertainties in the data reflecting acquisition sampling rates. The use of a shorter relocation time would result in the prediction of a more rapid pressurization than indicated by the data. Similarly, the assumption of a longer relocation interval would give rise to an underprediction of the pressurization rate.

15) The corium superheat (excess temperature above the corium freezing temperature) was assumed to have a value of 200 Kelvins (360 Farenheit degrees) based upon a previous analysis of the heatup of the molten core region before the relocation event. For the best estimate case, the superheat has a minimal effect upon the predic-

tion of complete breakup and particle formation. For the bounding severe case, the effects of superheat upon corium breakup are minor. However, the heatup of the lower head is sensitive to the superheat, because the convective heat flux in the impingement zone is proportional to the superheat. Additional calculations are required to determine the dependency of the predicted lower head heatup upon uncertainties in the superheat. In the absence of further calculations, it is anticipated that an increase in superheat by a factor of about two would be necessary to predict the beginning of a melting attack.

16) A corium mass of 20 metric tonnes (44000 pounds) was assumed to relocate into the lower head. If a lower mass were used, complete breakup would still be predicted in the best estimate case. For the bounding severe case, a lower mass would result in the calculation of more extensive breakup and an even less severe heatup of the lower head.

17) There is uncertainty in the role that control material which melted and relocated into the lower head may have played. Calculations were carried out examining the breakup and quenching of molten control material alloy. The calculations suggest that the control material underwent extensive breakup to form particles which were effectively quenched as they settled through the water. However, the radial extent of the resulting debris is not predicted to reach the peripheral regions of the vessel lower head where corium would drain from the overlying core former region.

18) The modeling of the interactions between corium and water did not account for the possible generation of hydrogen from oxidation of metallic constituents. This is justified in the current analysis because the principal form of the relocated mass was a UO_2-ZrO_2 mixture.

19) The heatup of the lower head was calculated on the basis of impingement of downward directed corium jets. Forced convection heat transfer inside the impingement zone is expected to represent the highest heat fluxes into the weldments. However, following impingement, the corium might be envisioned to flow laterally along the inner surface of the lower head to impinge upon the neighboring, upright incore instrument nozzles. The prediction of nozzle heatup from this contact mode lies beyond the scope of the current analysis. A major uncertainty here is the potential for a corium jet to splash up off of the lower head surface as opposed to spreading over the surface as a coherent layer.

20) The circumstances under which corium freezing and immobilization took place inside the core former region are uncertain. However, the presence of particulate debris observed between successive former plates suggests that water initially present inside the core former region had a significant effect in promoting corium breakup and quenching to form debris beds upon the former plates underlying the breach in the baffle plate structure.

21) Although a corium mass of the order of 20 tonnes (44000 pounds) relocated into water in the lower head, there is no indication from the recorded data that a steam explosion occurred.

References

1. "Summary of the TMI-2 Relocation Event," GPU Corp., March, 1988.

2. C. Blomquist, S. K. Wang, B. W. Spencer, and L. M. McUmber, "Corium Coolant Mixing Studies," to be published.

3. "Zion Probabilistic Safety Study," Commonwealth Edison Co. (1981).

4. IDCOR 15.2A

5. "Lower CSA Region," TMI-2 Technical Bulletin, TB 87-15 Rev. 1, GPU Nuclear Corporation, October 27, 1987.

6. "Upper Core Support Assembly Data Acquisition," TMI-2 Technical Bulletin, TB 88-01 Rev. 0, GPU Nuclear Corporation, February 16, 1988.

7. D. H. Cho, D. R. Armstrong, L. Bova, S. H. Chan, and G. R. Thomas, "Debris Bed Quenching Studies," Proceedings of the International Meeting on Thermal Nuclear Reactor Safety, Chicago, IL, August 29-September 2, 1982, NUREG/CP-0027, Vol. 2, p. 987, U. S. Nuclear Regulatory Commission (1982).

8. T. Ginsberg, J. Klein, C. E. Schwarz, and J. Klages, "Transient Core Debris Bed Heat Removal Experiments and Analysis, "Proceedings of the International Meeting on Thermal Nuclear Reactor Safety, Chicago, IL, August 29-September 2, 1982, NUREG/CP-0027, Vol. 2, p. 996, U. S. Nuclear Regulatory Commission (1982).

9. M. Epstein and H. K. Fauske, "The TMI-2 Core Relocation-Heat Transfer and Mechanism," EGG-TMI-7956, July 1987.

10. E. L. Tolman et al., "TMI-2 Accident Scenario Update," EGG-TMI-7489, December 1986.

11. R. E. Henry et al., "Core Relocation Phenomenology," Proceedings of the First International Information Meeting on the TMI-2 Accident," October 21, 1985, Germantown, MD, USA.

12. NSAC-28, "Interpretation of TMI-2 Instrument Data," Nuclear Safety Analysis Center (NSAC), EPRI, March 1980.

13. R. D. McCormick et al., "TMI-2 Data Summary Report," EGG-TMI-7843, September 1987.

14. J. L. Anderson, "Recommended HPI Rates for the TMI-2 Analysis Exercise (0-300 Minutes)," EGG-TMI-7833, September 1987.

15. N. Zuber, "On the Stability of Boiling Heat Transfer," Trans. ASME, Vol. 80, p. 711, 1958.

16. T. G. Theofanous, "The Cooldown Aspects of the TMI-2 Accident," NUREG/CR-4978, August 1987.

17. B. W. Spencer, J. J. Sienicki, and L. M. McUmber, "Hydrodynamic and Heat Transfer Aspects of Corium-Water Interaction," EPRI-NP-5127, 1987.

18. L. A. Neimark, R. V. Strain, J. E. Sanecki, and W. D. Jackson, "The Microstructural and Microchemical Characterization of Samples from the TMI-2 Core," Proceedings of the U.S. Nuclear Regulatory Commission Fourteenth Water Reactor Safety Information Meeting, Gaithersburg, MD, October 26-29, 1987, NUREG/CP-0091, Vol. 6, p. 199, U. S. Nuclear Regulatory Commission (February 1988).

19. W. A. Lambertson and M. H. Mueller, "Uranium Oxide Phase Equilibrium Systems: III, UO_2-ZrO_2," J. Amer. Ceram. Soc., 36, p. 365 (1953).

20. J. K. Fink, M. G. Chasanov, and L. Leibowitz, "Thermophysical Properties of Uranium Dioxide," J. Nucl. Materials, Vol. (102), pp. 17-25, 1981.

21. D. L. Hagrman, Personal communication, May 1982.

22. R. Brandt and G. Neuer, "Thermal Conductivity and Thermal Radiation Properties of UO_2," Journal of Non-Equilibrium Thermodynamics, 1, p. 3 (1976).

23. S. Nazaré, G. Ondracek, and B. Schulz, "Properties of Light Water Reactor Core Melts," Nucl. Tech., 32, p. 239 (1977).

24. "1983 ASME Boiler and Pressure Vessel Code," American Society of Mechanical Engineers, New York (1983).

25. Properties of Selected Ferrous Alloying Elements, Vol. III-1 of McGraw-Hill/CINDAS Data Series on Material Properties, ed. Y. S. Touloukian and C. Y. Ho, McGraw-Hill Book Company, New York, (1981).

26. Liquid Metals Chemistry and Physics, ed. S. Z. Beer, Marcel Dekker, Inc., New York (1972).

27. V. C. Levich, "Physiochemical Hydrodynamics," Prentice-Hall, Englewood Cliffs, NJ (1962).

28. N. Zuber, "The Dynamics of Vapor Bubbles in Non-Uniform Temperature Fields," Int. J. Heat Mass Trans., Vol. 2, p. 83, 1961.

29. G. I. Taylor, "The Shape and Acceleration of a Drop in a High Speed Air Stream," The Scientific Papers of G. L. Taylor, Ed. G. K. Batchelor, Vol. III, University Press, Cambridge, 1963.

30. V. K. Dhir and G. P. Purohit, "Subcooled Film-Boiling Heat Transfer From Spheres," Nucl. Eng. Design, Vol. 47, p. 49, 1978.

31. K. Kobayasi, "Film Boiling Heat Transfer Around a Sphere in Forced Convection," J. Nucl. Sci. Tech., Vol. 2, p. 62, 1964.

32. J. J. Sienicki and B. W. Spencer, "Superheat Effects on Localized Vessel Breach Enlargement During Corium Ejection," Transactions of the American Nuclear Society, Vol. 52, p. 522 (1986).

33. J. J. Sienicki and B. W. Spencer, "Analysis of Reactor Material Experiments Investigating Corium Crust Stability and Heat Transfer in Jet Impingement Flow," ANS Proceedings 1985 National Heat Transfer Conference, Denver, CO, August 4-7, 1985, p. 255, American Nuclear Society, LaGrange Park, IL (1985).

34. H. Martin, "Heat and Mass Transfer between Impinging Gas Jets and Solid Surfaces," Advances in Heat Transfer, ed. J. P. Hartnett and T. F. Irvine, Jr., Vol. 13, p. 1, Academic Press Inc., New York (1977).

ACKNOWLEDGMENTS

This work was funded by the U.S. Department of Energy under DOE Contract No. DE-AC07-761D01570. This work was performed at the request of General Public Utilities (GPU) Nuclear Corporation. The authors are indebted to GPU Nuclear for their support of this work, and to Mr. Robert Ryan of GPU in particular for his invaluable assistance. The efforts of V. Eustace, K. Rank, M. Heinig, L. Pavlik, and J. Kawka in preparing the manuscript and figures are deeply appreciated. The authors also wish to acknowledge Dr. Roger Tilbrook, ANL, for bringing this work to their attention.

APPENDIX A

CORIUM PROPERTIES

The corium is assumed to have a composition of 65 mole % UO_2 - 35 mole % ZrO_2 corresponding to the mean value obtained from chemical analysis of various samples retrieved from the lower head.[18] For these proportions, the UO_2-ZrO_2 phase diagram determinations of Lambertson and Mueller[19] provide a liquidus temperature of 2850 Kelvins (4670 degrees Farenheit). This value is assumed for the corium freezing and melting temperatures. Thus,

$$T_{liquidus} = 2850 \text{ K}. \tag{A.1}$$

The specific enthalpy of molten corium and the corium heat of fusion were obtained from the specific enthalpies for UO_2 and ZrO_2 recommended in References 20 and 21, respectively. Assuming that the enthalpy increases linearly between 298 Kelvins (77 degrees Farenheit) and the freezing temperature provides the following functional representations for the specific enthalpy of the corium solid and liquid phases:

$$h_{liquid} \text{ (MJ/kg)} = 1.497 + 0.5650 \times 10^{-3} (T - 2850), \tag{A.2}$$

$$h_{solid} \text{ (MJ/kg)} = 0.4447 \times 10^{-3} (T - 298.15). \tag{A.3}$$

In Equations A.2 and A.3, as well as below, the temperature is assumed to be in Kelvins. The difference between Equations A.2 and A.3 at the freezing temperature of 2850 Kelvins (4670 degrees Farenheit) corresponds to the corium heat of fusion,

$$h_{fusion} = 0.3624 \text{ MJ/kg}. \tag{A.4}$$

The density of molten corium was assumed given in terms of a mass fraction weighting of the specific volumes (i.e., inverse densities) of UO_2 and ZrO_2 at their respective liquidus states. The molten UO_2 density was taken equal to that recommended for UO_2 at the liquidus in Reference 20 while the liquidus density of ZrO_2 was obtained from Reference 21. The resulting density for liquid corium is

$$\rho_{liquid} = 7960\ kg/m^3. \tag{A.5}$$

This same value was also assumed for corium solidified as crust.

The corium thermal conductivity was taken equal to a mole fraction weighting of the thermal conductivities of UO_2 and ZrO_2,

$$k_{solid} = X_{UO_2}\, k_{solid\ UO_2} + X_{ZrO_2}\, k_{solid\ ZrO_2} \tag{A.6}$$

where

X_{UO_2} = mole fraction of UO_2,

X_{ZrO_2} = mole fraction of ZrO_2.

For solid UO_2, the conductivity was assumed given by the expression recommended by Brandt and Neuer,[22]

$$k_{solid\ UO_2}\ [W/(m \cdot K)] = \frac{1}{4.39 + 0.0216\ T}$$

$$+ 11.2 \times 10^{-4}\ T \exp\left(-\frac{1.18}{kT}\right) - 4.8 \times 10^{3} \exp\left(-\frac{3.29}{kT}\right), \tag{A.7}$$

where

k = Boltzmann's constant.

The activation energies in the exponential terms are given in units of electron-volts. It has been found computationally efficient to fit the following polynomial function to Equation A.7,

$$k_{solid\ UO_2}\ [W/(m \cdot K)] = 14.04 - 2.315 \times 10^{-2} T + 2.076 \times 10^{-5} T^2$$

$$- 9.661 \times 10^{-9} T^3 + 1.797 \times 10^{-12} T^4 + 1.101 \times 10^{-16} T^5$$

$$- 5.381 \times 10^{-20} T^6. \tag{A.8}$$

The solid ZrO_2 conductivity was taken equal to that recommended in Reference 21,

$$k_{solid\ ZrO_2}\ [W/(m\cdot K)] = 0.835 + 1.81 \times 10^{-4}\ T. \tag{A.9}$$

In evaluating the UO_2 thermal conductivity, the temperature used in Equation A.8 is defined as the actual temperature "renormalized" by the multiplicative factor 3138/2850 representing the ratio of the freezing temperatures of pure UO_2 and the corium mixture. Similarly, the temperature employed in Equation A.9 is the actual temperature multiplied by the factor 2973/2850 corresponding to the ratio of the freezing temperature of pure ZrO_2 and the corium mixture. This procedure is followed so that the mixture conductivity at the solidus is equal to a mole fraction weighting of the solidus conductivities of UO_2 and ZrO_2. The liquid corium thermal conductivity is assumed equal to the value of the solid corium thermal conductivity at the solidus. The resulting numerical value is given by

$$k_{liquid} = 2.88\ W/(m\cdot K). \tag{A.10}$$

The viscosity of molten corium was calculated with the method of da Andrade as discussed in Reference 23 whereby the viscosity at the liquidus is given by

$$\mu_{liquidus}\ (Pa\cdot s) = 6.12 \times 10^{-5}\ \frac{(T_{liquidus} A)^{1/2}}{(V)^{2/3}} \tag{A.11}$$

where

$T_{liquidus}$ = liquidus temperature,

A = atomic weight in g,

V = molar volume in cm^3.

Equation A.11 predicts a liquidus viscosity of

$$\mu_{liquidus} = 5.31 \times 10^{-3}\ Pa\cdot s. \tag{A.12}$$

Above the liquidus, the viscosity decreases with temperature as

$$\mu \propto \exp\left(\frac{Q}{RT}\right) \tag{A.13}$$

where the activation energy, Q, is given by

$$Q = 1.80330\ T_{liquidus}^{1.348}\ \text{J/mole} \tag{A.14}$$

and R = 8.31433 joules per mole per Kelvin is the universal gas constant. Equations A.12-A.14 provide the temperature dependent viscosity,

$$\mu(\text{Pa}\cdot\text{s}) = 1.675 \times 10^{-4} \exp\left(\frac{9848}{T}\right) . \tag{A.15}$$

Representative thermophysical properties for corium are shown in Table A.1.

Table A.1. Representative Thermophysical Properties of Corium Assumed in Analysis

Corium Composition, wt %	80.3 UO_2 + 19.7 ZrO_2
Corium Composition, mole %	65.0 UO_2 + 35.0 ZrO_2
Liquidus/Freezing Temperature, K	2850
Specific Enthalpy, MJ/kg	
Liquidus	1.50
Solidus	1.13
298 K	0
Heat of Fusion, MJ/kg	0.362
Specific Heat, kJ/(kg•K)	
Liquid	0.565
Solid	0.445
Density, kg/m^3	
Liquid	7960
298 K	9430
Thermal Conductivity, W/(m•K)	
Liquid	2.88
Solidus	2.88
Viscosity, Pa•s	
3050 K	4.23×10^{-3}
Liquidus	5.31×10^{-3}

APPENDIX B

REACTOR VESSEL LOWER HEAD PROPERTIES

The heatup and ablation of the reactor vessel lower head is calculated using properties for Type A-533 steel. This is a medium carbon, low alloy steel for which the composition range is 0.25% C, 1.07-1.62% Mn, 0.41-0.64% Mo, 0.17-1.03% Ni, 0.13-0.45% Si, 0.035% max P, 0.04% max S, and the remainder Fe.[24] Thermophysical property data for A-533 steel could be identified only for low temperatures less than approximately 1100 Kelvins (1520 degrees Farenheit). In view of a lack of high temperature data together with the low proportions of alloying elements, the lower head is described mainly in terms of properties for pure iron. The exception is the thermal conductivity below the iron Curie temperature (1043 Kelvins [1418 degrees Farenheit]) which is assumed equal to that recommended in Reference 24 for a representative 1.0% Mn, 0.5% Mo, 0.5% Ni medium carbon, low alloy steel. The resulting thermal conductivity is about 50% that of pure iron at room temperature and rises to ~90% of the iron value near the Curie temperature. Properties for iron were taken from Reference 25 where available. The liquid iron density was obtained from Reference 26. The molten iron thermal conductivity was approximated as constant above the liquidus temperature. The iron thermal conductivity at the liquidus was assumed to equal the value at the solidus divided by a factor of 1.6. As discussed in Reference 23, this ratio is appropriate for a metal such as iron which immediately below the solidus has a crystal structure in which each atom has eight nearest neighbors.

It was found computationally convenient to employ the following functional representations for the lower head properties in the calculations.

<u>Liquidus/Melting Temperature</u>

$$T_{liquidus} = 1811 \text{ K}. \tag{B.1}$$

<u>Specific Enthalpy</u>

For $T \geq 1811$ K,

$$h_{liquid}\ (MJ/kg) = 1.293 + 0.835 \times 10^{-3}\ (T - 1811); \qquad (B.2)$$

For $1667.01 \le T < 1811$ K,

$$h_{solid}\ (MJ/kg) = -3.666 \times 10^{-2} + 4.340 \times 10^{-4}T + 9.028 \times 10^{-8}T^{2}; \qquad (B.3)$$

For 1667 K $\le T <$ 1667.01 K,

$$h_{solid}\ (MJ/kg) = 0.9225 + 1.515(T - 1667); \qquad (B.4)$$

For 1185.01 K $\le T <$ 1667 K,

$$h_{solid}\ (MJ/kg) = 1.127 \times 10^{-2} + 4.083 \times 10^{-4}T + 8.299 \times 10^{-8}T^{2}; \qquad (B.5)$$

For 1185 K $\le T <$ 1185.01 K,

$$h_{solid}\ (MJ/kg) = 0.5956 + 1.61(T - 1185); \qquad (B.6)$$

For 1043 K $\le T <$ 1185 K,

$$h_{solid}\ (MJ/kg) = -9.293 \times 10^{3} + 3.257 \times 10^{1}T - 3.645 \times 10^{-2}T^{2} + 4.949 \times 10^{-6}T^{3} + 1.606 \times 10^{-8}T^{4} - 6.989 \times 10^{-12}T^{5} - 2.127 \times 10^{-15}T^{6} + 1.279 \times 10^{-18}T^{7}; \qquad (B.7)$$

For 1000 K $\le T <$ 1043 K,

$$h_{solid}\ (MJ/kg) = 1.660 \times 10^{4} - 6.517 \times 10^{1}T + 9.594 \times 10^{-2}T^{2} - 6.276 \times 10^{-5}T^{3} + 1.540 \times 10^{-8}T^{4}\ ; \qquad (B.8)$$

For 250 K $\leq$ T < 1000 K,

$$h_{solid}\ (MJ/kg) = -\ 8.484 \times 10^{-2} - 3.355 \times 10^{-7} T + 1.614 \times 10^{-6} T^{2}$$

$$-\ 2.703 \times 10^{-9} T^{3} + 1.679 \times 10^{-12} T^{4} + 1.723 \times 10^{-15} T^{5}$$

$$-\ 3.044 \times 10^{-18} T^{6} + 1.256 \times 10^{-11} T^{7}\ . \tag{B.9}$$

<u>Density</u>

$$\rho_{liquid}\ (kg/m^{3}) = 7010 - 8.3419 \times 10^{-1}\ (T - T_{liquidus})\ ; \tag{B.10}$$

$$\rho_{solid}\ (kg/m^{3}) = \frac{7867}{(1 + 0.01\ \frac{\Delta L}{L})^{3}}\ ; \tag{B.11}$$

For 1185 K $\leq$ T,

$$\frac{\Delta L}{L} = -\ 1.76805 + 0.00233\ T; \tag{B.12}$$

For 300 K $\leq$ T < 1185 K,

$$\frac{\Delta L}{L} = 0.009 + 1.210 \times 10^{-3}\ (T - 300) + 6.504 \times 10^{-7}\ (T - 300)^{2}$$

$$-\ 3.140 \times 10^{-10}\ (T - 300)^{3}. \tag{B.13}$$

<u>Thermal Conductivity</u>

$$k_{liquid} = 24.13\ W/(m \cdot K); \tag{B.14}$$

For $1185\ K \le T < 1811\ K$,

$$k_{solid}\ [W/(m\cdot K)] = 1.322 \times 10^{4} - 5.813 \times 10^{1} T + 1.053 \times 10^{-1} T^{2}$$

$$- 1.007 \times 10^{-4} T^{3} + 5.359 \times 10^{-8} T^{4} - 1.508 \times 10^{-11} T^{5}$$

$$+ 1.754 \times 10^{-15} T^{6}\ ; \tag{B.15}$$

For $1043\ K \le T < 1185\ K$,

$$k_{solid}\ [W/(m\cdot K)] = 30.4; \tag{B.16}$$

For $477.59\ K \le T < 1043\ K$,

$$k_{solid}\ [W/(m\cdot K)] = 8.623 \times 10^{2} - 7.083\ T + 2.504 \times 10^{-2} T^{2}$$

$$-4.630 \times 10^{-5} T^{3} + 4.718 \times 10^{-8} T^{4} - 2.515 \times 10^{-11} T^{5}$$

$$+ 5.478 \times 10^{-15} T^{6}\ ; \tag{B.17}$$

For $T \le 477.59\ K$,

$$k_{solid}\ [W/(m\cdot K)] = 41.19\ . \tag{B.18}$$

Viscosity

$$\mu\ (Pa\cdot s) = 2.21 \times 10^{-4} \exp\left(\frac{5776}{T}\right)\ . \tag{B.19}$$

Representative thermophysical properties for the lower head are shown in Table B.1.

Table B.1. Representative Thermophysical Properties of Reactor Vessel Lower Head Assumed in Analysis

Melting Temperature, K	1811
Specific Enthalpy, MJ/kg	
Liquidus	1.29
Solidus	1.05
470 K	0.858
298 K	0
Heat of Fusion, MJ/kg	0.247
Specific Heat, kJ/(kg•K)	
Liquid	0.835
Solidus	0.761
470 K	0.519
298 K	0.450
Density, kg/m^3	
Liquidus	7010
Solidus	7320
470 K	7810
298 K	7870
Thermal Conductivity, W/(m•K)	
Liquidus	24.1
Solidus	38.6
470 K	41.2
298 K	41.2
Liquidus Viscosity, Pa•s	5.36×10^{-3}

APPENDIX C

MODELING OF THERMAL AND HYDRODYNAMIC ASPECTS OF CORIUM JET/WATER INTERACTIONS

Based on the experimental results of the simulant material/water and corium/water tests carried out at ANL, a phenomenological model has been developed to describe the thermal and hydrodynamic behavior of a high-temperature corium jet when it interacts with water. the jet-breakup length and dispersed-particle-size distribution were analyzed based on Kelvin-Helmholtz instability on the jet column and boundary-layer stripping on the leading edge. The heat-transfer aspects, which strongly affect the jet-breakup behavior, also were analyzed to predict the generation and condensation of steam. The resulting vessel pressurization was estimated and a good agreement between predicted and experimental results was obtained.

Modeling of Pour-Stream Breakup

Based on the observation of simulant material tests, a conceptual configuration of the jet when it interacts with the water has been assumed as shown in Figure C.1. A vortex ball (i.e., the leading edge), followed by a coherent jet column, is usually formed immediately after the jet submerged into the water. The dynamic governing equations of the jet can be obtained by applying mass and force balance on the coherent column and the leading edge as the following:

$$2 \frac{\partial R_j}{\partial t} = -U_{E,J}; \quad R_J(o) = R_o \tag{C.1}$$

$$(\rho_m + \rho_\ell/2) \frac{\partial \left[U_L V_L\right]}{\partial t} = \rho_m \int_o^{R_J(t)|\text{at column/ball interface}} (U_J - U_L)\, U_J\, 2\pi r dr$$

$$+ (\rho_m - \rho_\ell)\, g\, \bar{V}_L - \rho_m U_L \frac{\partial V_{E,L}}{\partial t}$$

$$- \frac{1}{2} C_D \rho_\ell U_L^2 \pi R_L^2 \; ; \quad U_L(o) = U_J \tag{C.2}$$

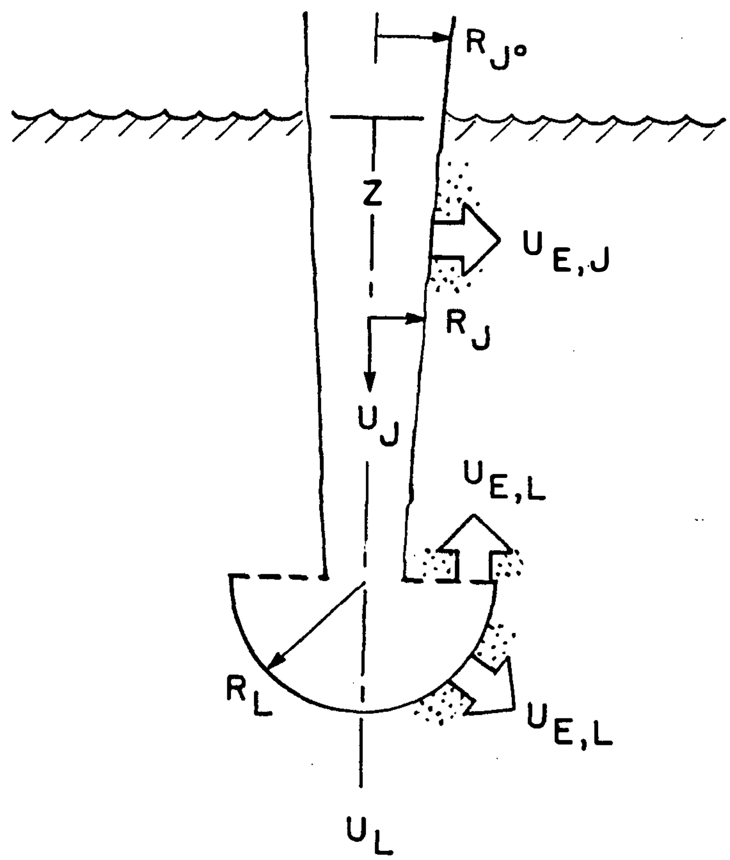

Figure C.1 Schematic Configuration of Jet Breakup

$$\frac{\partial \bar{V}_L}{\partial T} = \int_o^{R_J(t)|\text{at column/ball interface}} (U_J - U_L)\, 2\pi r dr - \frac{\partial \bar{V}_{E,L}}{\partial t} \; ; \; R_L(o) = R_J(o) \tag{C.3}$$

The time variations of the jet diameter, the leading-edge velocity, and the leading-edge volume can be determined from these simultaneous differential equations (C.1, C.2, and C.3), if the erosion velocities on the jet column and leading edge (i.e., $U_{E,J}$ and $U_{E,L}$) are known. It will be shown later that the erosion velocities depend strongly on the steam generated on the column and leading edge. Therefore, the jet-breakup behavior is coupled with the corium/water thermal interaction.

The Kelvin-Helmholtz instability at the liquid/vapor interface has been discussed by many authors.[27] The fastest growth rate and wave number of the interfacial disturbances were determined by differentiating the dispersion equation.[27] Then the erosion velocity of the dispersed particles at the interface due to droplets formation can be approximated by

$$U_E \approx \frac{\omega_p}{k_p} = \frac{1}{3} \frac{\rho_2}{\rho_1} U_2 \tag{C.4}$$

Therefore, the erosion due to Kelvin-Helmholtz instability depends on the vapor (steam) velocity in the vapor film. The erosion on the jet column is assumed due to this type of the instability solely.

By assuming a linear temperature profile in the vapor film and a parabolic profile for the liquid (water) velocity and the temperature in the liquid boundary layers, as shown in Figure C.2, and applying the mass, momentum, energy, and boundary equations the vapor velocity, growth of the vapor film, and the heat transfer coefficient, etc., were determined by solving the following equations:

$$\frac{\partial}{\partial z} \int_o^{\delta_\ell} U_\ell (U_\ell - U_\infty) dy_\ell = \int_o^{\delta_T} \beta_\ell (T_\ell - T_\infty) g dy_\ell - \nu_\ell \left. \frac{\partial U_\ell}{\partial y_\ell} \right|_{y_\ell = 0} \tag{C.5}$$

$$\frac{\partial}{\partial z} \int_o^{\min[\delta_\ell, \delta_T]} U_\ell \rho_\ell C_{p_\ell} (T_\ell - T_\infty) dy_\ell = - k_\ell \left. \frac{\partial T_\ell}{\partial y_\ell} \right|_{y_\ell = 0} \tag{C.6}$$

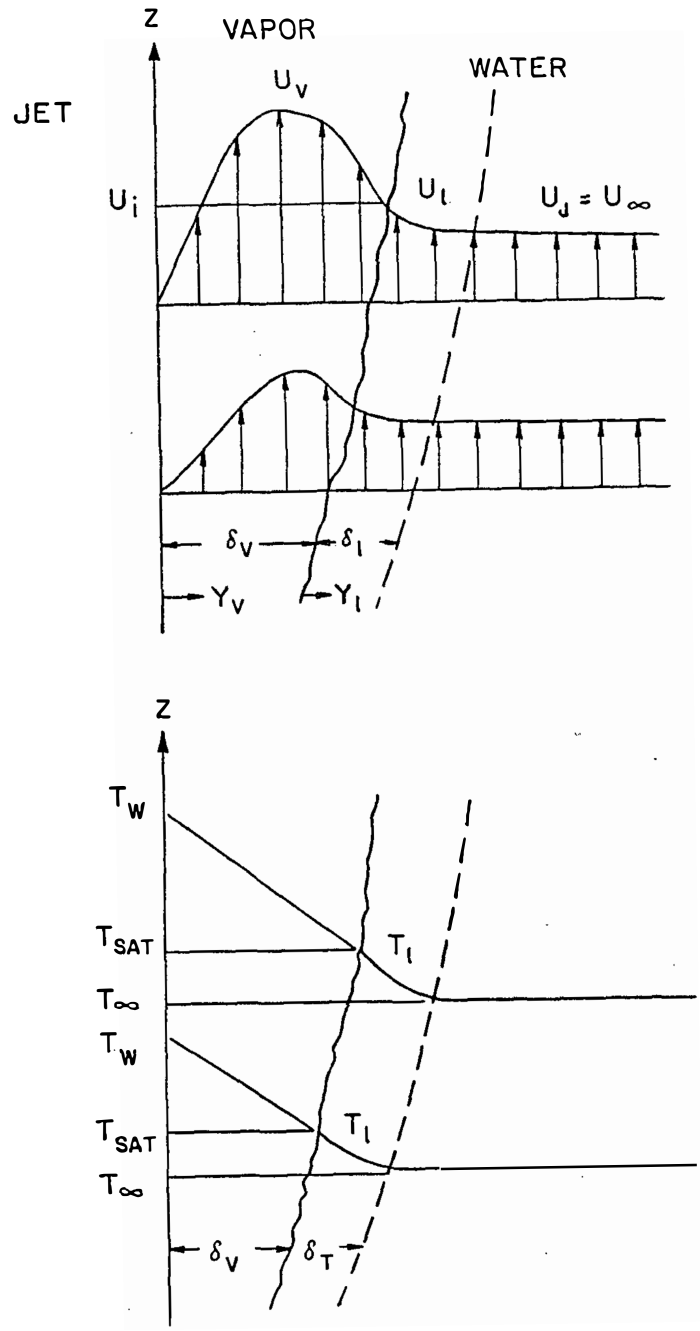

Figure C.2 Velocity and Temperature Profiles on Jet Column

$$\left(q''_R - k_v \frac{\partial T_v}{\partial y_v}\right) - \left(- k_\ell \frac{\partial T_\ell}{\partial y_\ell}\right) = \rho_v h'_{fg} \frac{\partial}{\partial z} \int_o^{\delta_v} U_v dy_v \tag{C.7}$$

$$\mu_v \left.\frac{\partial U_v}{\partial y_v}\right|_{y_v=\delta_v} = \mu_\ell \left.\frac{\partial U_\ell}{\partial y_\ell}\right|_{y_\ell=0} \tag{C.8}$$

$$\delta_t \simeq (\pi\ \alpha_\ell\ z/U_\infty)^{1/2} \tag{C.9}$$

$$\delta_\ell \simeq \delta_T\ Pr_\ell \tag{C.10}$$

Equation C.9 was based on the thermal transient boundary layer as developed by Zuber.[28]

In addition to the surface instability, aerodynamic stripping also accounts for the erosion on the leading edge. Taylor[29] investigated the surface-layer stripping of a large drop in a high speed air stream. He concluded that the surface layer is removed by tangential friction and the induced velocity in the surface layer shows a profile of boundary layer type. Assuming that the corium surface layer of the leading edge is constantly dragged by the enveloping fluid, i.e., steam, and departs from the main body at the tail edge due to an abrupt change in the pressure distribution, and assuming a velocity profile for the surface layer as per Taylor

$$U_m = U_{mi} \exp \left(- \frac{y_m}{C_m \sqrt{x}}\right) \tag{C.11}$$

The velocity and temperature profiles of vapor and liquid adjacent to the leading edge are similar to those of the jet column except z is replaced by x and g is replaced by g sinθ, as shown in Figure C.3. In addition to Equations

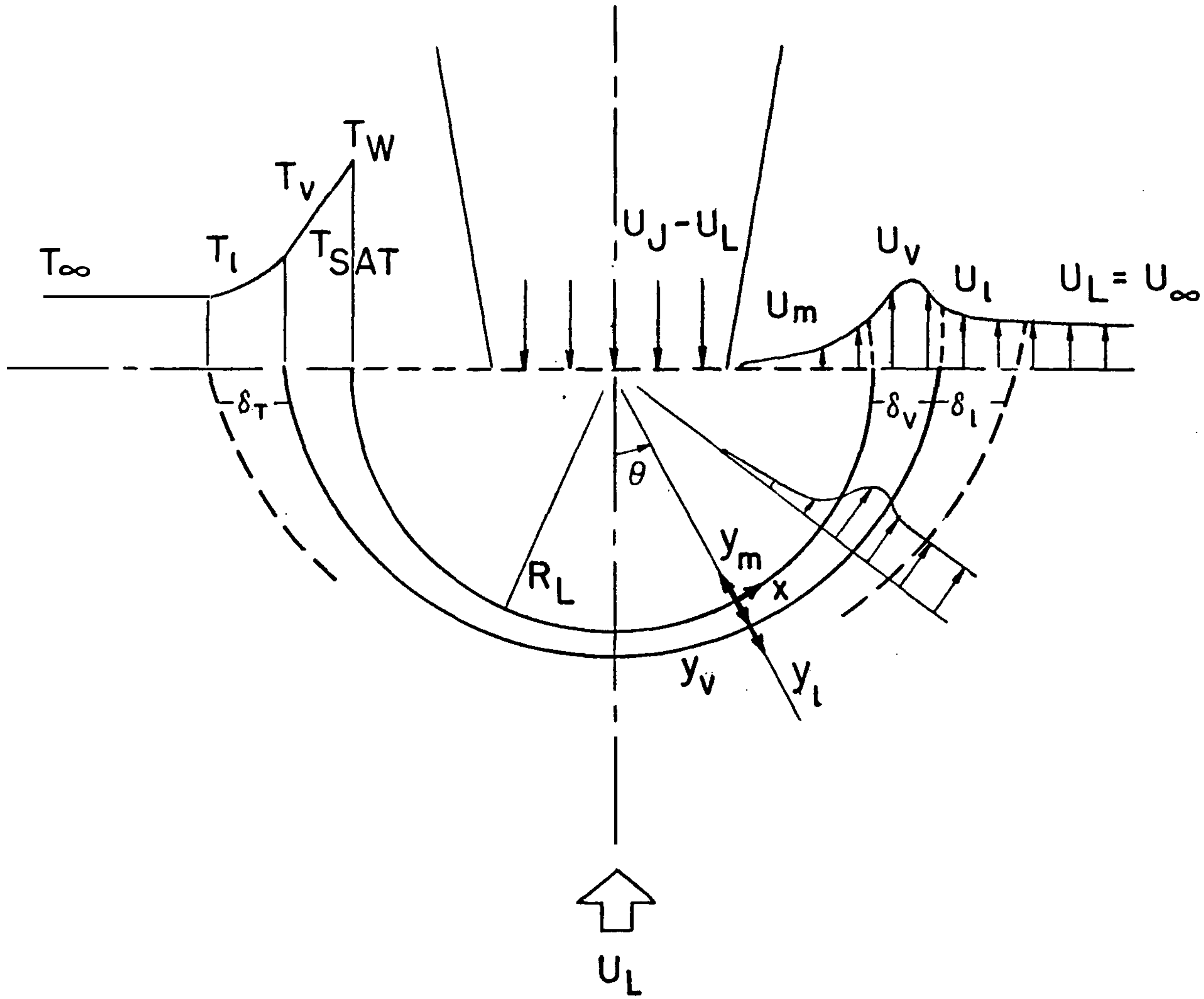

Figure C.3 Film Boiling and Erosion on Leading Edge

C.5-C.10, two more equations are needed:

$$\frac{\partial}{\partial x}\int_{o}^{\infty} U_m^2 \, dy_m = \nu_m \left.\frac{\partial U_m}{\partial y_m}\right|_{y_m=o} \tag{C.12}$$

and

$$\mu_m \left.\frac{\partial U_m}{\partial y_m}\right|_{y_m=o} = \mu_v \left.\frac{\partial U_v}{\partial y_v}\right|_{y_v=o} \tag{C.13}$$

The erosion velocity (or the rate change of the volume) on the leading edge can be approximated by:

$$\frac{\partial \bar{V}_{E,L}}{\partial t} = \int_{o}^{R_L} 2\pi R_L U_m \Big|_{\theta=\pi/2} dR_L \simeq 2\pi U_{mi} C_m \sqrt{\frac{\pi R_L}{2}} \left(R_L - C_m \sqrt{\frac{\pi R_L}{2}}\right) \tag{C.14}$$

After the erosion velocities on the column and leading edge are calculated, the jet breakup behavior can be completely determined by solving Equations C.1, C.2, and C.3.

<u>Dispersed Particle Size Distribution</u>

As described before, the diameter of the particles dispersed from the jet column surface due to Kelvin-Helmholtz instability is approximately by the wavelength of the most unstable wave. Thus,

$$D_p \sim \frac{1}{k_p} = \frac{3\sigma_1}{2\rho_2 U_2^2} \tag{C.15}$$

However, the particles dispersed from the tail of the leading edge may show quite a different size distribution since the erosion mechanism is completely different. Presumably, the drag-induced energy is lost at the tail in the form of the kinetic energy of dispersed particles and the formation of a new surface area. Then the particle size can be estimated by solving the following equation:

$$\frac{1}{2}\rho_m \int_0^\infty 2\pi\ (R_L - y)U_m^3\Big|_{x=\pi(R_L/2)}\ dy$$

$$= \frac{6\sigma_m}{D_p}\left(\frac{\partial\bar{V}_{E,L}}{\partial t}\right) + \frac{1}{8}\rho_m U_{mi}^2 \left(\frac{\partial\bar{V}_{E,L}}{\partial t}\right) \tag{C.16}$$

For a thin corium boundary layer, Equation C.16 can be simplified to yield

$$D_p = \frac{144\sigma_m}{\rho_m U_{mi}^2} \tag{C.17}$$

Comparing Equations C.15 and C.17, the dispersed particles of the leading edge are usually ~1 to ~10 times bigger than the dispersed particles of the jet column during the corium/water interaction.

Film Boiling Heat Transfer on Particles

The heat transfer from a descending, dispersed particle is illustrated in Figure C.4. For simplicity, heat conduction is neglected in the trailing vapor dome. The vapor velocity in the vapor film, the film thickness, and the heat transfer coefficient, etc., can be determined by solving the equations similar to Equations C.5-C.10 except the curvature on the particle is considered. The average heat transfer coefficient, $\bar{h}$, is approximated by

$$\bar{h} = \frac{1}{4\pi R^2}\left\{\int_0^{\pi/2}\left(q''_R - k_v \frac{\partial T_v}{\partial r}\Big|_R\right) 2\pi R^2 \sin\theta d\theta + \int_{\pi/2}^{\pi} q'' 2\pi R^2 \sin\theta d\theta\right\} \tag{C.18}$$

Figures C.5 and C.6 show a comparison of the heat transfer during forced film boiling of saturated water from a 19-millimeter (0.748-inch) diameter stainless steel sphere as predicted by Dhir et al.,[30] Kobayasi,[31] and the present

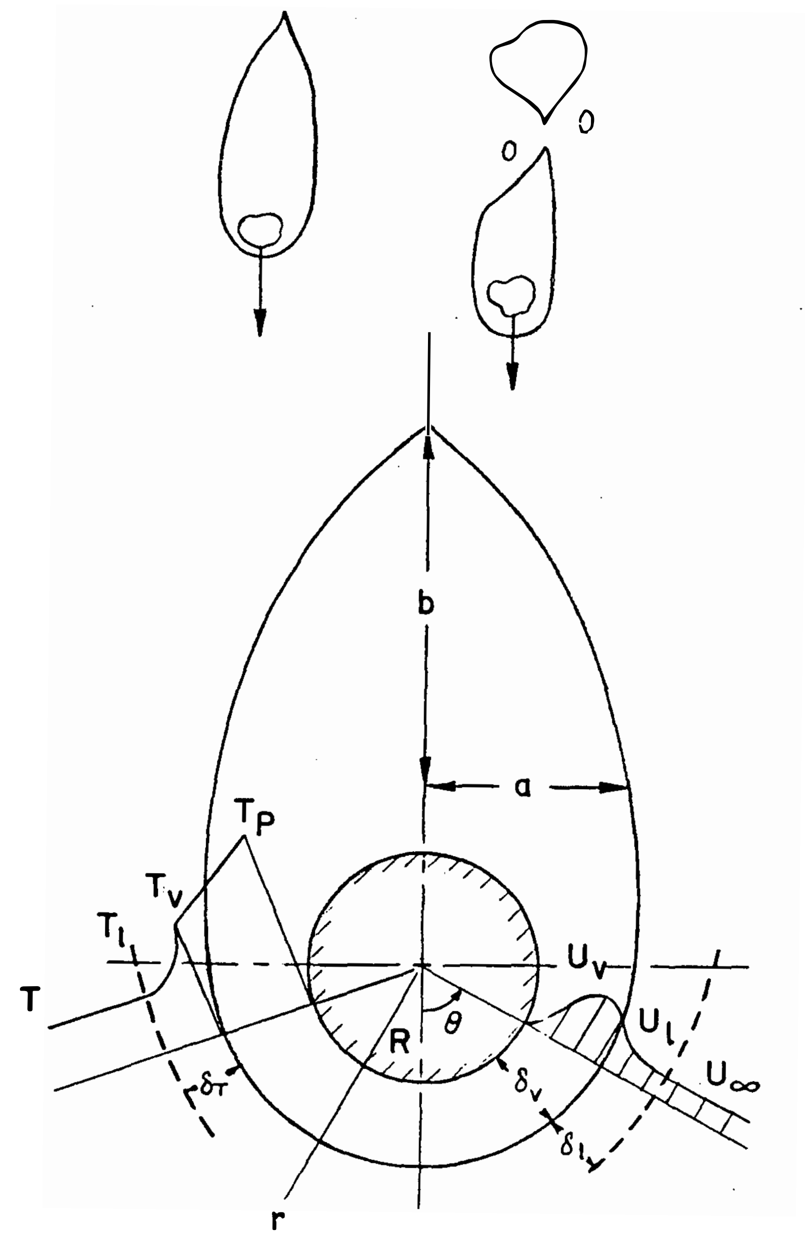

Figure C.4 Film Boiling on Descending Particle

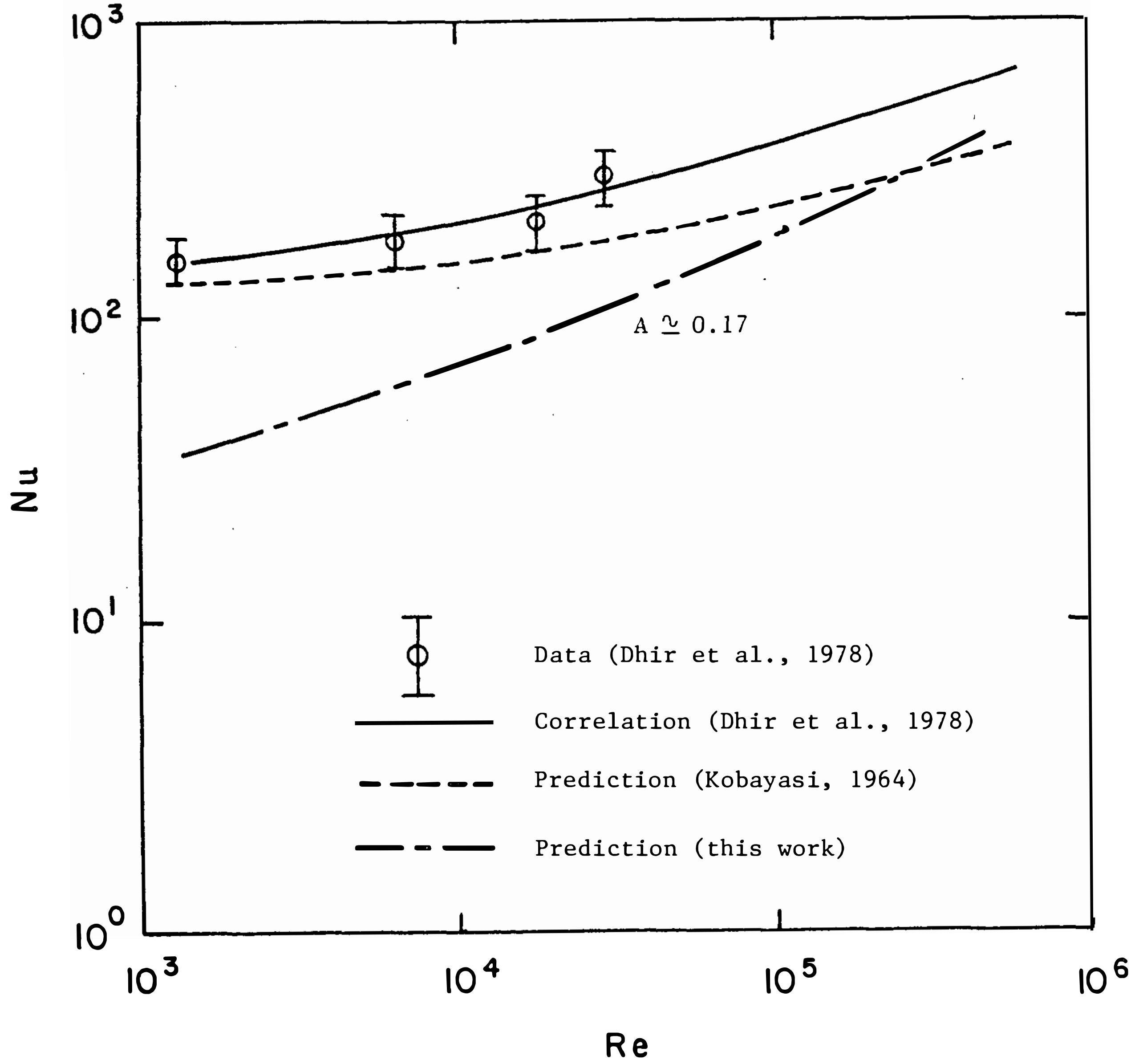

Figure C-5. Film Boiling Heat Transfer on Sphere

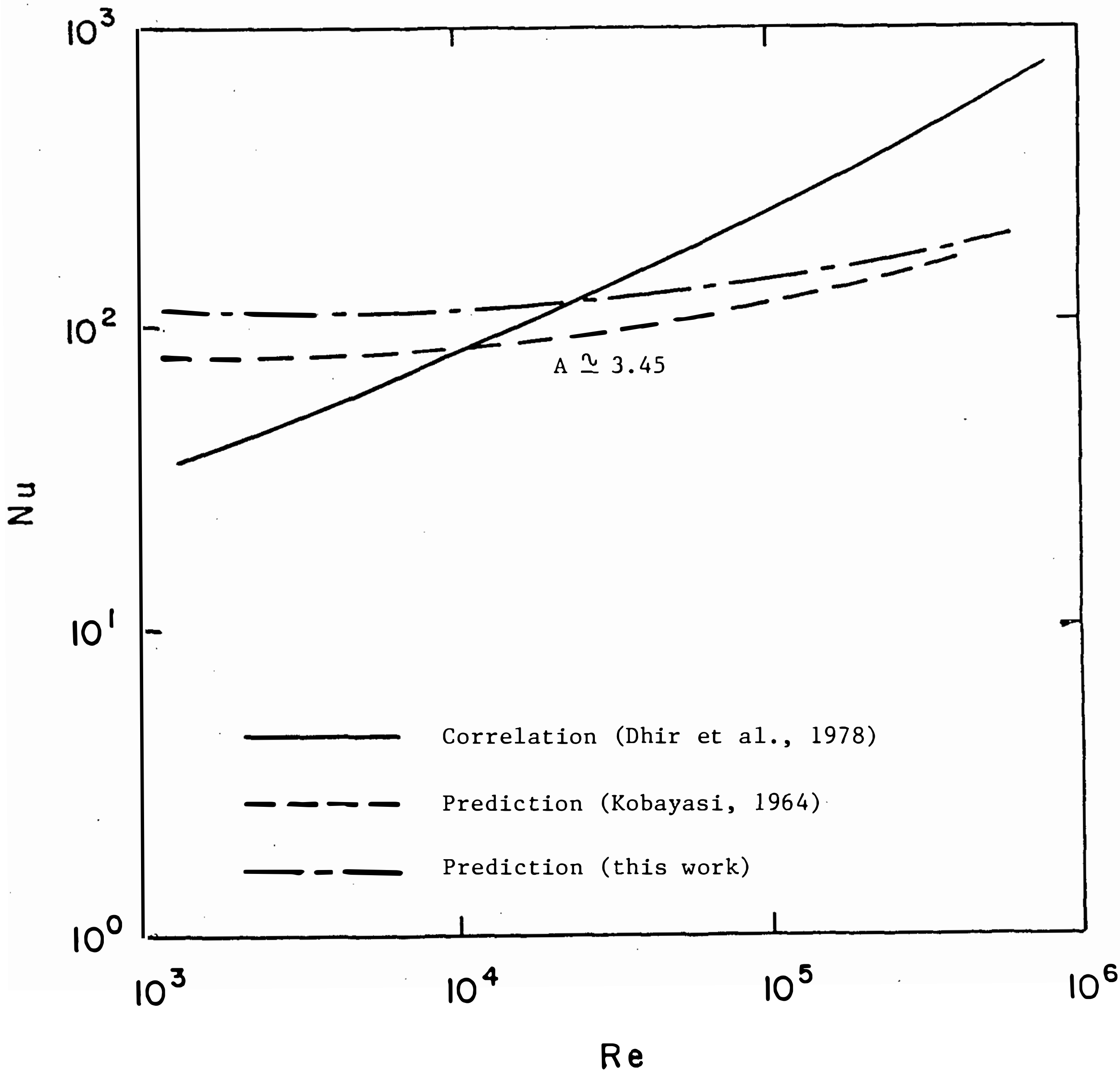

Figure C-6. Film Boiling Heat Transfer on Sphere work. In general, this work underestimates the heat transfer for a lower particle temperature as shown in Figure C.5 with A = 0.17 (i.e., T_p ~800 Kelvins [980 degrees Farenheit]). This is due to the fact that at this temperature radiation is negligible and conduction becomes significant in the vapor "dome" which is not much thicker than the vapor film. Therefore, the model of the present work is not recommended for cases with low particle temperatures. However, as the particle temperature increases, the present work agrees very well with Kobayasi's prediction as shown in Figure C.6 for A = 3.45 (i.e., T_p ~3000 Kelvins [4940 degrees Farenheit]).

The effect of water subcooling on film boiling heat transfer is shown in Figure C.7. The heat transfer is seen to increase with water subcooling and flow velocity. However, the enhancement of the heat transfer due to subcooling diminishes with increasing particle temperature as also confirmed by Dhir et al.[30]

The heat contributed to the evaporation of water (i.e., steam generation), as characterized by $\bar{h}_{EVAP}$, was predicted and is shown in Figure C.8 as a function of particle temperature for 50 Kelvins (90 Farenheit degrees) subcooling. The effect of liquid subcooling on the reduction of steam generation becomes less important as the particle temperature increases (i.e., A increases) and the ambient fluid velocity decreases. However, this conclusion has yet to be verified experimentally.

Prediction and Comparison of Steam Generation Rate and Vessel Pressurization

The pressurization is mainly composed of three main parts: (i) the pressure transient of the initial inerting gas (i.e., air or argon), (ii) the pressurization due to steam generation, and (iii) the pressurization due to hydrogen generation. If the vessel is much larger than the water volume and the vessel temperature did not change significantly during the interaction, (i) can be neglected. The pressurization due to steam generation was estimated based on the assumption that steam would rapidly reach a thermodynamic equilibrium in the expansion vessel without significant condensation since the vessel was heated initially. Therefore, the pressure was predicted by dividing the calculated mass of steam by the free air space of the expansion vessel and then by using steam tables to determine the pressure, given the specific volume and temperature. Hydrogen is treated as perfect gas when (iii) is

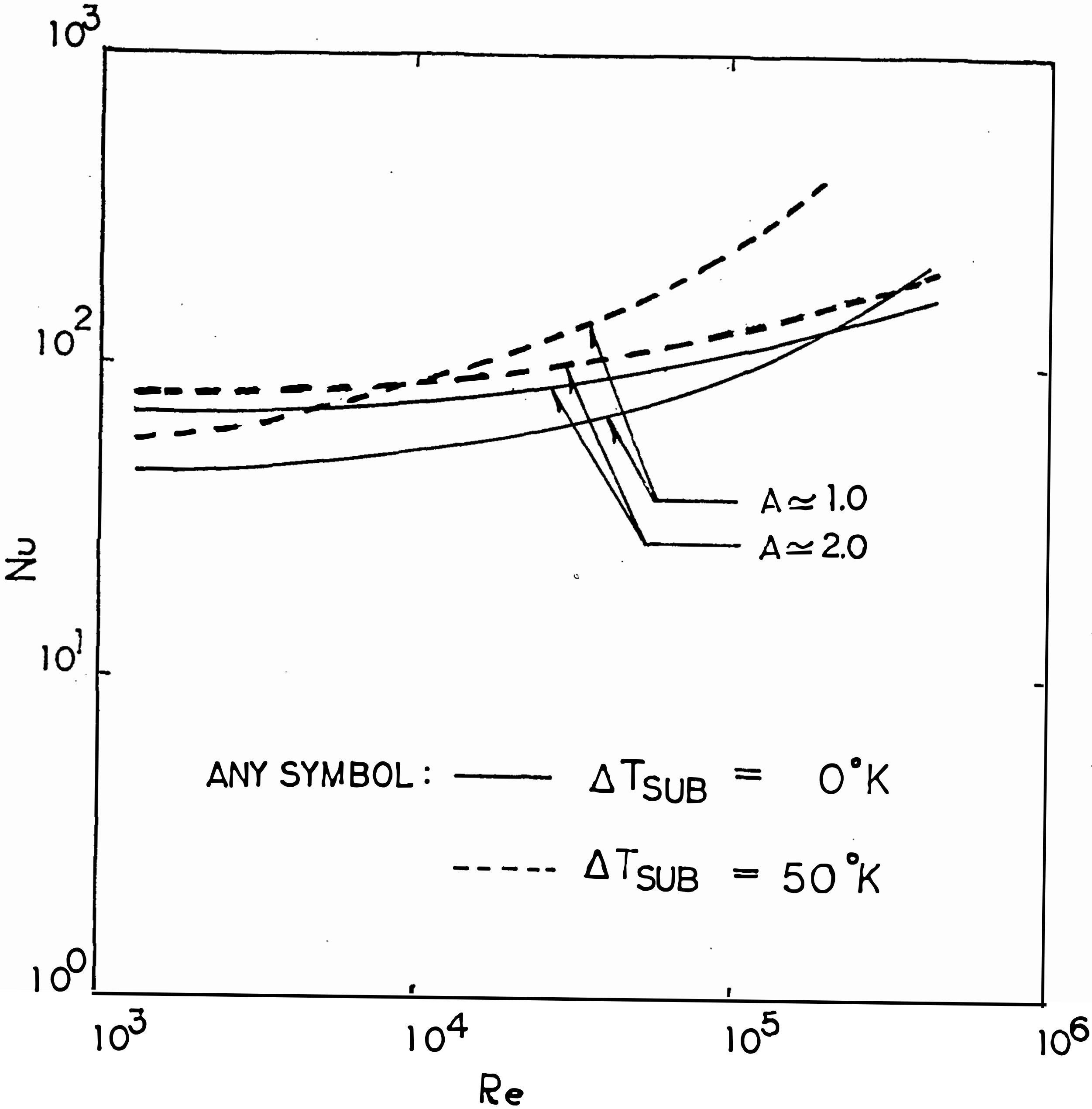

Figure C.7 Effect of Liquid Subcooling on Film Boiling Heat Transfer

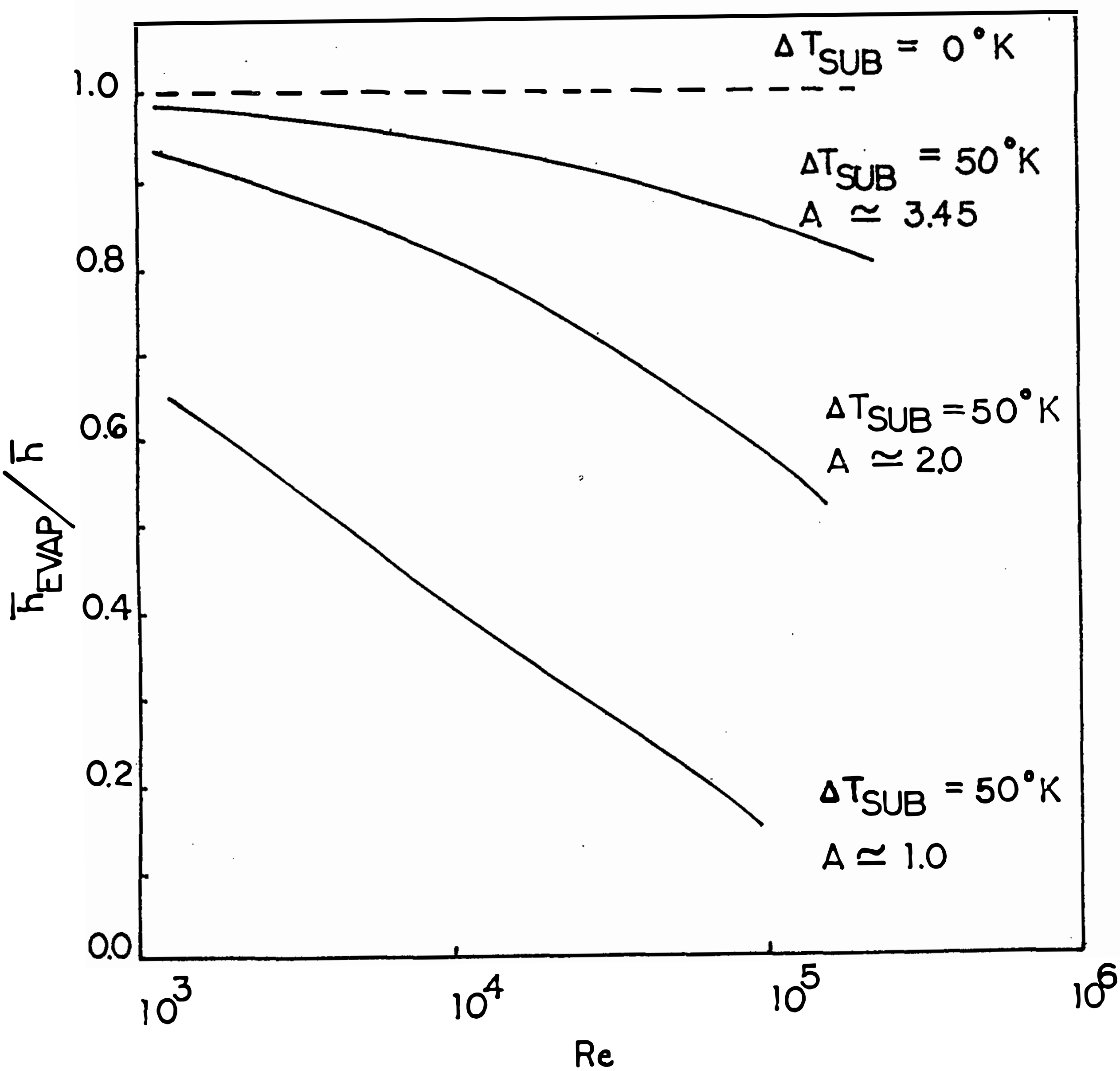

Figure C.8 Effect of Liquid Subcooling on Water Evaporation calculated. In general, the pressurization data can be predicted fairly well by the present model.

APPENDIX D

CORIUM SPREADING AND DRAINAGE INSIDE THE CORE FORMER REGION

Corium which flows through a hole in the baffle plate to enter the core former region (CFR) will accumulate upon the horizontal core former plate immediately below the breach. As the depth of the molten corium layer increases, the corium will tend to spread laterally over the former plate under the influence of gravity. However, the extent of corium spreading is restricted by drainage through the flow holes in the core former plate. In particular, each former plate contains eighty circular holes each having a diameter of 1 5/16 inch (3.33 centimeters). The total drainage area corresponds to 5.08% of the plate cross-sectional area. Thus, molten corium will successively accumulate upon and drain through the former plates underlying the baffle breach. The baffle plate structure may be postulated to be breached between the fifth and sixth former plates (counting downward from top to bottom) and may thus drain through the sixth, seventh, and eighth former plates prior to reaching the lower ribbed grid plate at the elevation of the bottom of the core. Ultimately, corium will drain through the peripheral part of the lower ribbed grid plate to enter the lower head region interior to the core support assembly. Examination of the core former region has revealed debris solidified between the lower core former plates over about three-fourths of the circumference of the core barrel.[6] In addition, examination of the core support assembly structure has shown the presence of corium over a similar extent of the vessel circumference.[5]

An analysis has been carried out of the spreading and drainage of corium flowing over a horizontal core former plate. The principal objective is to predict the extent of spreading around the circumference of the core former region for the case where corium enters the CFR through a localized breach in the baffle plate structure.

A simple model was developed to investigate simultaneous spreading and drainage inside a one-dimensional channel of uniform width. Steady-state conditions are assumed whereby the local horizontal spreading velocity is given by

$$U_{spread} = \sqrt{2g(Z_o - Z)} \tag{D.1}$$

where

U_{spread} = local horizontal velocity of fluid,

g = gravitational acceleration,

Z_o = gravity driving head,

Z = local depth of fluid.

The local velocity of gravity-driven drainage through the flow holes is assumed to equal

$$U_{drain} = C(2gZ)^{1/2} \tag{D.2}$$

where

U_{drain} = velocity of fluid draining downward through hole,

C = discharge coefficient.

Conservation of mass provides the equation,

$$\frac{d}{dx}(w\, U_{spread} Z) = -aC(2gZ)^{1/2} , \tag{D.3}$$

where

x = displacement along channel,

w = channel width,

a = flow hole drainage area per unit channel length.

The drainage area per unit length, a, is currently taken to be constant such that the effects of the flow holes are effectively smeared over the channel length as well as its width. This is expected to be a good assumption for the former plate since the normal flow area constitutes only five percent of the former plate cross-sectional area. The channel width, w, is also assumed to be constant over the length of the channel. From Equation D.2 the total flowrate of fluid through the flow holes is given by

$$G = 2\rho Ca\int_{0}^{L} dx(2gZ)^{1/2} \qquad (D.4)$$

where

G = total mass flowrate,

ρ = fluid density,

L = distance from symmetry plane at which the fluid depth goes to zero.

In writing Equation D.4, the corium is assumed to spread symmetrically on both sides of the fluid source corresponding to corium entering through the breached baffle plate. The distance over which corium floods the former plate is thus given by 2L.

Equation D.3 does not contain a local source term for corium addition to the layer. Consequently, the solution strictly applies to the plate immediately beneath the breach location. However, all of the former plates have an identical configuration of flow holes. Thus, if a corium mass is draining through a particular set of holes located in one plate, then an equal mass of corium would be expected to drain through the corresponding set of holes in the underlying plate under quasi-steady conditions. It follows that the fluid distributions at successively underlying plates would be expected to be quite similar in both extent and shape. Thus, an examination of spreading upon the uppermost plate is sufficient to predict the extent of spreading.

The current analysis does not consider the effects of freezing of corium which will further limit the corium penetration. In reality, corium crusts will form on the underlying structure and flowing molten corium will lose energy by forced convection heat transfer into the crust and steel substrate. In addition, the corium layer will lose energy from its upper surface. Reduction of the corium temperature and freezing may be enhanced by the presence of water inside the CFR. In general, the effects of heat transfer upon corium penetration are expected to be significant for thin corium layers of the order of one or two centimeters. For greater depths, layer surface-to-volume effects are expected to minimize the effects of heat transfer permitting the penetration of bulk corium masses over distances of one meter or more in the absence of drainage.

To obtain a differential equation for the local fluid depth in the simple model, Equation D.1 is substituted into Equation D.3 to obtain

$$w \frac{d}{dx}\left[Z\sqrt{2g(Z_o - Z)}\right] = -aC(2gZ)^{1/2} . \qquad (D.5)$$

Introducing the dimensionless depth, y, defined by

$$Z = \frac{Z_o}{2}(1 + y) , \qquad (D.6)$$

Equation D.5 is equivalent to the equation,

$$\frac{(\frac{1}{2} - \frac{3}{2} y)}{(1 - y^2)^{1/2}} \frac{dy}{dx} = - \frac{2aC}{wZ_o} . \qquad (D.7)$$

This equation may be integrated to obtain the solution,

$$\frac{2aC}{wZ_o} x = e - \frac{1}{2} \sin^{-1} y - \frac{3}{2}(1 - y^2)^{1/2} \qquad (D.8)$$

where e is a constant of integration. Equation D.9 has a physically realistic solution only when

$$y \le \frac{1}{3}$$

or

$$Z \le \frac{2}{3} Z_o \ . \qquad \text{(D.9)}$$

The significance of Equation D.9 is that the solution applies only to those portions of the channel in which the fluid depth is less than or equal to two-thirds of the driving head. This is not a serious limitation because the model does not include the jet impingement region in which fluid is delivered into the spreading layer. The peak fluid depths are attained inside the impingement zone. In actuality, the impingement region is expected to be a small portion of the CFR circumference. Accordingly, the impingement zone has been ignored on the basis of its small width in the current simple analysis. Presently, the maximum depth is assumed to equal two-thirds of the driving head, consistent with Equation D.9. Taking this to be the value at x equal to zero provides the solution

$$\frac{2aC}{wZ_o} x = \frac{1}{2} \sin^{-1} \frac{1}{3} + \frac{3}{2} [1 - (1/3)^2]^{1/2} - \frac{1}{2} \sin^{-1} y - \frac{3}{2} (1 - y^2)^{1/2} \qquad \text{(D.10)}$$

A fluid depth of zero corresponds to y = -1. For this value, Equation D.10 provides the spreading half-distance,

$$L = \frac{wZ_o}{2aC} \left[\frac{1}{2} \sin^{-1} (1/3) + \frac{3}{2} [1 - (1/3)^2]^{1/2} + \frac{\pi}{4} \right]. \qquad \text{(D.11)}$$

The model therefore provides a simple expression for the maximum fluid penetration.

Changing variables in Equation D.4 and using Equation D.7 yields an expression for the total flowrate,

$$G = \rho w Z_o (g\ Z_o)^{1/2} \int_{-1}^{1/3} dy \frac{(\frac{1}{2} - \frac{3}{2})y}{(1 - y)^{1/2}} , \qquad \text{(D.12)}$$

which upon integration provides

$$G = \rho w Z_o \frac{4}{3} (\frac{2}{3} g Z_o)^{1/2} . \qquad (D.13)$$

This equation determines the driving head, Z_o, for a specified total mass flowrate as

$$Z_o = \frac{G}{\rho w} \left[\frac{3}{4(\frac{2}{3} g)^{1/2}}\right]^{2/3} . \qquad (D.14)$$

From Equations D.11 and D.13, the flowrate may be related to the spreading distance,

$$G = 2\rho a L \frac{4C}{3(2)^{1/2}\left[\frac{1}{2} \sin^{-1} (1/3) + \frac{3}{2} [1 - (1/3)^2]^{1/2} + \frac{\pi}{4}\right]} (2g \frac{2}{3} Z_o)^{1/2} . \qquad (D.15)$$

Equation D.14 can be used to define a mean drainage velocity over the spreading distance,

$$\bar{U}_{drain} = \frac{4C}{3(2)^{1/2} \left[\frac{1}{2} \sin^{-1} (1/3) + \frac{3}{2} [1 - (1/3)]^{1/2} + \frac{\pi}{4}\right]} (2g \frac{2}{3} Z_o)^{1/2} . \qquad (D.16)$$

Evaluating the constants provides

$$\bar{U}_{drain} = 0.3979 \; C(2g \frac{2}{3} Z_o)^{1/2} . \qquad (D.17)$$

The fluid depth distribution given by Equation D.10 is shown in Figure D.1 in terms of a nondimensional depth, Z/Z_o, plotted versus a nondimensional distance, x/L. Of course, the corium distribution would be symmetric about the vertical axis.

The simple model was applied to drainage from a TMI core former plate.

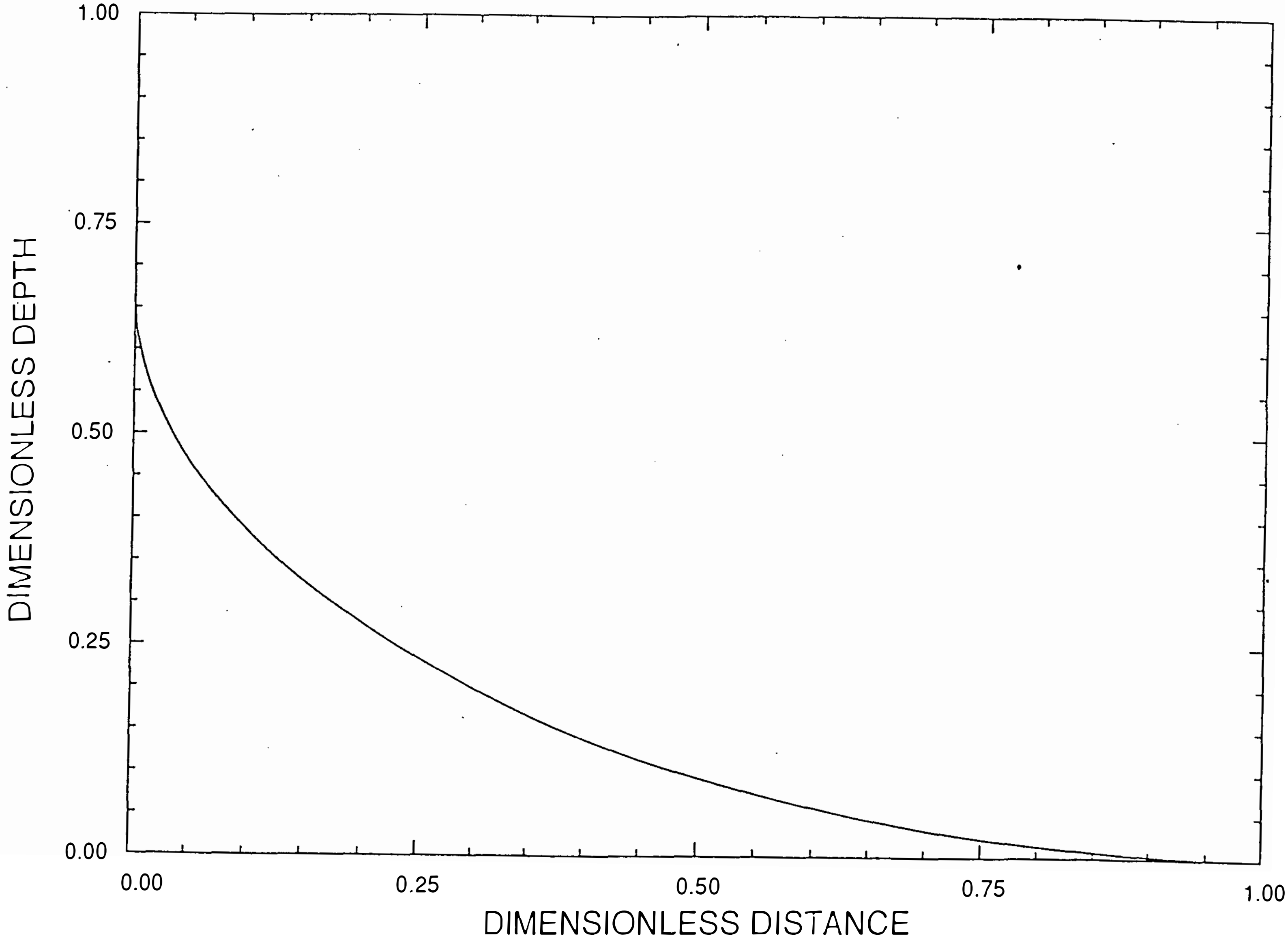

Figure D.1 Fluid Depth Distribution in Terms of Depth Nondimensionalized by Driving Head versus Distance Nondimensionalized by Maximum Penetration.

The plate cross-sectional area has a value of 1.375 square meters (2132 square inches).[6] Over the core barrel inner circumference of 1.125 meter (3.691 feet), this corresponds to a mean CFR width of 12.23 centimeters (4.815 inches) between the baffle plates and the core barrel. Corium draining through the flow holes will heat up and eventually ablate the surrounding 3.175 centimeters (1.25 inch) thick plate steel. Ablation-induced enlargement of the hole will increase the local drainage while progressively decreasing the spreading-induced lateral penetration. To carry out the analysis, a simplifying assumption was made that all of the flow holes within the spreading region are eroded at the same rate corresponding to the mean drainage velocity given by Equations D.16 or D.17. In actuality, the holes closer to the baffle breach would be enlarged at a greater rate while holes farther away grow more slowly. This effect would tend to emphasize drainage in the vicinity of the baffle breach at later times. However, using the mean velocity is expected to still provide a good prediction of the spreading distance. The discharge coefficient was assumed to have a value of 0.61. The time dependent diameter of the flow holes was calculated using the breach enlargement model described in Ref. 32. For the small plate thickness, forced convection heat transfer from the flowing molten corium to the steel is expected to exceed that which would be predicted by correlations for fully developed pipe flow. Accordingly, the heat transfer coefficient was assumed given by an expression appropriate for entrance region flow averaged over the plate thickness. In particular,

$$h = \left(\frac{4\mathrm{RePrD}}{\pi Z_{\mathrm{plate}}}\right)^{1/2} \frac{k}{D} \qquad \text{(D.18)}$$

where

h = forced convective heat transfer coefficient,

Re $= \dfrac{\rho \bar{U}_{drain} D}{\mu}$,

= Reynolds number,

Pr $= \dfrac{C_p \mu}{k}$,

- = Prandtl number,
- D = time dependent breach diameter,
- Z_{plate} = plate thickness,
- k = molten corium thermal conductivity,
- ρ = molten corium density,
- μ = molten corium viscosity,
- C_p = molten corium specific heat.

The heat transfer coefficient is observed to be independent of the breach diameter. The pre-melting energy deposited in the steel is accounted for in the ablation rate by the same approach as discussed in Appendix F. Steel heatup and ablation were calculated assuming the thermophysical properties for corium and stainless steel discussed above. The corium superheat was taken equal to 200 Kelvin (360 Farenheit degrees). The drainage area per unit length is defined as

$$a = \frac{80 \frac{\pi}{4} D_{hole}^2}{\pi D_{CB}} \tag{D.19}$$

where

- D_{hole} = time dependent diameter of an individual flowhole,
- D_{CB} = core barrel inner diameter.

Prior to ablation, a has an initial value of 0.621 centimeter (0.244 inch).

As noted above, debris was found solidified inside the CFR.[3] In specific locations, the debris was revealed in the form of "small rocks" typically 2.5 centimeters (0.98 inch) or less in diameter. In other places, fine particulate which was described as "sand-like," was observed. The CFR was estimated to contain 4.2 tonnes (9200 pounds) of debris.[3] It is speculated here that this debris might have been largely formed during the initial phases of corium relocation through the CFR. In particular, the small jet size characteristic of the initial baffle breach or the nominal flow hole diameter would be expected to be accompanied by jet breakup and particulate formation forming debris beds atop the former plates. Water is expected to be an ingredient in the jet breakup processes here. Specifically, water will be present when corium first enters the CFR. Subsequently, water may be expelled from the former region in the vicinity of the baffle breach and regions of greater corium accumulation thereby allowing molten corium to form a spreading layer. Unfortunately, an assessment of the corium quenching induced pressure-driven expulsion of water from the CFR is beyond the scope of the present analysis. The effects of debris beds assumed to exist atop the former plate are accounted for in the calculations by multiplying the spreading channel width by a factor of 0.4 representative of the void fraction inside a bed. This provides an effective width of 4.89 centimeters (1.93 inch).

The total corium flowrate through the CFR was set equal to that corresponding to the uniform drainage of 20 tonnes (44000 pounds) of corium over a timescale of 90 seconds. The total cumulative corium mass which has drained through the former plate together with the corresponding driving head, Z_o, predicted from Equation D.14 are shown in Figure D.2. The driving head of 0.3 meter (0.98 foot) represents a maximum layer depth of about 0.2 meter (0.66 foot). This is less than the former plate vertical separation distance of 0.6 meter (2.0 feet). The corresponding mean drainage velocity (Equation D.17) has a value of 0.48 meter per second (1.6 feet per second) over the drainage interval. Ablation of steel and hole enlargement are predicted not to begin until 29 seconds following the onset of corium flow into the CFR. Figure D.3 shows the calculated time dependent hole diameter representative of the mean drainage velocity. The enlargement of the flow holes proceeds at a constant rate reflecting the constant mean drainage velocity. The final hole diameter is nearly a factor of three times the initial value. The lateral spreading potential of the corium is illustrated by Figure D.4 which shows the fraction of the former plate length flooded with corium (also called the spreading fraction) defined as

$$\eta = \frac{2L}{\pi D_{CB}} \quad . \tag{D.20}$$

During the pre-ablation heatup phase, the spreading fraction has a value of 0.82. The spreading fraction decreases after 29 seconds due to the enlargement of the former plate flow holes. The calculation predicts that corium

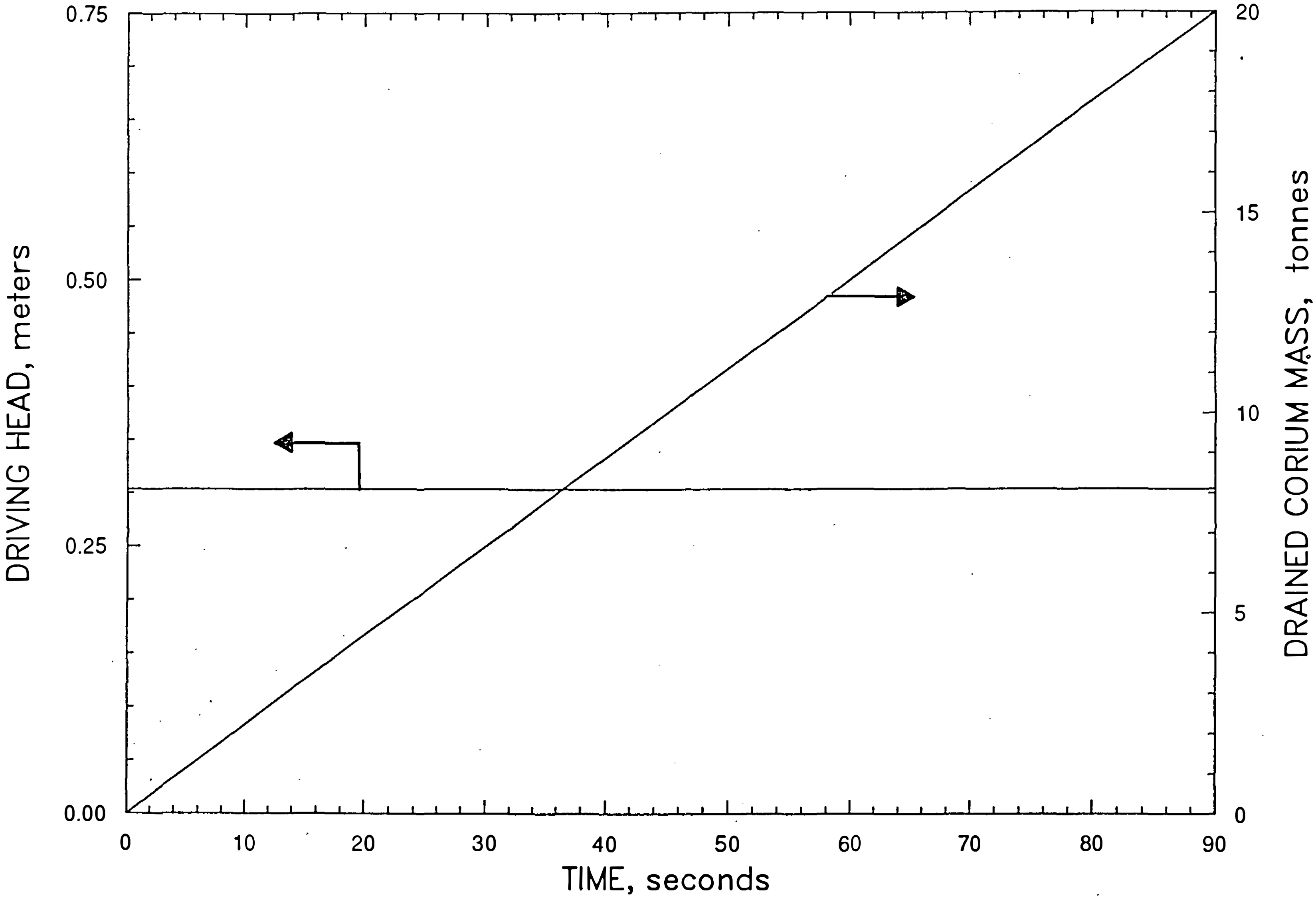

Figure D.2 Driving Head and Drained Corium Mass for Case of Uniform Corium Flowrate and Debris Bed Atop Former Plate.

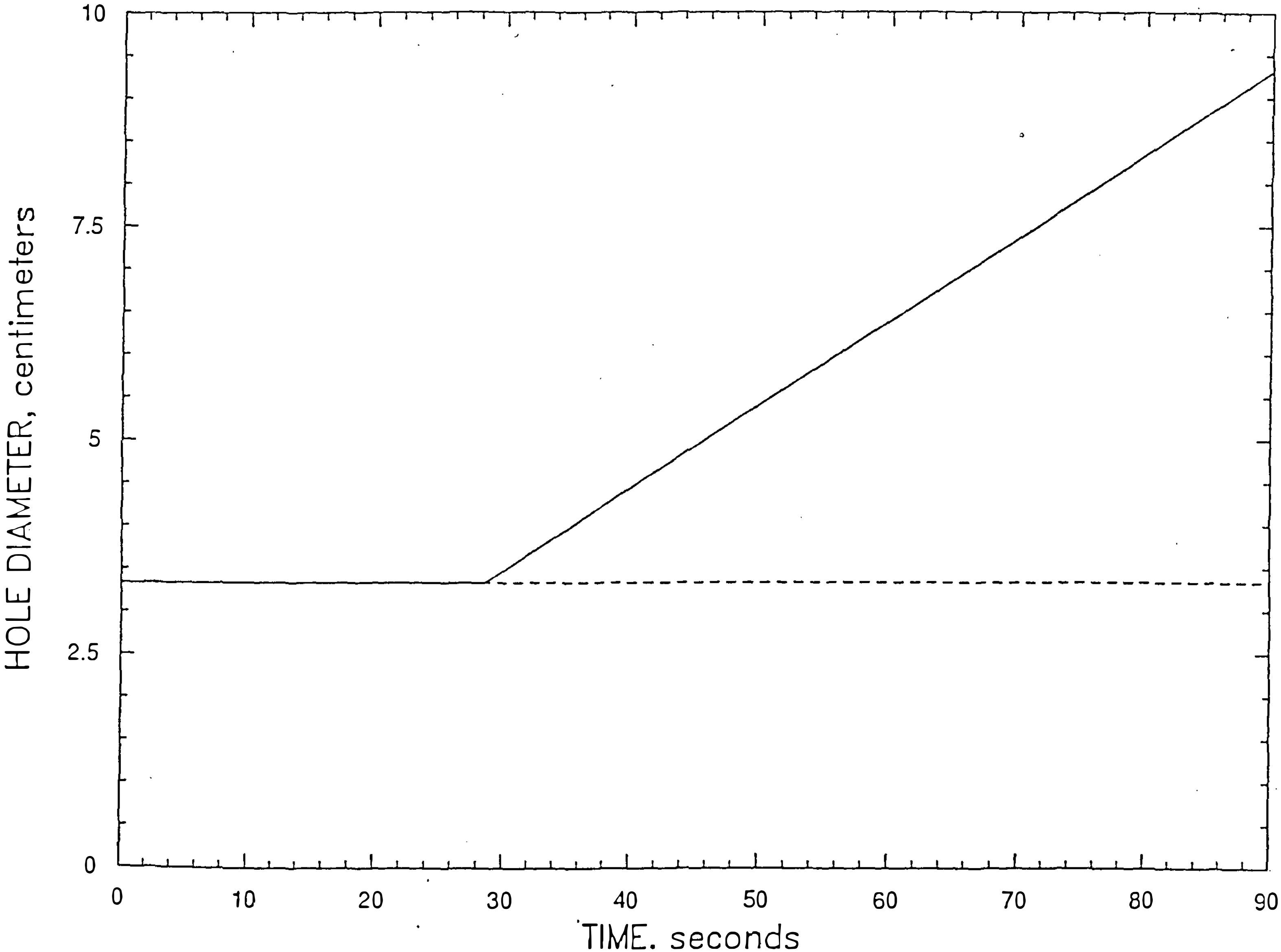

Figure D.3 Diameter of Flow Holes Inside Spreading Region for Case of Uniform Corium Flowrate and Debris Bed Atop Former Plate.

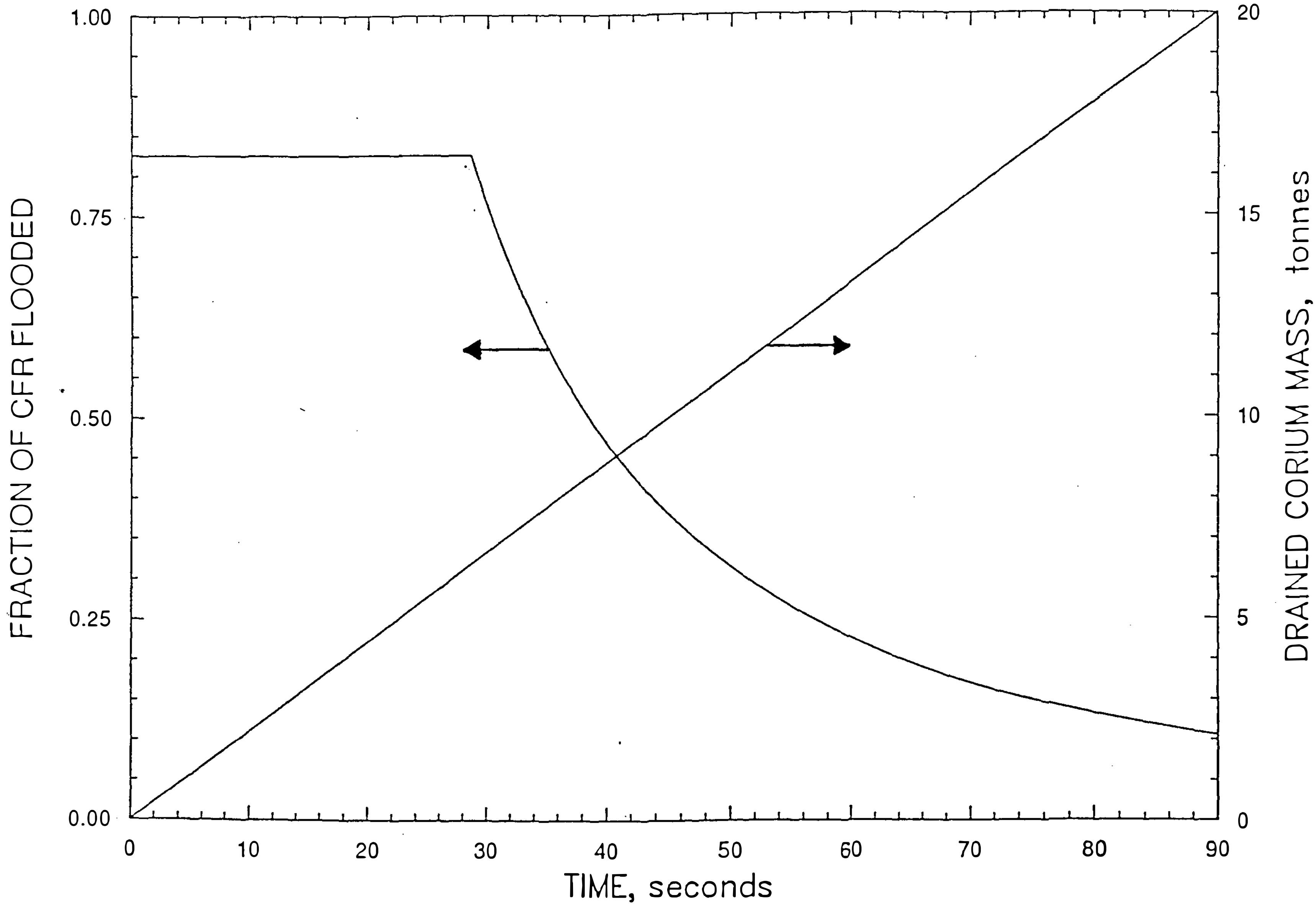

Figure D.4 Spreading of Corium Inside CFR and Drained Corium Mass for Case of Uniform Corium Flowrate and Debris Bed Atop Former Plate.

spreads nearly all the way around the CFR. Referring back to Figure D.1, it is observed that the depth distribution corresponds to very small depths near the maximum penetration half-distance, L. The region of significant depths coincides with a half-distance of roughly 0.75 L such that the present calculation would indicate significant corium spreading over about 60% of the CFR circumference. This prediction is in good agreement with the defueling examinations. The reduction in the spreading fraction at late times represents a progressively enhanced drainage in the vicinity of the baffle plate failure location. At the completion of corium flow, the corium spreading fraction decreases to 0.1.

The calculation was repeated without reducing the effective channel width to account for the effects of debris bed formation. Thus, the width was set equal to 12.23 centimeters (4.815 inches) corresponding to the unobstructed mean baffle plate-core barrel separation. The model predictions are shown in Figures D.5-D.7. The greater channel width requires a lower driving head to deliver the corium down the channel (Figure D.5). The lower corium depths give rise to lower drainage velocities such that the inception of flow hole enlargement is delayed until 42 seconds (Figure D.6). To achieve the total corium flowrate with lower layer depths, the corium spreads over a greater distance. As shown in Figure D.7, corium is predicted to spread completely around the CFR circumference until after 44 seconds. Significant corium layer depths are thus indicated over at least three-fourths of the circumference of the CFR. Strictly speaking, the analytical solution does not apply to a spreading channel having a limited length. If such a solution were to be carried out, the driving head would be greater than that shown in Figure D.5 over the time interval when the spreading factor exceeds unity. This would produce a correspondingly somewhat greater corium depth, drainage velocity, and flow hole heatup or ablation. A minimum spreading fraction of 0.2 is calculated at the completion of drainage.

In conclusion, corium entering the core former region through a localized breach in the baffle plates will spread around most of the circumference of the core former region while draining through the holes in the former plates in agreement with the results of the defueling examinations.

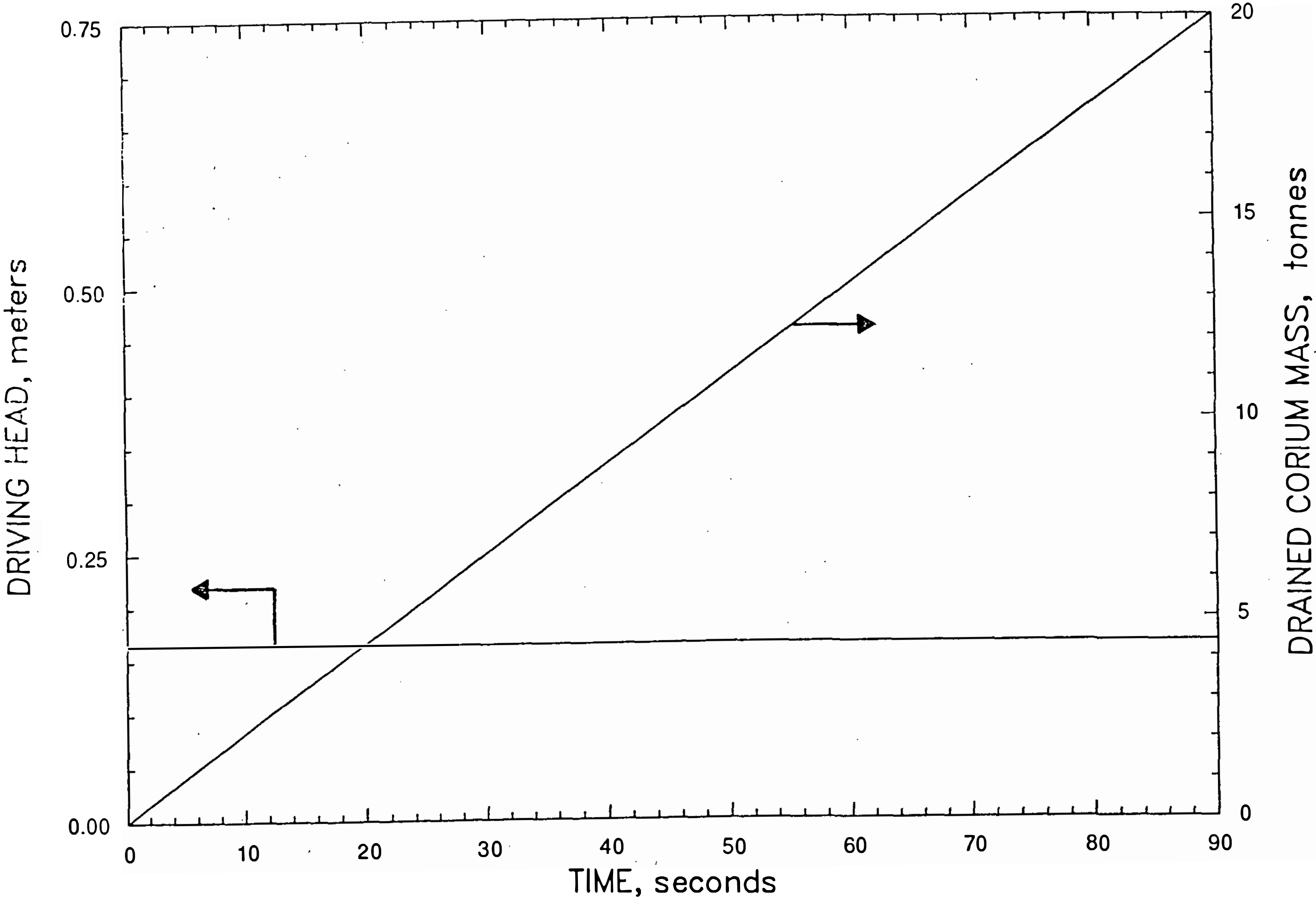

Figure D.5 Driving Head and Drained Corium Mass for Case of Uniform Corium Flowrate and Unobstructed Channel Width.

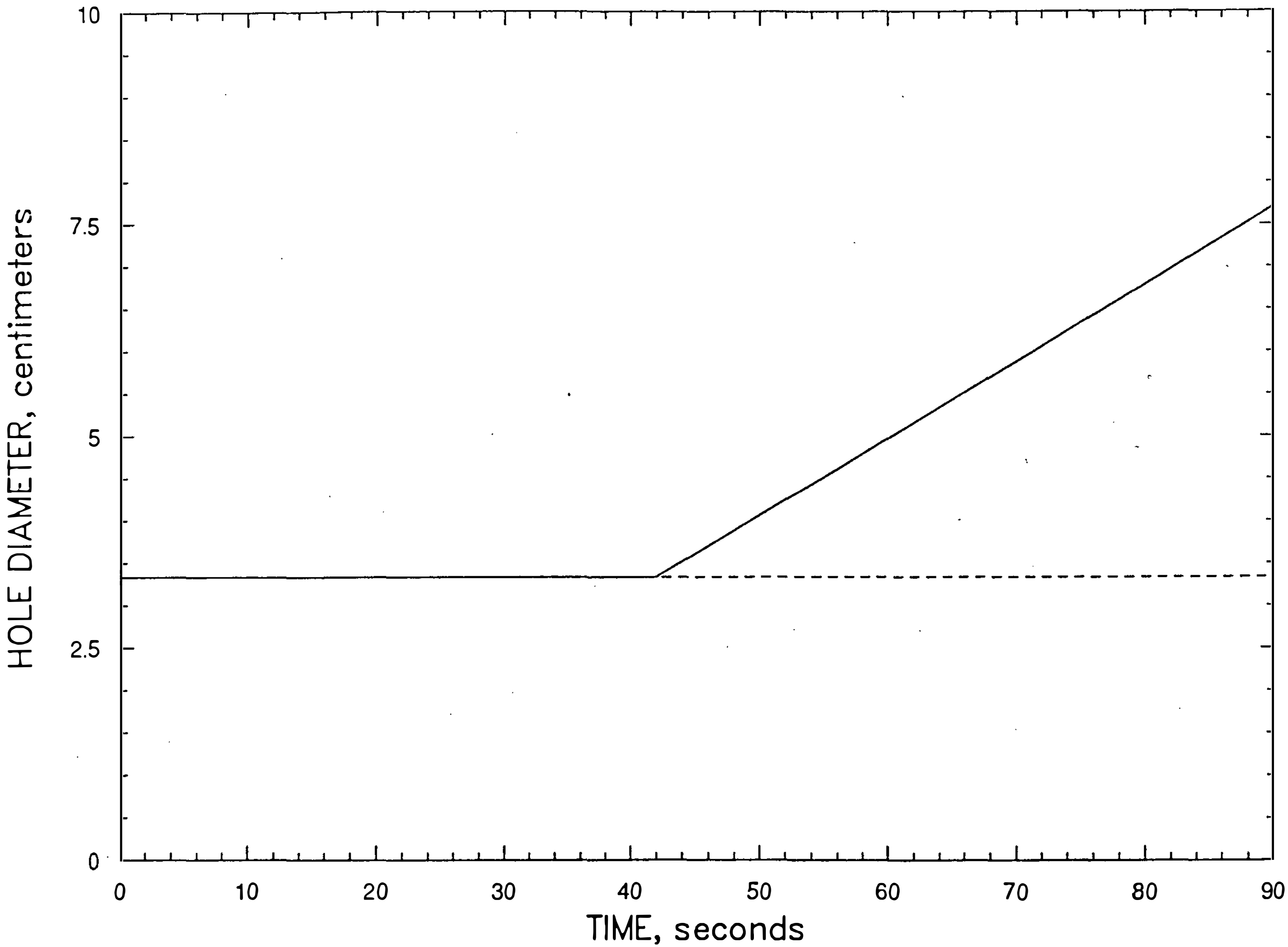

Figure D.6 Diameter of Flow Holes Inside Spreading Region for Case of Uniform Corium Flowrate and Unobstructed Channel Width.

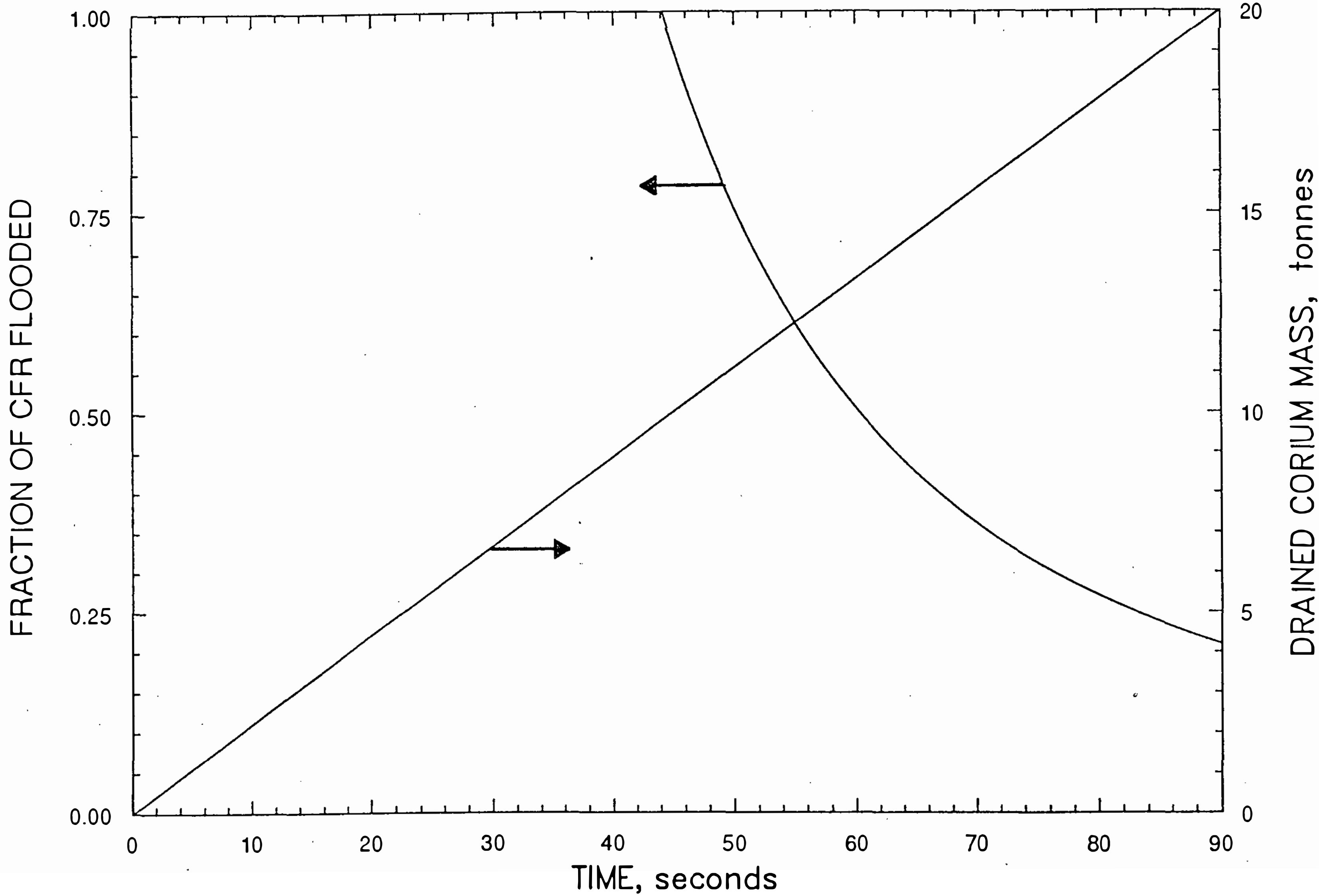

Figure D.7 Spreading of Corium Inside CFR and Drained Corium Mass for Case of Uniform Corium Flowrate and Unobstructed Channel Width.

APPENDIX E

RELOCATION OF CONTROL ROD MATERIAL

Based on the current understanding of the core heatup during the TMI-2 accident, the zircaloy guide tubes might have failed at ~1700 Kelvins (2600 degrees Farenheit) as a result of stainless steel melting and subsequent dissolution of the zircaloy guide tubes by molten silver, indium, cadmium and stainless steel before the molten core material relocated at 224 minute[10]. The TMI-2 core contains approximately 2500 kilograms (5500 pounds) of the Ag-In-Cd control rod alloy. The alloy composition is approximately 80% Ag, 15% In and 5% Cd by weight and it melts around ~1100 Kelvins (~1520 degrees Farenheit).

A. Assumptions of Relocated Control Rod Material

The zircaloy guide tubes are assumed to fail at 0.5 meter (20 inches) above the bottom of the active core based on the current perception of the core water level during the first 174 minutes. The molten control rod material contained in the zircaloy guide tubes above the breaches is assumed to drain from the breaches with ~600 Kelvins (1080 degrees Farenheit) superheat, i.e., an initial temperature of ~1700 Kelvins (2600 degrees Farenheit). It is further assumed that all the control rods failed except for those located in the outermost fuel assemblies which are found virtually intact during the incore inspection[10]. Therefore, a total amount of ~1650 kilograms (3630 pounds) molten control rod material is assumed to relocate to the vessel lower head. The molten control rod material drained from the breach flows along the guide tube as a film flow. The energy transferred to the tube and the interaction with water during the drainage of the film flow is neglected. A cylindrical molten Ag-In-Cd jet is assumed to form at the bottom of each control rod and interacts with the core water presumably at saturated temperature. The additional jet breakup due to the CSA is neglected to yield a minimum erosion of jet material and a conservative vessel heatup calculation.

B. Initial Conditions of Jet/Water Interaction

The molten alloy exit velocity is calculated as a function of the height of the remaining molten alloy in the tube. Based on Bernoulli's equation, the exit velocity, $\bar{V}_e$, and the height of the molten alloy above the break, h, are given by

$$\bar{V}_e = \sqrt{\frac{2gh}{1 + K_c - (A_B/A_c)^2}} \qquad (E.1)$$

and

$$h = \left[h_o - \frac{1}{2} \left[\frac{2g\ (A_B/A_c)^2}{1 + K_c - (A_B/A_C)^2}\right]^{1/2} t \right]^2 \qquad (E.2)$$

where

h_o = initial height of the molten alloy above the break, m,

A_B = area of break in the guide tube, m^2,

A_c = cross sectional area of control rod, m^2, and

K_c = loss coefficient.

The exit velocity is shown in Figure E.1 as a function of the break size. It shows that the exit velocity varies linearly with time. In the current analysis, a guillotine break is assumed to yield a highest exit velocity and a maximum break area with diameter d_B ~10 millimeters (0.394 inch). According to the jet breakup model as described in Appendix C, jet with higher initial velocity normally suffers less dispersion by the ambient fluid due to shorter time of interaction with the water in a vessel of finite depth. Furthermore, a constant velocity equal to the initial exit velocity, i.e., the exit velocity when $h = h_o$, is used during the course of ejection in order to simplify the analysis.

The velocity of the cylindrical molten stream which drained from the bottom of the control rod into the core water is evaluated by averaging the velocity profile of the film flow which may be accelerated or retarded due to the influences of gravity and surface drags. The variation of the velocity profile of a film flow is shown in Figure E.2. Using the boundary-layer

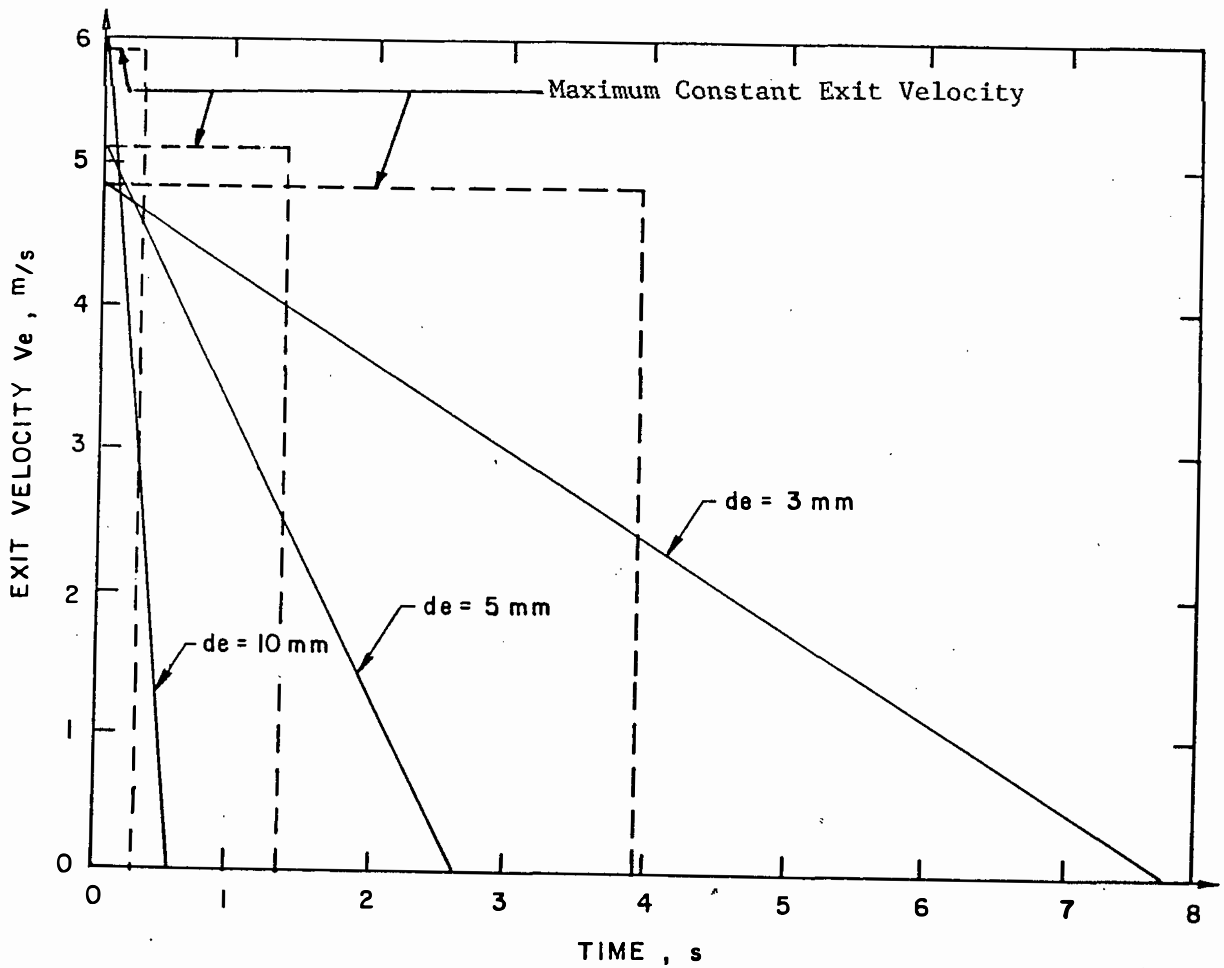

Figure E.1 Exit Velocity of the Molten Control Rod Alloy

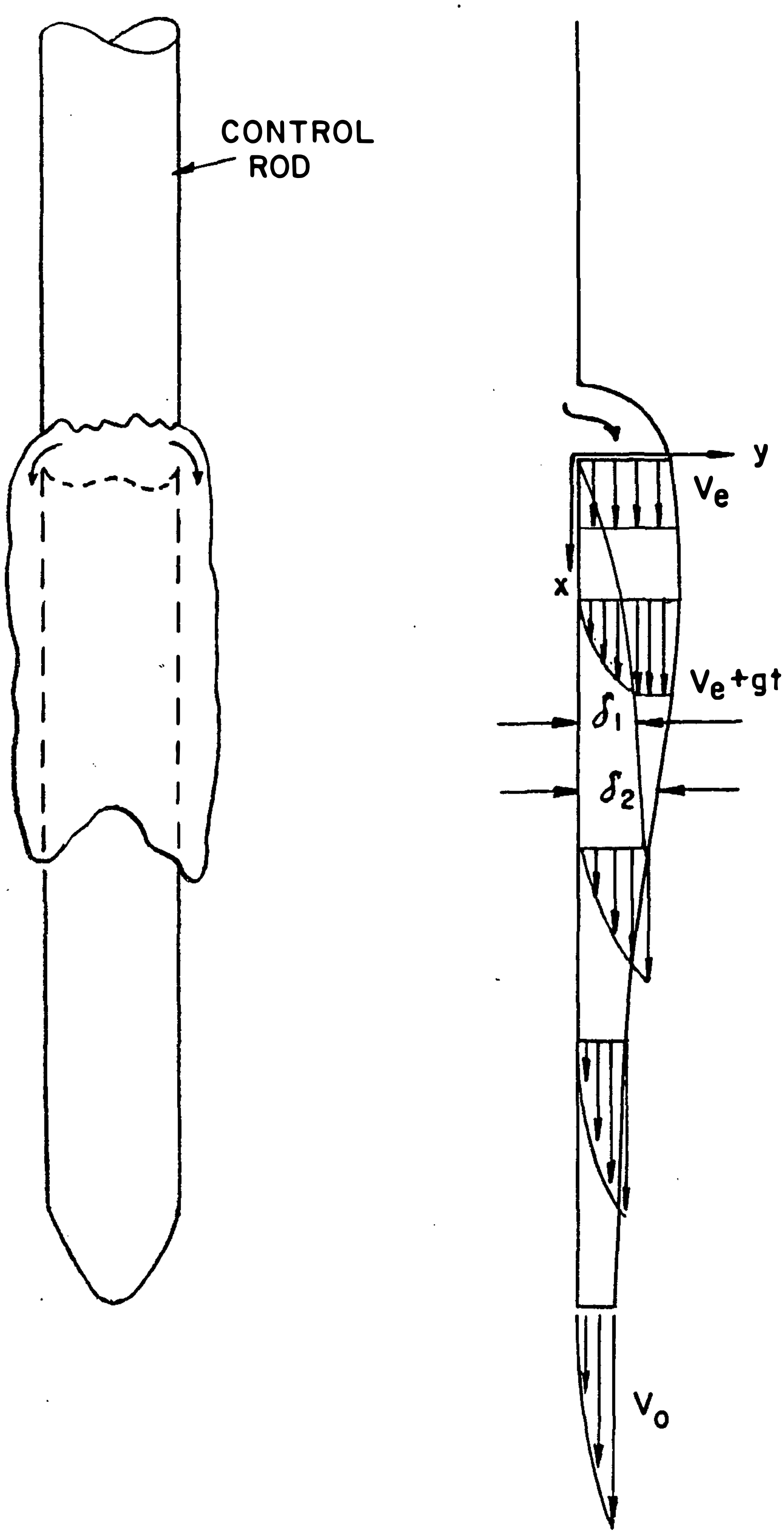

Figure E.2 Film Flow on Control Rod Guide Tube approximations for an incompressible, steady-state flow, the Navier-Stokes equation is written as:

$$u \frac{\partial u}{\partial x} + v \frac{\partial u}{\partial y} = - \frac{1}{\rho} \frac{\partial p}{\partial x} + g + \nu \frac{\partial^2 u}{\partial y^2} \tag{E.3}$$

Integrating Equation E.3 from 0 to δ_1, where δ_1 is the boundary layer thickness, and ignoring the pressure gradients, Equation E.3 yields:

$$- \frac{\partial}{\partial x} \int_0^{\delta_1(x)} u(x)^2 \, dy + V(x) \frac{\partial}{\partial x} \int_0^{\delta_1(x)} u(x) dy + g\delta_1(x) = \nu \left. \frac{\partial u}{\partial y} \right]_{y=o} \tag{E.4}$$

The continuity equation can be written as:

$$\int_0^{\delta_1(x)} u(x)dy + V(x)[\delta_2(x) - \delta_1(x)] = \bar{V}_e A_B / \pi d_c$$

where δ_2 is the molten film thickness and d_c is the control rod diameter. Note that the molten film has a flat velocity profile and is free of the boundary layer drag in the region between $y = \delta_1$ and $y = \delta_2$.

The boundary layer thickness, δ_1, is solved by assuming a parabolic velocity profile in the boundary layer, i.e.,

$$\frac{u(x)}{V(x)} = 2\eta - \eta^2 ; \; \eta = \frac{y}{\delta_1(x)} \tag{E.6}$$

Obviously, Equation E.6 satisfies the "no-slip" condition on the tube wall and the continuity condition at $y = \delta_1$ (x). The molten film outside of the boundary layer is subject to gravity only. Thus,

$$V(x) = (V_e^2 + 2gx)^{1/2} \tag{E.7}$$

Substituting Equations E.6 and E.7 into Equation E.4, a differential equation can be derived:

$$\frac{2}{15}\left(V_e^{\,2} + 2gx\right)\frac{\partial \delta_1}{\partial x} + \frac{3g\delta_1}{5} = \frac{2\left(V_e^{\,2} + 2gx\right)^{1/2}\nu}{\delta_1} \tag{E.8}$$

Finally, the initial jet velocity is calculated by averaging the velocity profile at the bottom of the control rod as written as:

$$V_o = \frac{1}{\delta_2}\left[\int_o^{\delta_1} u(x)dy + \left(V_e^{\,2} + 2gx\right)^{1/2}(\delta_2 - \delta_1)\right] \quad \text{at the bottom of the control rod} \tag{E.9}$$

Where δ_2 is determined by using Equation E.5.

C. Calculations of Jet Breakup and Quench

The breakup and quench of the molten control rod alloy is calculated using the model described in Appendix C. The masses of the coherent jet and the dispersed particulate are shown in Figure E.3. As predicted by the model, the molten control rod alloy suffers an extensive breakup and retains the form of a coherent jet only within a short traveling distance. Therefore, the configuration excludes a possible thermal attack upon the vessel lower head by an impinging coherent jet. The average temperature of the dispersed particulate as shown in Figure E.4 is predicted to be well below the melting temperature of the control rod alloy, i.e., ~1100 Kelvin (1520 degrees Farenheit). As a result, the solidified control rod debris bed is not likely to yield any significant vessel heatup. Furthermore, the control rod debris bed is predicted to spread over a region of radius 0.881 meter (35 inches) to 0.957 meter (38 inches) depending on the debris packing arrangement. As shown in Figure E.5, if the corium jet is assumed to drain from the core former region into the core water, the jet impinging zone (if any) would be outside of the control rod debris bed. The particle size of the dispersed control rod alloy is predicted to range from ~3 millimeters (0.118 inch) to ~10 millimeters (0.394 inch) with 90% of the particles smaller than ~5 millimeters (0.197 inch).

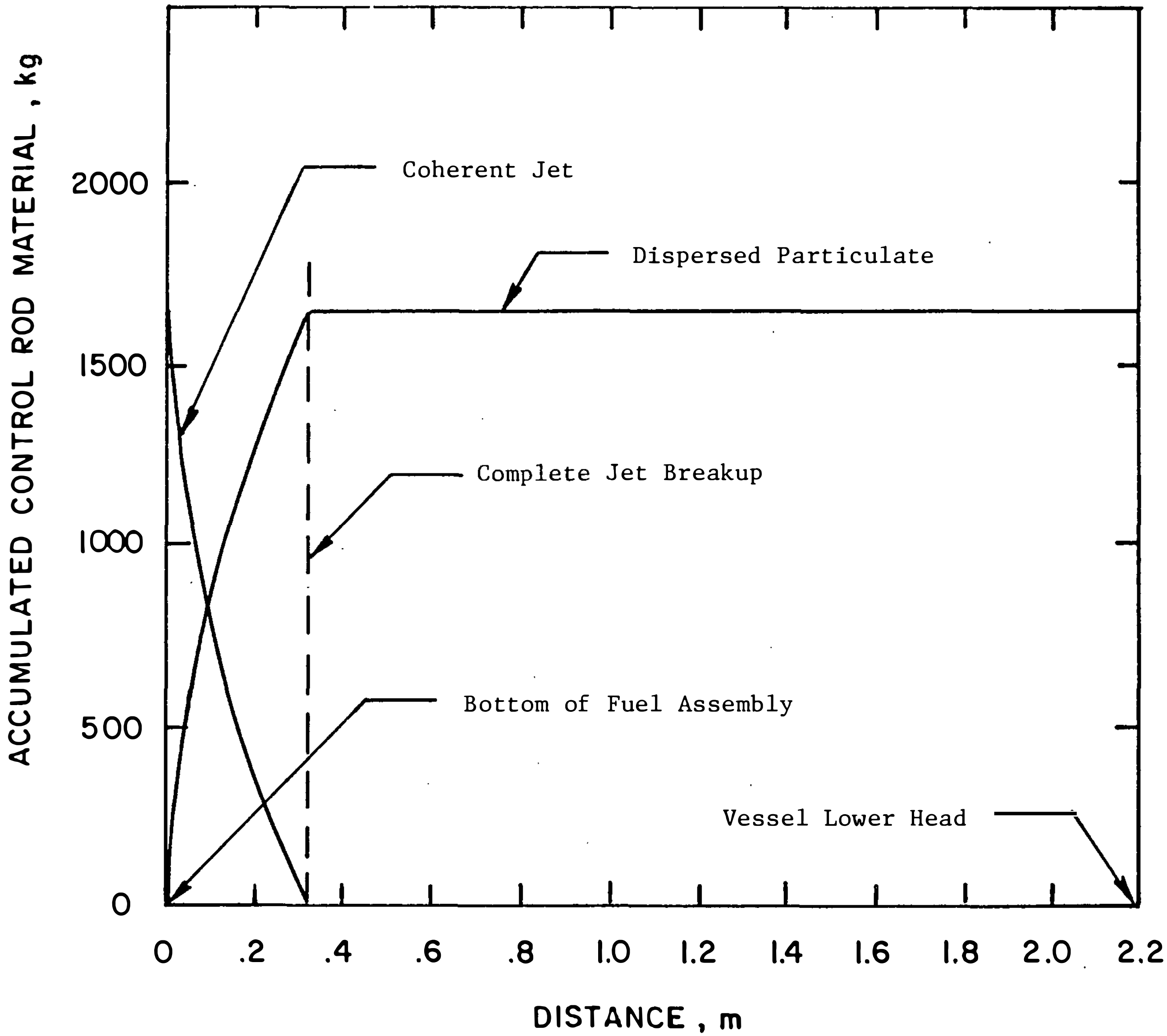

Figure E.3 Breakup of Molten Control Rod Material

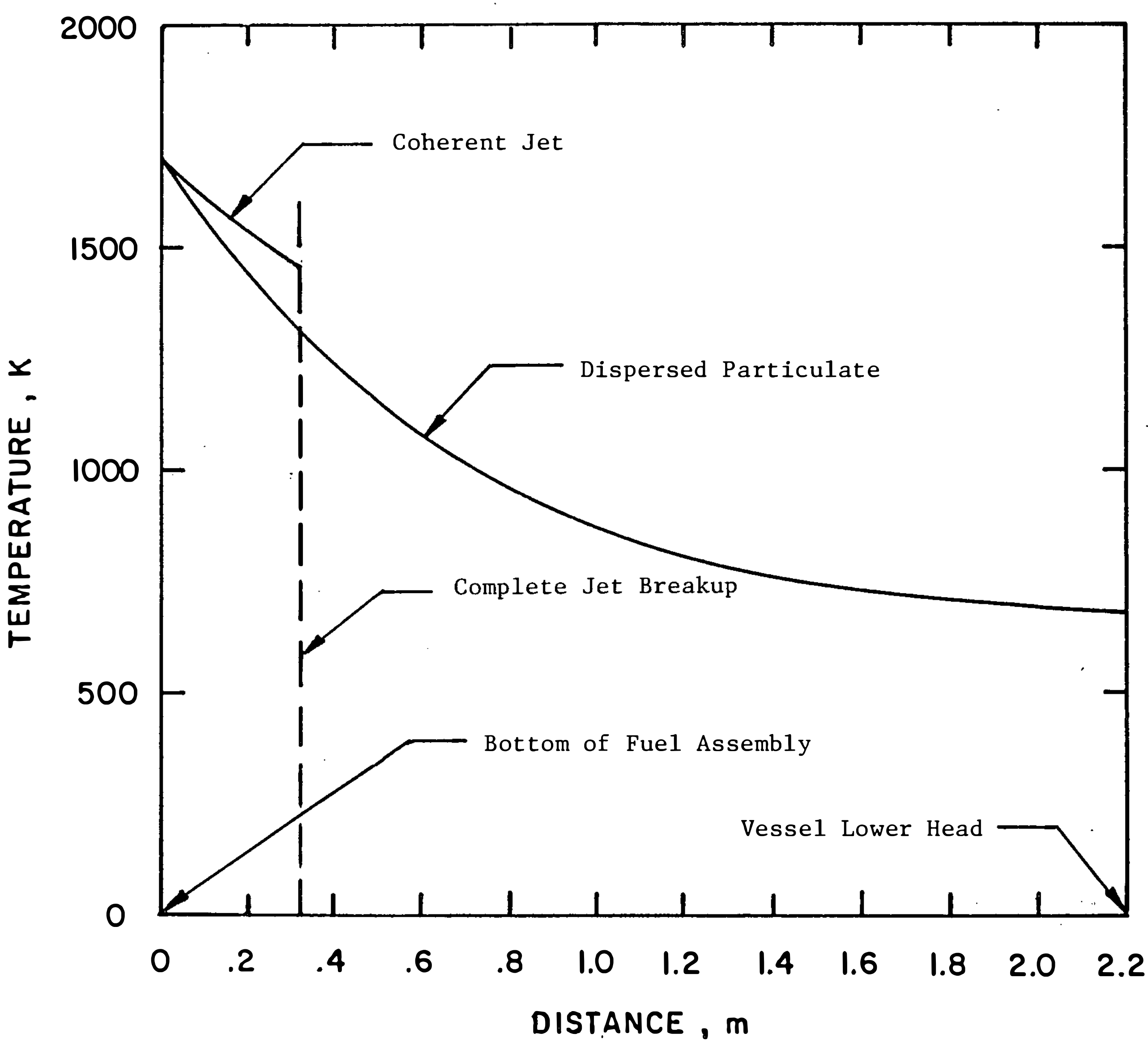

Figure E.4 Temperature Variation of Control Rod Material

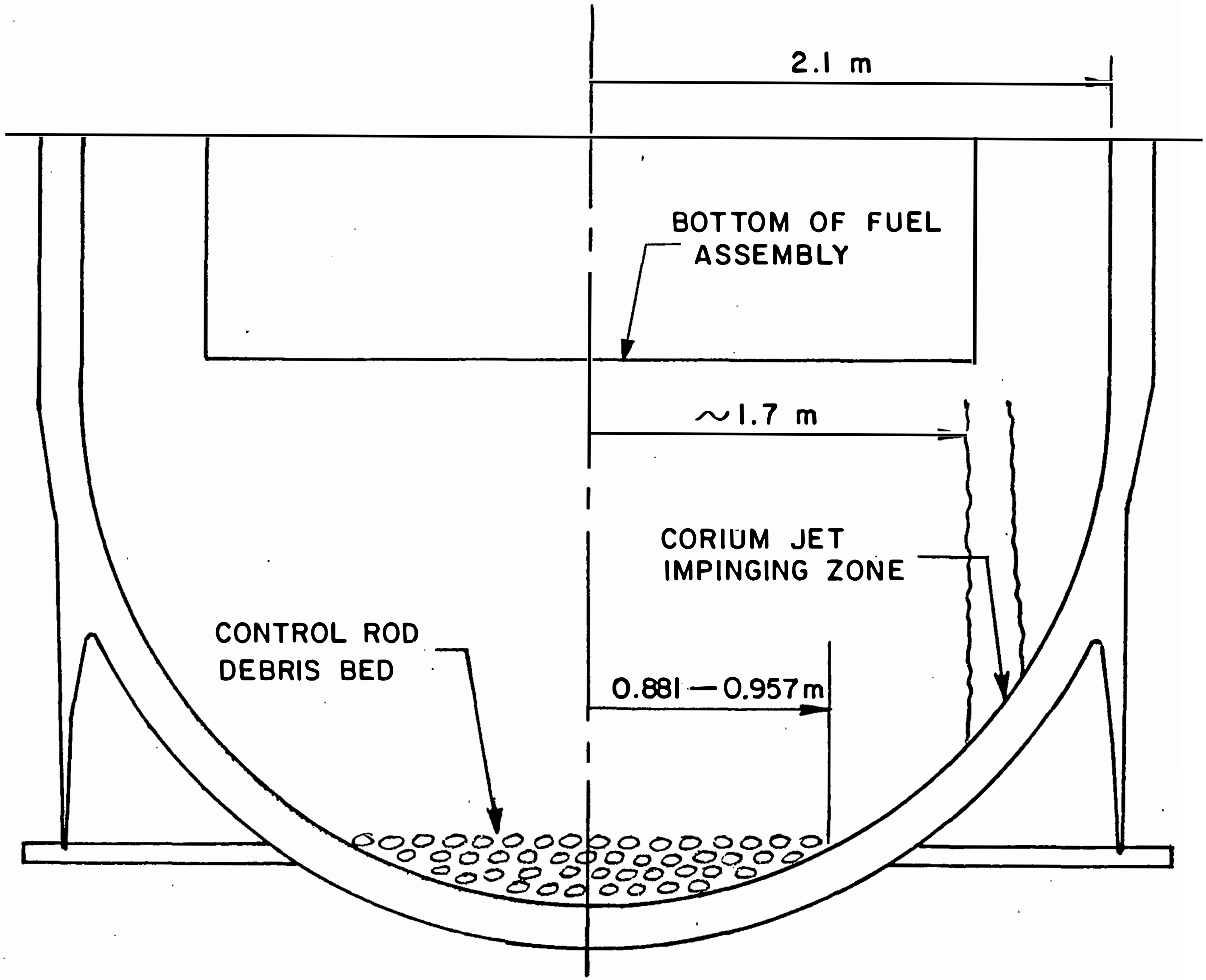

Figure E.5 Configuration of Control Rod Debris Bed

APPENDIX F

HEATUP AND ABLATION OF LOWER HEAD BY AN IMPINGING CORIUM JET

The MISTI (Melt Impingement upon Structure Thermal Interactions) computer code was previously developed to predict the time dependent heatup and ablation of a finite thickness plate in response to an impinging corium jet. The code was employed in the analysis of the CSTI-1, CSTI-3, and CWTI-11 reactor material experiments[33] in which oxide-metal corium mixtures were impinged upon a 1.27 centimeter (0.5 inch) thick stainless steel plate supported by a similar 3.81 centimeter (1.5 inch) thick base plate. The computer code, experiments, and analysis are documented in Reference 33 in which it is demonstrated that the measured heatup rates of thermocouples embedded immediately beneath the plate surface are indicative of the presence of an interstitial oxide crust between the flowing molten corium and the steel substrate. The term "crust" here refers to a stable solidified layer of corium which forms upon the steel substrate and tends to insulate the steel from the hot molten corium.

Prior to the onset of steel melting, the code calculates the growth of the solid crust consistent with forced convection heat transfer from the impinging molten corium and thermal conduction downward through the crust and vessel lower head wall. The thickness of the crust, δ_c, satisfies the equation,

$$\rho_{f,c} L_f \frac{d\delta_c}{dt} = -k_{f,c} \left.\frac{\partial T_c}{\partial z}\right]_{z=\delta_c} - h_{conv} \left(T_{f,imp} - T_{f,freeze}\right) , \qquad (F.1)$$

where

$\rho_{f,c}$	= corium crust density,
L_f	= corium heat of fusion,
δ_c	= corium crust thickness,
t	= time,
$k_{f,c}$	= corium crust thermal conductivity,
T_c	= crust temperature,

z = displacement from crust-steel interface,

h_{conv} = forced convection heat transfer coefficient,

$T_{f,imp}$ = temperature of impinging corium,

$T_{f,freeze}$ = corium freezing temperature,

f = subscript denoting corium,

c = subscript denoting crust.

The thermal gradient is evaluated within the crust at the crust upper surface located at $z = \delta_c$. Temperatures within the crust and the steel wall are obtained from the solution of the one-dimensional thermal conduction equations,

$$\rho_{f,c} \frac{\partial e_c}{\partial t} = \frac{\partial}{\partial z} \left[k_{f,c} \frac{\partial T_c}{\partial z} \right] , \tag{F.2}$$

$$\rho_s \frac{\partial e_s}{\partial t} = \frac{\partial}{\partial z} \left[k_s \frac{\partial T_s}{\partial z} \right], \tag{F.3}$$

where

e_c = corium crust specific enthalpy at temperature T_c,

ρ_s = steel wall density,

e_s = steel specific enthalpy,

k_s = steel thermal conductivity,

T_s = steel temperature

The solution is subject to the boundary conditions,

$$T_c \Big]_{z=\delta_c} = T_{f,freeze} , \tag{F.4}$$

$$T_c \Big]_{z=0} = T_s \Big]_{z=0}, \tag{F.5}$$

$$k_{f,c} \left.\frac{\partial T_c}{\partial z}\right]_{z=0} = k_s \left.\frac{\partial T_s}{\partial z}\right]_{z=0} , \tag{F.6}$$

$$\left.\frac{\partial T_s}{\partial z}\right]_{z = -\delta_{wall}} = 0, \tag{F.7}$$

where

δ_{wall} = steel wall thickness,

Equation F.4 states that the temperature at the upper surface of the crust is equal to the corium freezing temperature reflecting the growth and remelting of crust at the upper surface. Equations F.5 and F.6 are an assumption of perfect thermal contact at the corium crust-solid steel interface. In actuality, a less than ideal contact might exist due to the existence of a narrow gap between the solidified crust and the solid steel. In this case, the current analysis will be somewhat conservative in that higher heat fluxes and higher steel temperatures are predicted in the absence of a contact thermal resistance. The outside surface of the lower head is presently treated as an adiabatic surface as indicated by Equation F.7.

The heat transfer coefficient accounts for the effects of turbulent forced convection from the flowing molten corium to the crust. Heat transfer coefficients for impingement flow are usually presented in terms of correlations representing values averaged over discs centered about the jet centerline. For the current application, the heat transfer coefficient is taken equal to the disc averaged value recommended by Martin[34] for a disc of radius $r = D_{jet}$, surrounding the jet centerline. This radius corresponds to the jet impingement zone in which the corium is redirected from a downward flowing jet to flow horizontally over the lower head surface. It has been found convenient to fit the following function to the values presented graphically in Reference 34:

$$h_{conv} = 0.606\, Re_f^{0.547}\, Pr_f^{0.42}\, \frac{k_{f,jet}}{D_{jet}} \tag{F.8}$$

where

$$Re_f = \frac{\rho_f U_{jet} D_{jet}}{\mu_{f,jet}},$$

= Reynolds number of impinging jet,

$$Pr_f = \frac{C_{f,jet} \mu_{f,jet}}{k_{f,jet}},$$

= Prandtl number of impinging jet,

ρ_f = molten corium density,

U_{jet} = velocity of impinging jet,

D_{jet} = diameter of impinging jet,

$\mu_{f,jet}$ = viscosity of molten corium in impinging jet,

$C_{f,jet}$ = specific heat of molten corium,

$k_{f,jet}$ = thermal conductivity of molten corium,

jet = subscript denoting impinging jet.

If the temperature at the crust-steel interface rises to the steel melting temperature, then steel will be ablated away by the corium jet as it continues to impinge upon the steel. The principal assumption in modeling steel erosion is that an oxide corium crust remains present between the impinging jet and underlying stainless steel. As the steel melts, it is envisioned to flow outward from the jet centerline as a molten film. Under such conditions, the crust is expected to break up into small segments which are swept along atop the melted steel film. Although the crust does not remain structurally stable, it still serves as a thermal boundary condition reducing the heat flux into the plate well below that which would be predicted in the complete absence of crust formation.

Erosion of the vessel wall is calculated by modeling the steel ablation as a quasi-steady process. The steel ablation rate is given by

$$\frac{d\delta_s}{dt} = \frac{Q}{\rho_s \left[e_{s,liq} - \frac{Qt_{heatup}}{\rho_s \delta_{heatup}} + \frac{1}{2} C_{s,film} (T_{int} - T_{s,melt}) \right]} \tag{F.9}$$

where

Q = $h_{conv} (T_{f,imp} - T_{f,freeze})$, (F.10)

= forced convection heat flux,

δ_s = steel thickness eroded away,

ρ_s = steel density,

$\Delta e_{s,liq}$ = change in steel specific enthalpy in going from initial temperature to liquidus,

t_{heatup} = time to melting inception following onset of impingement,

δ_{heatup} = penetration distance of thermal wave into steel at melting inception,

$C_{s,film}$ = melted steel film specific heat,

T_{int} = temperature at corium crust-steel melt film interface,

$T_{s,melt}$ = steel melting temperature.

The third term in the denominator represents energy deposited in the lower head wall over the depth, δ_{heatup}, during the transient heatup phase of duration, t_{heatup}. The crust thickness satisfies

$$\delta_c = \frac{k_{f,c}(T_{f,freeze} - T_{int})}{Q} . \tag{F.11}$$

The interface temperature satisfies

$$T_{int} = T_{s,melt} + \frac{h_{conv}(T_{f,imp} - T_{f,freeze})\,\delta_{s,film}}{k_{s,film}} \tag{F.12}$$

where $\delta_{s,}$ film is the thickness of the molten steel film. The steel melt film has a uniform thickness in the jet impingement region. MISTI employs an approximate expression for the film thickness derived from conservation of the flowing melted steel mass and by equating the shear stress at the top of the film to that at the bottom of the boundary layer of the impinging jet. In particular, the film thickness is determined from the solution of the equation,

$$\delta_{film} = \left\{ \frac{AQ}{\rho_s \left(\Delta e_{s,liq} - \frac{Q_{t,heatup}}{\rho_s \delta_{heatup}} + \frac{C_{s,film} Q \delta_{s,film}}{2k_{s,film}} \right)} \right\}^{1/2} , \qquad (F.13)$$

where

$$A = \frac{1}{1.3120a} \left(\frac{\mu_{s,film}}{\mu_{f,jet}} \right) \left(\frac{\mu_{f,jet}}{a \rho_f} \right)^{1/2} , \qquad (F.14)$$

$$a = \frac{U_{jet}}{D_{jet}} .$$

The analysis is carried out using temperature dependent thermophysical properties for corium and the lower head steel discussed in Appendices A and B respectively. Representative values are shown in Tables A.1 and B.1. Calculations are continued until either the impinging corium mass is exhausted or complete meltthrough of the vessel wall occurs.